POLITECNICO DI TORINO

Master of Science in Energy and Nuclear Engineering

Master Thesis

Assessment of thermal-hydraulic performance of circular pipes equipped with Triply Periodic Minimal Surfaces

Supervisors
Prof. Laura Savoldi
Prof. Nima Fathi

Candidate
Cecilia Piatti

March 2023

Abstract

One of the greatest challenges that the scientific community is addressing in this century is to provide clean and abundant energy to satisfy the increasing worldwide demand. Many solutions are already existing or currently under development and some of them require to deal with very high temperatures and high heat loads. As an example, heat fluxes are expected to reach values up to $20\,MW/m^2$ on some components of nuclear fusion plants. Thus, it is necessary to design very efficient heat sinks in order to respect the thermo-mechanical limitations of the structural materials.

Triply Periodic Minimal Surfaces (TPMS) are three-dimensional surfaces that can be mathematically described by sinusoidal and cosinusoidal functions. From these surfaces periodic lattices can be generated and, among other applications, they can be used to equip channels for heat dissipation. In recent decades, TPMS have become more and more interesting due to the advent of Additive Manufacturing that allows the production of such complex objects. They may therefore effectively substitute other porous media configurations, introducing regularity and reducing the pressure drop in the flow due to their smooth curvature.

TPMS-based structures can be generated with numerous different settings. After the selection of the topology, it is possible to choose whether to construct the structure in solid or sheet form. The first method produces a single channel, while the second one results in two parallel channels. Moreover, the unit cell dimension has to be set, together with the average thickness and the coordinates type to use for the structure generation (Cartesian, cylindrical or spherical). This wide range of options leads the TPMS to an extreme versatility and suitability to several applications, due to the possibility of adapting them to the shape and size of the problem domain.

The present work aims at the study and performance assessment of four TPMS-based structures, namely *Diamond*, *Gyroid*, *Lidinoid* and *SplitP*. The first two TPMS have been already object of numerous studies, mainly in the field of innovative heat exchangers, that indicated better performance with respect to traditional solutions. On the contrary, there is no available literature yet regarding thermal-hydraulic applications of the other two TPMS.

In the present work, the four structures under investigation have been inserted in a circular channel 10 cm long. Their behaviors have been analyzed through numerical simulations on the Computational Fluid Dynamics software *STAR-CCM+*, performed considering Copper for the walls and internal solid structure and water as coolant.

The dependence of hydraulic and thermal quantities on the unit cell dimension has been assessed through a parametric study for each lattice. Comparing the different TPMS, it has been found that the *Gyroid* and the *Diamond* produce lower pressure drops in the fluid flow, at the cost of poor thermal performances, while the *Lidinoid* and *SplitP* behave exactly the

opposite way. From these considerations, the possibility to combine two TPMS types has been investigated, splitting the cylindrical channel domain in two regions. *Diamond* or *Gyroid* have been inserted in the core region and the outer layer has been filled with *Lidinoid* or *SplitP* with a smaller unit cell dimension, in order to enhance heat exchange next to the wall. Four combinations have been designed and the simulations results have confirmed the expectations, suggesting that an optimization process on the thickness of the outer layer could lead to interesting outcomes.

For all the analyzed configurations, the turbulence enhancement factor has been computed to estimate the performance improvement with respect to the smooth tube.

An experimental campaign, currently ongoing at the Texas A&M University, will help in confirming and qualifying the simulated results on the different TPMS configurations.

Contents

List of Figures

List of Tables

Abbreviations

Symbols	**Description**	Units
A	Surface area	$[m^2]$
c	Convergence order	
D_h	Hydraulic diameter	$[m]$
h	Mesh average cell size	$[m]$
k	Turbulent kinetic energy per unit mass	$[m^2/s^2]$
L	Length	$[m]$
$\dot{m}$	Mass flow rate	$[kg/s]$
P	Perimeter	$[m]$
p	Pressure	$[Pa]$
Q	Power	$[W]$
s	Unit cell size	$[mm]$
T	Temperature	$[K]$
t	Time	$[s]$
U	Velocity	$[m/s]$
V	Volume	$[m^3]$
Δ	Difference	
ϵ	Rate of dissipation of turbulent kinetic energy	$[m^2/s^3]$
ϵ_r	Relative error	$[-]$
μ	Dynamic viscosity	$[Pa \cdot s]$
ν	Kinematic viscosity	$[m^2/s]$
ρ	Density	$[kg/m^3]$
ϕ	Porosity	$[-]$
ω	Turbulence frequency	$[s^{-1}]$

Acronyms	**Description**
AM	Additive Manufacturing
CFD	Computational Fluid Dynamics
GCI	Grid Convergence Index
HTC	Heat Transfer Coefficient
Lag-EB	Lag Elliptic Blending
Nu	Nusselt Number
Pr	Prandtl Number
RANS	Reynolds Averaged Navier-Stokes
Re	Reynoldws number
SM	Subtractive Manufacturing
SST	Shear Stress Transport
TPMS	Triply Periodic Minimal Surface

Chapter 1

Introduction

Decarbonization is one of the greatest challenges that the scientific community worldwide is addressing in the present age. It is in fact needed to keep under control the Earth average temperature increase, in order to avoid the worsening of the effects of climate change [1]. Meanwhile, we are experiencing an increasing of the energy demand [2], [3], [4]. Thus, the development of new technologies for the production of clean and abundant energy is more and more necessary. There are several available low Carbon power production options and they include mainly renewable energy sources, biomasses and nuclear fission energy [5]. Moreover, nuclear fusion is expected to produce a great amount of power in the next future, with low CO_2 and radioactive waste production levels, even though it is still at a research stage now [6].

Some of these options, such as solar and nuclear fission and fusion power plants, require dealing with high heat fluxes on different components, that demand efficient heat exchangers and heat sinks, to comply with the thermal-mechanical limitations of materials. For example, for fusion power plants components, such as the first wall, the divertor and the gyrotron, heat flux values can range from $1\,MW/m^2$ to $20\,MW/m^2$ [7]. Clearly, traditional heat sinks may not be adequate to sustain those heat loads and more effective solutions must be analyzed. Structures based on Triply Periodic Minimal Surfaces are investigated to provide effective cooling strategies to high heat loads components.

1.1 TPMS

Triply Periodic Minimal Surfaces (TPMS) are, by definition, minimal surfaces that are not subjected to variation if translated in three principal directions.

Minimal surfaces represent the solution to a mathematical problem invented by Joseph-Louis Lagrange and Leonhard Euler in the 18th century, that was to find a surface that minimizes the area in the neighborhood of each of its points [10], [11]. The trivial solution of this problem is the plane, but, as the time went by, many mathematicians addressed this matter and found other surfaces that satisfy the requirements. The first of them was Jean Baptiste Meusnier [12] who discovered the *Catenoid* and the *Helicoid* that are shown in figure (1.1).

Meusnier also elaborated more on the Lagrange theory and found out that requiring the area minimization means also vanishing curvature at every point, i.e. the mean value of the maximum and minimum curvature is equal to zero. This directly implies that every point of the surface is a saddle point, with principal curvatures that have equal and opposite values.

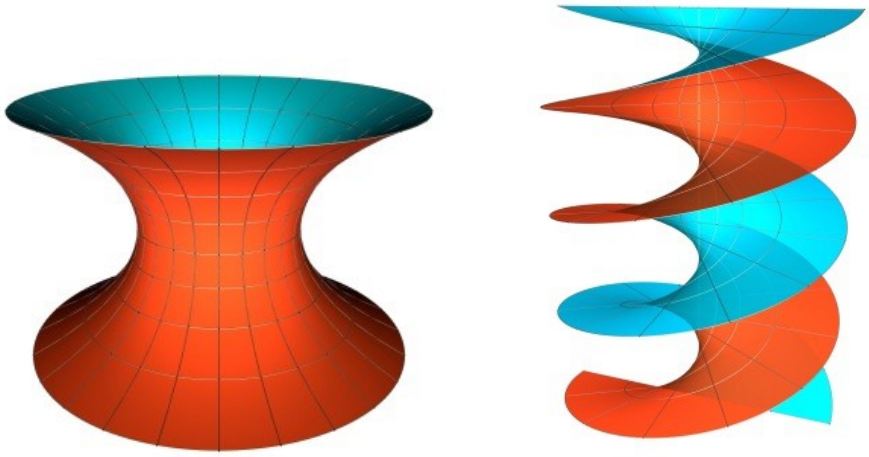

(a) **(b)**

Figure 1.1: *Examples of minimal surfaces, Catenoid (a) and Helicoid (b)*

Triply Periodic Minimal Surfaces (TPMS), as the name suggests, are defined as minimal surfaces with translational symmetries in three principal directions [13]. They are non-self-intersecting periodic surfaces, defined through mathematical equations (see table (2.1) for some examples), that generate lattices, thus composed of unit cells replicated in the three directions.

TPMS were reported for the first time by Hermann Schwarz and his student Edvard Rudolf Neovius in the 1880s, who established two TPMS that they named *Schwarz-P* (or *Primitive*) and *Schwarz-D* (or *Diamond*), shown in figure (1.2a) and (1.2b) [14],[15].

Later, in 1970, Alan Schoen [16], [17] designed many other types of TPMS, including the *Gyroid*, in figure (1.2c).

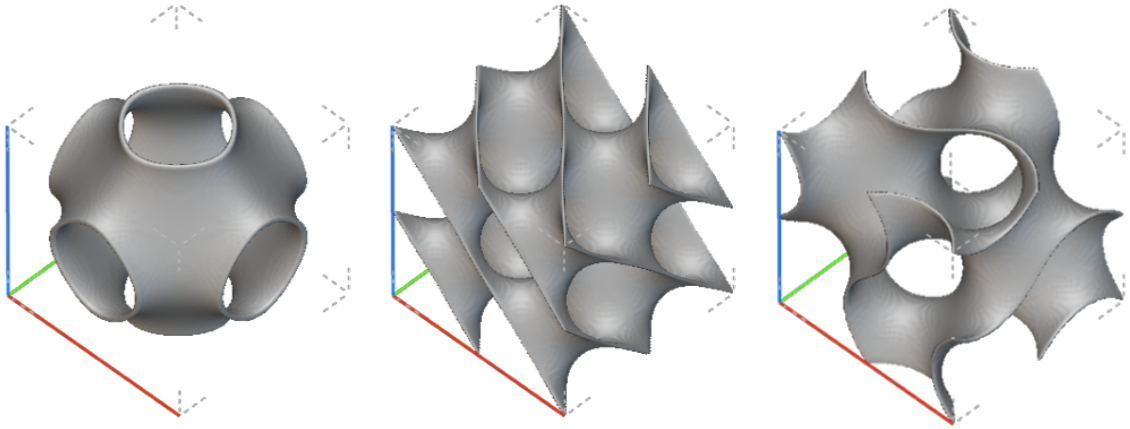

(a) **(b)** **(c)**

Figure 1.2: *First types of TPMS, Primitive (a), Diamond (b) and Gyroid (c)*

In the last decades, many other types of TPMS have been developed, only from a theoretical point of view, due to the impossibility of manufacturing them with traditional methods. Some of them are completely new, while some others are simply the evolution of already ex-

isting ones, that lead to the establishment of families of TPMS. Still, this classification is not complete and it is evolving as new surfaces are identified.

In recent years, TPMS have encountered increasing interest in the scientific world, due to the growing diffusion of Additive Manufacturing (AM). This new technique has a higher level of design freedom with respect to traditional methodologies such as Subtractive Manufacturing (SM) and this opens up the possibility of fabricating more complex objects at a similar cost [18]. In particular, TPMS structures are suitable to substitute porous media, that are usually made of particles randomly packed together, introducing regularity and this could be beneficial in many fields, since it gives the possibility to predict the behavior of the structure with more accuracy, knowing the exact shape.

TPMS are thus suitable for many applications. For example some recent studies in the bio-medical engineering showed that, due to their porosity, they can substitute bones lattices, giving the chance to effectively repair broken or damaged ones [19], [20]. More details are exposed in appendix (A).

In this work, TPMS have been studied as porous media equipping a cooling channel, to generate an efficient heat sink. TPMS structures can be generated from the minimal surface in two ways. In fact, it splits the space in two volumes, as shown for the *Gyroid* in figure (1.2c). The first possibility is to fill one of the two volumes with solid (figure (1.3a)), generating a single channel structure. This is usually referred to as *solid-TPMS*.

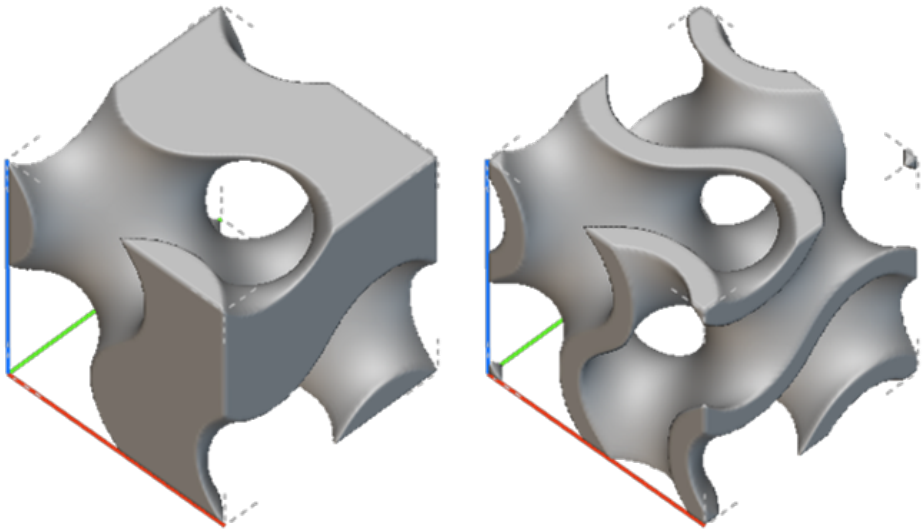

(a) **(b)**

Figure 1.3: *Example of the difference between solid (a) and sheet (b) TPMS for Gyroid*

The second possibility is to extrude the iso-surface (figure (1.3b)) generating a wall that separates two parallel channels and this is called *sheet-TPMS*. This second configuration has been widely analyzed in the field of heat exchangers since the presence of two channels is suitable for that purpose too. Many researches have focused on the design, test and simulation especially of *Gyroid*-based heat exchangers. For example, Peng et al. in 2019 [21] and subsequently also Dixit et al. in 2022 [22] evaluated computationally and experimentally the performances of such a heat exchanger in laminar flow regime, showing improvement with respect to traditional ones in terms of thermal performances and studied its manufacturability.

In other works, such as Kim et al. in 2020 [23] (experimentally) and of Alteneiji et al. in 2022 [24] (numerically), the performances of *Gyroid*-based heat exchangers have been compared to the ones obtained with *Primitive* and *Diamond*.

In the field of heat sinks applications, the *Diamond* and *Gyroid* structures have been analyzed in some studies, both in the form of *sheet-TPMS* and in the form of *solid-TPMS*, as in Al-Ketan et al. in 2021 [25] and Baobaid et al. in 2022 [27], revealing some differences between them and a generally better behavior with respect to conventional heat sinks. However, the thermal-hydraulic advantages and disadvantages of one with respect to the other, when used as heat sinks, are not completely clear and further investigation is needed. In the present study, all the considered structures are *sheet-TPMS*.

1.2 Objective of the work

The present work aims at assessing the hydraulic and thermal performances of Triply Periodic Minimal Surfaces, comparing different types and configurations, in a simplified domain, such as a circular channel, in turbulent regime.

Four types of TPMS structures have been studied, implementing a parametric analysis of the effect of the unit cell dimension (and therefore of the porosity) on thermal-hydraulic variables, highlighting the advantages and drawbacks of every structure.

All the simulations have been performed using the Computational Fluid Dynamics (CFD) tool *STAR-CCM+* [8].

Chapter 2

Configurations

To characterize the performance of the TPMS-based structures, the same channel has been equipped with different configurations. The dimensions of the employed circular channel, presented in figure (2.1), are listed below:

- internal diameter $5.08\,cm$ ($2\,inches$)
- wall thickness $1\,mm$
- length $10.2\,cm$ (around $4\,inches$)
- TPMS insert length $10\,cm$

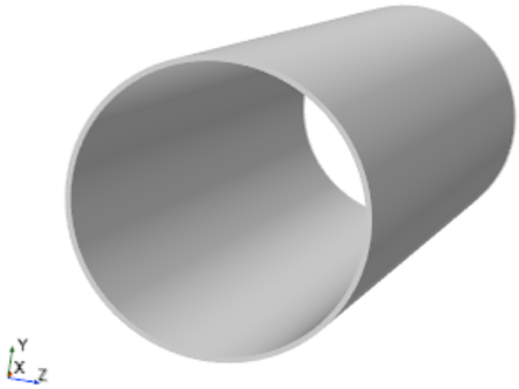

Figure 2.1: *Circular channel wall*

The TPMS length has been set $2\,mm$ shorter than the channel total one to facilitate the computational mesh procedure.

Firstly, four types of TPMS have been analyzed varying the unit cell size, in section (2.1). For one of them (*Gyroid*), a parametric study on the channel shape has been also performed (2.3). Lastly, the possibility of combining different TPMS together to optimize their behavior has been investigated (2.2).

2.1 Single TPMS structures

The *Gyroid* is the most popular TPMS in the cooling field and it is especially used for heat exchangers, as for example studied in [24] and [26]. However, other types of TPMS can have interesting thermal-hydraulic performance. In particular, the four considered *sheet-TPMS* are: *Diamond*, *Gyroid*, *Lidinoid* and *SplitP*. Their cubic unit cells are displayed in figure (2.2).

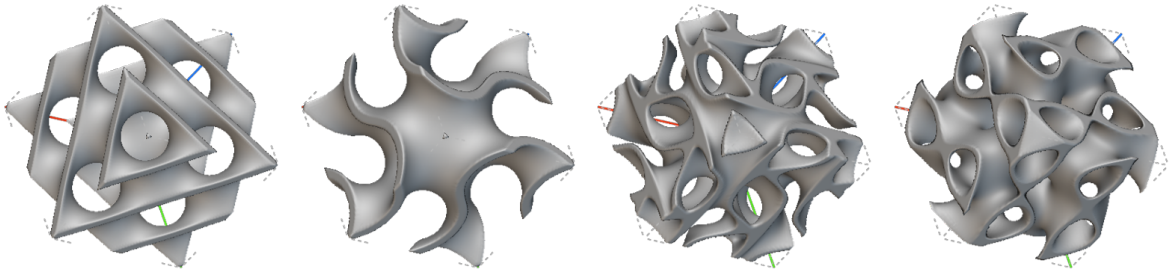

(a) *Diamond* **(b)** *Gyroid* **(c)** *Lidinoid* **(d)** *SplitP*

Figure 2.2: *Unit cells of studied TPMS*

All these surfaces are generated starting from specific mathematical equations. Table (2.1) presents the functional equations used to build standard TPMS on *nTopology* [9].

Table 2.1: *TPMS generating functions*

Structure name	**Generating function**
Diamond	$sin(x) \cdot sin(y) \cdot sin(z) + sin(x) \cdot cos(y) \cdot cos(z) + cos(x) \cdot sin(y) \cdot cos(z) + cos(x) \cdot cos(y) \cdot sin(z)$
Gyroid	$sin(x) \cdot cos(y) + sin(y) \cdot cos(z) + sin(z) \cdot cos(x)$
Lidinoid	$sin(2x) \cdot cos(y) \cdot sin(z) + sin(2y) \cdot cos(z) \cdot sin(x) + sin(2z) \cdot cos(x) \cdot sin(y) - cos(2x) \cdot cos(2y) - cos(2y) \cdot cos(2z) - cos(2z) \cdot cos(2x) + 0.3$
SplitP	$1.1 \cdot (sin(2x \cdot sin(z) \cdot cos(y) + sin(2y) \cdot sin(x) \cdot cos(z) + sin(2z) \cdot sin(y) \cdot cos(x)) - 0.2 \cdot (cos(2x) \cdot cos(2y) + cos(2y) \cdot cos(2z) + cos(2z) \cdot cos(2x)) - 0.4 \cdot (cos(2x) + cos(2y) + cos(2z))$

The average wall thickness has been set equal to $1\,mm$ for all the cases, while three values of unit cell size s have been studied for each TPMS type:

- $10mm \cdot 10mm \cdot 10mm$
- $15mm \cdot 15mm \cdot 15mm$
- $20mm \cdot 20mm \cdot 20mm$

The geometries for the simulations have been generated using the *nTopology* software in Cartesian coordinates within a parallelepiped and then intersected with the cylindrical domain to extract the final shape of the TPMS, as illustrated in figure (2.3) for the *Gyroid* case.

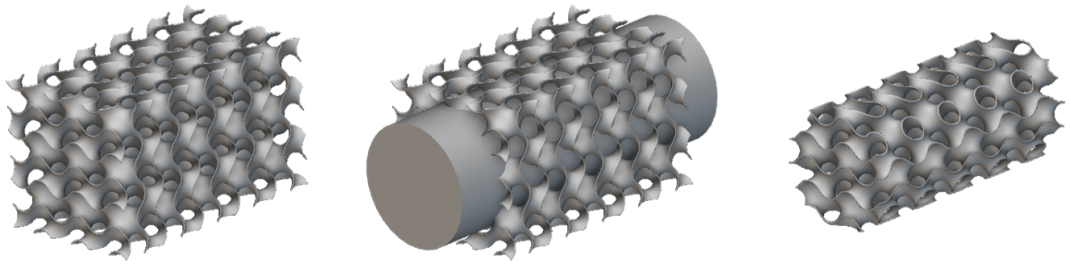

(a) *TPMS in the parallelepiped* **(b)** *Intersection* **(c)** *TPMS in the cylinder*

Figure 2.3: *Phases of the TPMS structure generation for Gyroid*

In total, 12 configurations have been analyzed (4 TPMS types for 3 values of unit cell size) and they are all presented in their front and side views respectively in figures (2.5) and (2.6). From the front view, it is observable that all the structures except the *Diamond* have some channels that extend straight forward from the inlet to the outlet (holes with white background within the TPMS). Moreover, from figure (2.6), it is evident that the level of complexity is not the same for all the structures, but it is higher for *Lidinoid* and *SplitP*.

TPMS-based structures are considered porous media, thus a porosity value can be associated to each of them. In particular, table (2.2) reports the values related to all the studied configurations, computed as in equation (2.1), where V_{fluid} and V_{solid} are respectively the fluid and solid volume, while V_{total} is the total volume of the channel. The values of porosity originating from *Gyroid* and *Diamond* are higher with respect to the other two structures.

$$\phi = \frac{V_{fluid}}{V_{total}} = 1 - \frac{V_{solid}}{V_{total}} \tag{2.1}$$

The volume occupied by TPMS-based structures is small, that means a moderate amount of material should be exploited to construct them. The absolute and percentage values of the solid volume in a cubic unit cell are reported in table (2.2).

The hydraulic diameter inside the TPMS structure has been computed as in equation (2.2), that is an alternative formulation of the standard one $4A_{sec}/P$ to be applied when the cross section area A_{sec} and the perimeter P are not constant along the channel length. Instead, it uses the fluid volume V_{fluid} and the total wetted area A_{wet}. The values are all collected in table (2.2). The hydraulic diameter results significantly smaller than the channel diameter ($50.8\,mm$). Again, as for the porosity, the larger values are the ones corresponding to the *Gyroid* structures, followed by *Diamond*.

$$D_h = \frac{4V_{fluid}}{A_{wet}} \tag{2.2}$$

One of the peculiarities of TPMS is a large surface-area-to-volume ratio, that permits them to be compact, light and suitable for thermal applications. The values for the four studied structures, computed on the single unit cells, are collected in table (2.2). In this case, the highest values are the ones of *SplitP* and *Lidinoid*. Thus it is possible to expect better thermal performances from these latter than from the other two.

In figure (2.4), the porosity and the surface-area-to-volume ratio are presented graphically. It is possible to infer that both of them are non-linearly depending from the unit cell size.

Moreover, the rate of change is different according to the TPMS type, and this is particularly evident for the case of *SplitP* surface-area-to-volume ratio.

Table 2.2: *Porosity, solid volume in a unit cell, fluid volume of the channel, total wetted area, hydraulic diameter and surface-area-to-volume ratio of Diamond (D), Gyroid (G), Lidinoid (L) and SplitP (S) structures, depending on the unit cell size s*

	$s\,[mm]$	$\phi\,[\%]$	$V_{solid}\,[mm^3]$ (%)	$V_{fluid}\,[mm^3]$	$A_{wet}\,[m^2]$	$D_h\,[mm]$	$A_{surf}/V\,[m^{-1}]$
D	10	76.8	231.9 (23%)	$1.56 \cdot 10^5$	0.164	3.79	3684
	15	84.5	521.0 (15%)	$1.71 \cdot 10^5$	0.117	5.86	3564
	20	88.4	927.1 (12%)	$1.79 \cdot 10^5$	0.0918	7.81	3509
G	10	80.7	193.7 (19%)	$1.63 \cdot 10^5$	0.137	4.79	3632
	15	87.1	434.5 (13%)	$1.77 \cdot 10^5$	0.0970	7.28	3519
	20	90.3	770.3 (10%)	$1.83 \cdot 10^5$	0.0775	9.45	3460
L	10	71.3	287.6 (29%)	$1.44 \cdot 10^5$	0.235	2.46	4475
	15	78.4	729.3 (22%)	$1.59 \cdot 10^5$	0.170	3.73	3964
	20	82.6	1400 (18%)	$1.67 \cdot 10^5$	0.134	4.99	3677
S	10	73.7	262.3 (26%)	$1.49 \cdot 10^5$	0.213	2.81	4335
	15	82.7	589.4 (17%)	$1.68 \cdot 10^5$	0.149	4.49	4229
	20	87.0	1046 (13%)	$1.76 \cdot 10^5$	0.117	6.02	4144

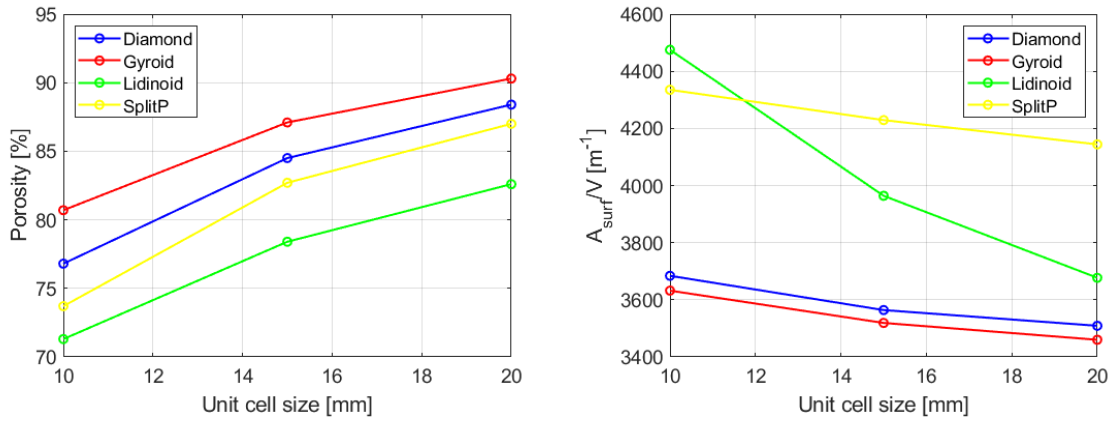

(a) **(b)**

Figure 2.4: *Porosity (a) and surface-area-to-volume ratio (b) depending on the unit cell size*

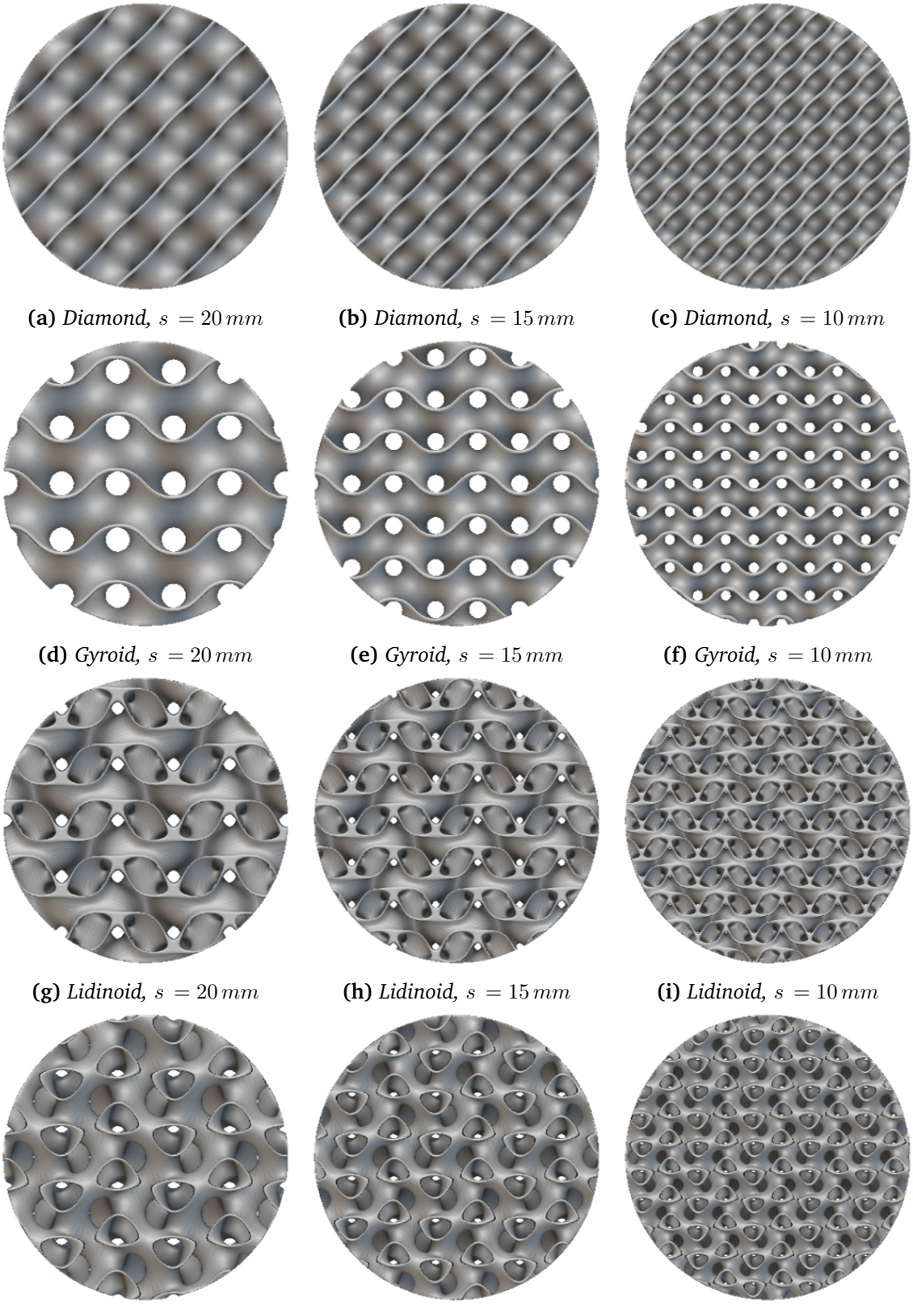

(a) *Diamond,* $s = 20\,mm$ **(b)** *Diamond,* $s = 15\,mm$ **(c)** *Diamond,* $s = 10\,mm$

(d) *Gyroid,* $s = 20\,mm$ **(e)** *Gyroid,* $s = 15\,mm$ **(f)** *Gyroid,* $s = 10\,mm$

(g) *Lidinoid,* $s = 20\,mm$ **(h)** *Lidinoid,* $s = 15\,mm$ **(i)** *Lidinoid,* $s = 10\,mm$

(j) *SplitP,* $s = 20\,mm$ **(k)** *SplitP,* $s = 15\,mm$ **(l)** *SplitP,* $s = 10\,mm$

Figure 2.5: *Front view of the twelve TPMS configurations, Diamond ((a), (b), (c)), Gyroid ((d), (e), (f)), Lidinoid ((g), (h), (i)) and SplitP ((j), (k), (l)) with three unit cell sizes*

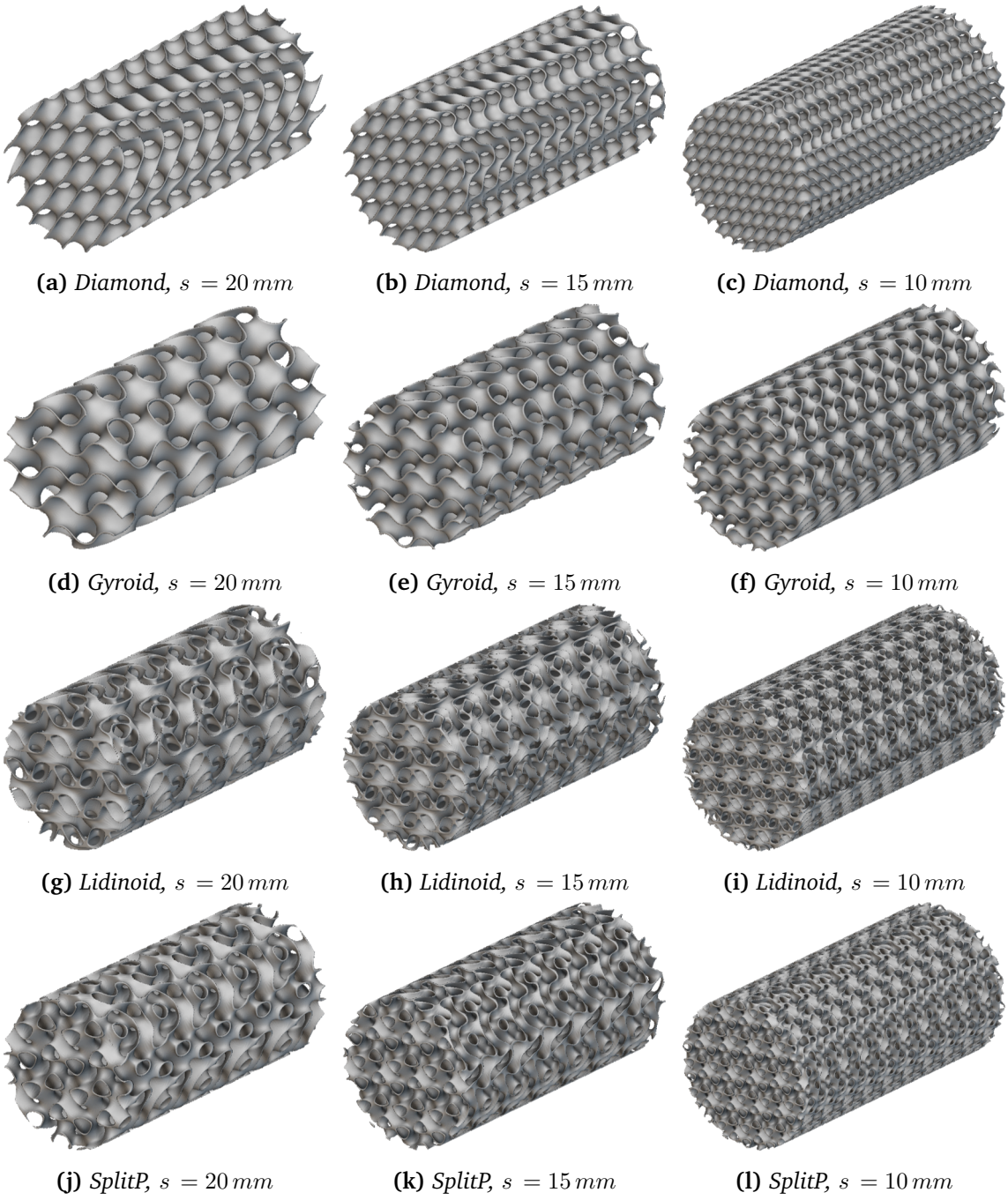

(a) *Diamond,* $s = 20\,mm$ **(b)** *Diamond,* $s = 15\,mm$ **(c)** *Diamond,* $s = 10\,mm$

(d) *Gyroid,* $s = 20\,mm$ **(e)** *Gyroid,* $s = 15\,mm$ **(f)** *Gyroid,* $s = 10\,mm$

(g) *Lidinoid,* $s = 20\,mm$ **(h)** *Lidinoid,* $s = 15\,mm$ **(i)** *Lidinoid,* $s = 10\,mm$

(j) *SplitP,* $s = 20\,mm$ **(k)** *SplitP,* $s = 15\,mm$ **(l)** *SplitP,* $s = 10\,mm$

Figure 2.6: *Side view of the twelve TPMS configurations, Diamond ((a), (b), (c)), Gyroid ((d), (e), (f)), Lidinoid ((g), (h), (i)) and SplitP ((j), (k), (l)) with three unit cell sizes*

2.2 TPMS combinations

The four TPMS have different behaviors in terms of pressure drop and channel external surface temperature, as it is possible to infer from the geometrical characteristics shown in the previous sections and as confirmed by some preliminary simulations.

In particular, due to the higher porosity, *Diamond* and *Gyroid* are expected to produce a smaller pressure drop, at the expense of worse thermal performances. Thus, the combination of two types of TPMS, with different unit cell sizes, may be beneficial. Four types of combinations are here proposed and analyzed. Their configurations are reported in table (2.3).

Table 2.3: *TPMS combinations*

Name	Core region ($15mm \cdot 15mm \cdot 15mm$)	Outer layer ($10mm \cdot 10mm \cdot 10mm$)
D-L	Diamond	Lidinoid
D-S	Diamond	SplitP
G-L	Gyroid	Lidinoid
G-S	Gyroid	SplitP

The cylindrical domain is radially divided in two regions, the core (radius $23\,mm$) and an outer layer (thickness $2.4\,mm$). This values have been selected as first trials, with a ratio of approximately $1/10$. *Diamond* and *Gyroid* with unit cell size of $15\,mm$ have been chosen to equip the central part, while *Lidinoid* and *SplitP* with unit cell size of $10\,mm$ have been put in the outer layer, to better improve the turbulence and heat exchange mechanisms next to the wall. The expectation is that the pressure drop will be driven by the core region TPMS, while the thermal performances from the outer layer.

The inlet cross sections of these four configurations are shown in figure (2.7).

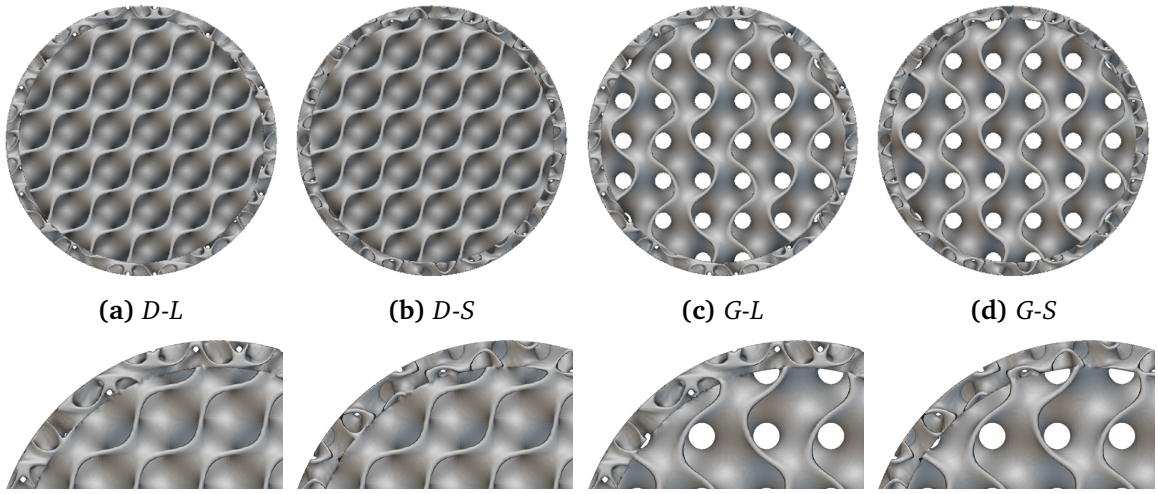

(a) *D-L* **(b)** *D-S* **(c)** *G-L* **(d)** *G-S*

(e) *D-L* **(f)** *D-S* **(g)** *G-L* **(h)** *G-S*

Figure 2.7: *Inlet cross sections of the four TPMS combinations and their magnifications, Diamond-Lidinoid ((a),(e)), Diamond-SplitP ((b),(f)), Gyroid-Lidinoid ((c),(g)) and Gyroid-SplitP ((d),(h))*

The geometrical characteristics, that are mainly depending on the core region, are reported in table (2.4).

Table 2.4: *Porosity, solid and fluid volume of the channel, total wetted area, hydraulic diameter and surface-area-to-volume ratio of the four TPMS combinations*

Name	$\phi\,[\%]$	$V_{solid}\,[mm^3]$ (%)	$V_{fluid}\,[mm^3]$	$A_{wet}\,[m^2]$	$D_h\,[mm]$	$A_{surf}/V\,[m^{-1}]$
D-L	81.8	$3.68 \cdot 10^4$ (18.2%)	$1.66 \cdot 10^5$	0.143	4.65	3874
D-S	82.3	$3.58 \cdot 10^4$ (17.7%)	$1.67 \cdot 10^5$	0.139	4.80	3883
G-L	83.9	$3.27 \cdot 10^4$ (16.1%)	$1.70 \cdot 10^5$	0.127	5.37	3880
G-S	84.4	$3.17 \cdot 10^4$ (15.6%)	$1.71 \cdot 10^5$	0.123	5.55	3891

2.3 Comparison of three channel shapes

Three channels with the same length ($10.2\,cm$) but different section shapes have been designed, respectively circular (diameter $D = 5.08\,cm$), square (side $L = 5.08\,cm$) and rectangular with aspect ratio 2 (maximum and minimum sides $L_{MAX} = 7.62\,cm$ and $L_{min} = 3.81\,cm$). The analysis has been performed on *Gyroid* only, considering five unit cell dimensions (10, 15, 20, 25 and $30\,mm$), to assess the dependence of the hydraulic characteristic on the channel shape in these cases. The inlet cross sections of the three channels are shown in figure (2.9).

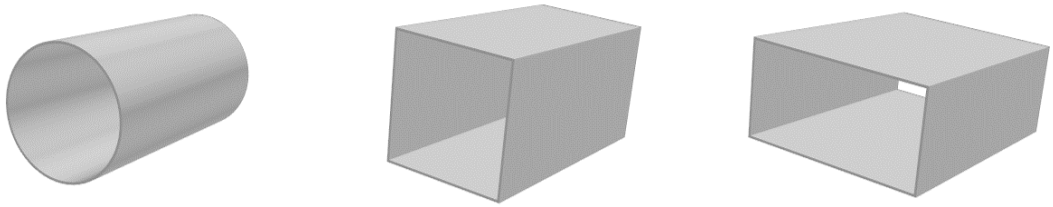

(a) **(b)** **(c)**

Figure 2.8: *Circular (a), square (b) and rectangular (c) channels*

The values of porosity and hydraulic diameter inside the TPMS structure corresponding to the unit cell sizes are reported in table (2.5), computed respectively as in equations (2.1) and (2.2).

Table 2.5: *Porosity and hydraulic diameter of the three channels equipped with Gyroid*

s	$\phi\,[\%]$	$D_h\,[mm]$
10	80.6	4.79
15	87.1	7.27
20	90.4	9.51
25	92.3	11.5
30	93.6	13.4

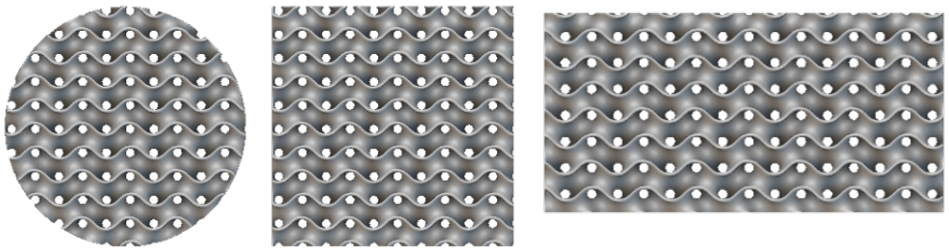

(a) *Circular* $10\,mm$ **(b)** *Square* $10\,mm$ **(c)** *Rectangular* $10\,mm$

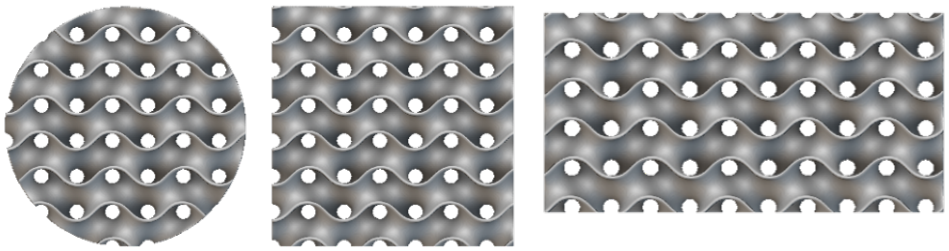

(d) *Circular* $15\,mm$ **(e)** *Square* $15\,mm$ **(f)** *Rectangular* $15\,mm$

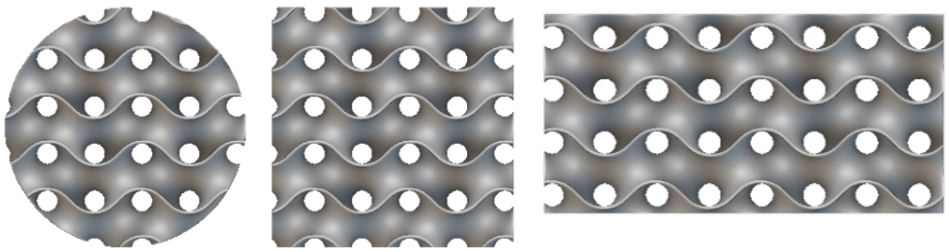

(g) *Circular* $20\,mm$ **(h)** *Square* $20\,mm$ **(i)** *Rectangular* $20\,mm$

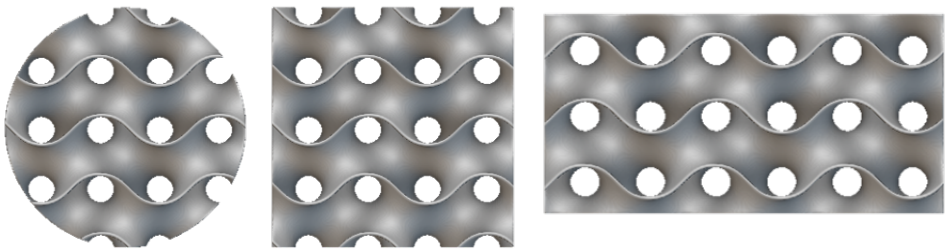

(j) *Circular* $25\,mm$ **(k)** *Square* $25\,mm$ **(l)** *Rectangular* $25\,mm$

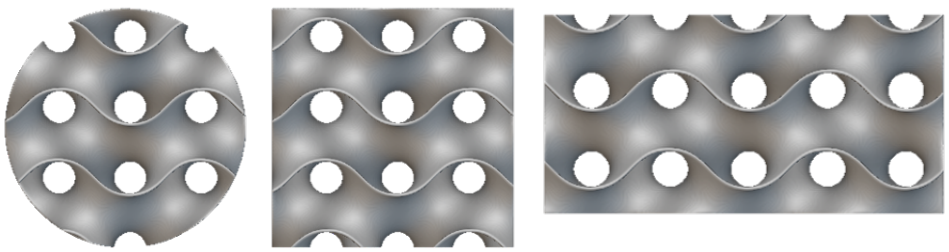

(m) *Circular* $30\,mm$ **(n)** *Square* $30\,mm$ **(o)** *Rectangular* $30\,mm$

Figure 2.9: *Inlet sections of the circular ((a),(d),(g),(j),(m)), square ((b),(e),(h),(k),(n)) and rectangular ((c),(f),(i),(l),(o)) channels*

Chapter 3

Simulations setup

This chapter is devoted to the description of the simulation settings concerning the fluid and solid models (3.1), the boundary conditions (3.2) and the mesh (3.3).

3.1 Models and properties

To simulate the *conjugate heat transfer* between fluid and solid, water has been considered at *constant density*, flowing through the structures in *steady state* conditions.
Due to the characteristics of the problem, the *coupled flow* approach is not needed, because the velocity field is not directly depending on the density field, as occurs instead in some free convection problems. Thus, a *segregated* approach that is less computational expensive has been chosen. The same settings (*constant density* and *steady state*) have been chosen for the solid domain, simulated using the default *Copper* properties provided by the software.
For what concerns the energy, the *segregated fluid temperature* and *segregated solid energy* options have been set.

3.1.1 Turbulence models

Due to the chosen mass flow rate values and to the presence of the TPMS structures, the flow regime inside the pipe is turbulent. Thus, it is necessary to numerically solve Reynolds Average Navier-Stokes (RANS) set of equations, shown in (3.1).

$$
\begin{aligned}
div\mathbf{U} &= 0 \\
\frac{\partial U}{\partial t} + div(U\mathbf{U}) &= -\frac{1}{\rho}\frac{\partial P}{\partial x} + \nu div(grad(U)) + \frac{1}{\rho}\left[\frac{\partial(-\rho\overline{u'^2})}{\partial x} + \frac{\partial(-\rho\overline{u'v'})}{\partial y} + \frac{\partial(-\rho\overline{u'w'})}{\partial z}\right] \\
\frac{\partial V}{\partial t} + div(V\mathbf{U}) &= -\frac{1}{\rho}\frac{\partial P}{\partial y} + \nu div(grad(V)) + \frac{1}{\rho}\left[\frac{\partial(-\rho\overline{u'v'})}{\partial x} + \frac{\partial(-\rho\overline{v'^2})}{\partial y} + \frac{\partial(-\rho\overline{v'w'})}{\partial z}\right] \\
\frac{\partial W}{\partial t} + div(W\mathbf{U}) &= -\frac{1}{\rho}\frac{\partial P}{\partial z} + \nu div(grad(W)) + \frac{1}{\rho}\left[\frac{\partial(-\rho\overline{u'w'})}{\partial x} + \frac{\partial(-\rho\overline{v'w'})}{\partial y} + \frac{\partial(-\rho\overline{w'^2})}{\partial z}\right]
\end{aligned}
\tag{3.1}
$$

U is the mean velocity vector, with its mean components *U*, *V* and *W*, while *u'*, *v'* and *w'* are the fluctuating components of the velocity, *P* is the pressure, ρ is the fluid density and ν is its kinematic viscosity [31].

To solve computationally the set of equations (3.1), one of the most widely used option is to introduce two additional transport equations (3.2), for the turbulent kinetic energy (k) and the rate of dissipation of turbulent kinetic energy (ϵ), known as $k-\epsilon$ model. C_μ, $C_{1\epsilon}$, $C_{2\epsilon}$, σ_ϵ and σ_k are adjustable constants, whose values were derived through data fitting of many turbulent flow cases, while μ_t is the eddy viscosity and S_{ij} is the mean component of the rate of deformation of a fluid element [31].

$$\begin{aligned}
&\frac{\partial(\rho k)}{\partial t} + div(\rho k\mathbf{U}) = div\left[\frac{\mu_t}{\sigma_k} grad(k)\right] + 2\mu_t S_{ij}\cdot S_{ij} - \rho\epsilon \\
&\frac{\partial(\rho \epsilon)}{\partial t} + div(\rho \epsilon\mathbf{U}) = div\left[\frac{\mu_t}{\sigma_\epsilon} grad(\epsilon)\right] + C_{1\epsilon}\frac{\epsilon}{k}2\mu_t S_{ij}\cdot S_{ij} - C_{2\epsilon}\rho\frac{\epsilon^2}{k} \\
&\mu_t = \rho C_\mu \frac{k^2}{\epsilon}
\end{aligned} \tag{3.2}$$

As an alternative, ϵ can be substituted with the turbulence frequency, $\omega = \epsilon/k$, to obtain the set of equations (3.3) [31]. Models belonging to this family are called $k-\omega$.

$$\begin{aligned}
&\frac{\partial(\rho k)}{\partial t} + div(\rho k\mathbf{U}) = div\left[\left(\mu + \frac{\mu_t}{\sigma_k}\right) grad(k)\right] + P_k - \beta^*\rho k\omega \\
&\frac{\partial(\rho \omega)}{\partial t} + div(\rho \omega\mathbf{U}) = div\left[\left(\mu + \frac{\mu_t}{\sigma_\omega}\right) grad(\omega)\right] + \gamma_1\left(2\rho S_{ij}\cdot S_{ij} - \frac{2}{3}\rho\omega\frac{\partial U_i}{\partial x_j}\delta_{ij}\right) - \beta_1\rho\omega^2 \\
&P_k = 2\mu_t S_{ij}\cdot S_{ij} - \frac{2}{3}\rho k\frac{\partial U_i}{\partial x_j}\delta_{ij}
\end{aligned} \tag{3.3}$$

The values of the constants σ_k, σ_ω, γ_1, β_1 and β^* are reported in table (3.1) together with the ones of the $k-\epsilon$ model.

Table 3.1: *Models constants values [31]*

Model	Constants				
$k-\epsilon$	$C_\mu = 0.09$	$\sigma_k = 1.00$	$\sigma_\epsilon = 1.30$	$C_{1\epsilon} = 1.44$	$C_{2\epsilon} = 1.92$
$k-\omega$	$\sigma_k = 2.0$	$\sigma_\omega = 2.0$	$\gamma_1 = 0.553$	$\beta_1 = 0.075$	$\beta^* = 0.09$

In particular *Lag Elliptic Blending* $k-\epsilon$ has been chosen for this work (T1 in the following). It is an elliptic-blending (EB) lag model, developed to keep into account the misalignment of the principal components of the strain and stress tensors [32]. This results in two equations added to the $k-\epsilon$ set. The first one is a transport equation of ϕ, that represents the lag effect on the eddy-viscosity, while the second one is an elliptic equation for the blending parameter α [32]. It has been chosen to model TPMS, because, as stated in [32], this model should be robust for complex flow configurations, such as the one considered in the present work.

For some simulations, a comparison between *Lag-EB* $k-\epsilon$ and the *SST (Menter)* $k-\omega$ has been performed (T2 in the following). This second model is a hybrid Shear Stress Transport

(SST) that combines a $k-\omega$ model next to the wall and a $k-\epsilon$ one in the free stream region. This gives a more accurate description of the flow next to the wall in case of adverse pressure gradients, with respect to $k-\epsilon$ models and the results are less dependent on the free stream (arbitrary) values that are required for the original (Wilcox) $k-\omega$. Moreover, the presence of blending functions gives as outcome a smooth transition between the two models [31].

It has been already shown that *Lag-EB* $k-\epsilon$ is more suitable than the *SST* $k-\omega$ model in case of complex cooling configurations, such as a set of mini-channels in parallel [33].

The $all-Y^+$ approach has been implemented as wall treatment method, since it adapts well to different cells densities next to the wall and correspondent Y^+ values [8].

3.2 Boundary conditions and drivers

The conditions imposed to the boundaries are common to all the simulations and are listed below:

- Fully-developed velocity profile at the inlet
- Uniform pressure of $3\,bar$ at the outlet
- Inlet temperature $300\,K$
- Conjugate heat transfer at the fluid-solid interface
- Adiabatic conditions on all the other solid boundaries

To compute the velocity fully-developed profile, some preliminary simulations have been performed on shorter channels with *periodic* boundary condition at inlet and outlet. Then the three components of the velocity have been extracted on a plane and imported in the other simulations.

On the external wall of the channel, a heat flux of $1\,MW/m^2$ has been imposed for the thermal-hydraulic simulations.

3.3 Mesh

To perform the numerical simulations, a polyhedral mesh has been applied to the computational domain. The *automated mesh* approach has been used in the fluid and solid region where the TPMS-based structures are present (pink in figure (3.1) that shows the fluid only, for the *Diamond* case with unit cell size of $20\,mm$). Then two *volume extrusions* of the mesh on the inlet and outlet faces have been executed (grey in figure (3.1)), to assure fully-developed conditions of the flow and facilitate the convergence.

The results presented in the next chapters have been obtained on a mesh whose settings are as follows:

- Base size: $0.6\,mm$
- Target surface size: 100%
- Minimum surface size: 20%

- Surface growth rate: 1.3
- Number of prism layers: 8
- Prism layer near wall thickness: $5 \cdot 10^{-3}\, mm$
- Prism layers total thickness: $0.3\, mm$

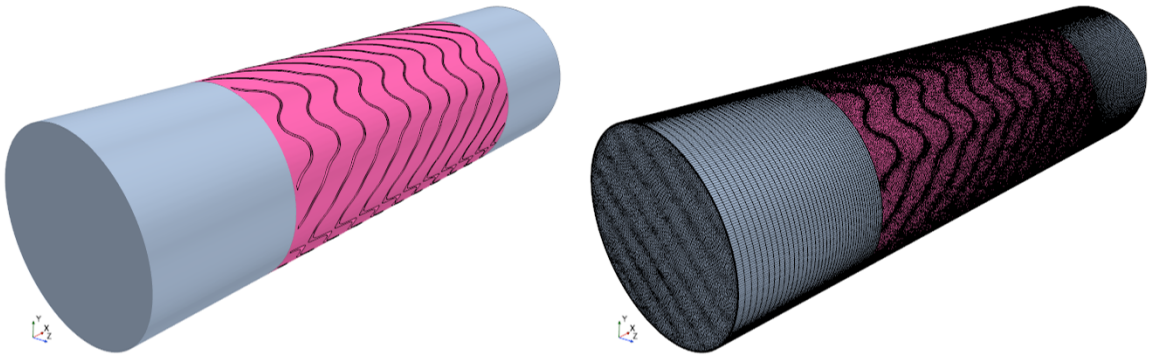

(a) **(b)**

Figure 3.1: *Geometry (a) and mesh (b) view on the fluid and extrusions external surface, for the Diamond with unit cell of* $20\, mm$ *case*

Figure (3.2) shows the mesh on a general cross section for the case of *Diamond* with unit cell size $20\, mm$, together with a magnification to highlight the presence of the prism layers at the boundaries of the fluid region.

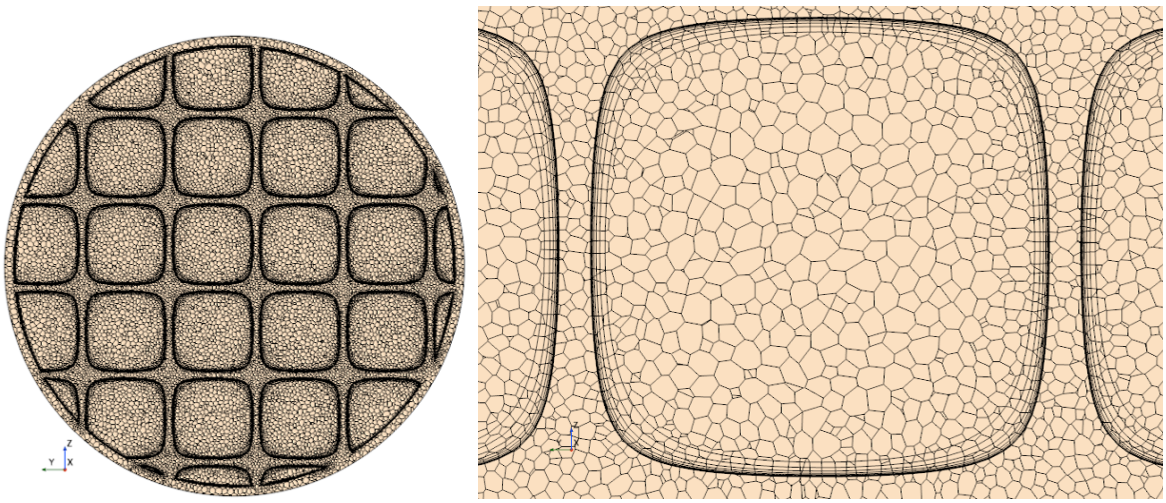

(a) **(b)**

Figure 3.2: *Mesh on a cross section (a) and its magnification (b), for the Diamond with unit cell of* $20\, mm$ *case*

The extrusions have been generated with the *Surface Extrusion* operation, along a length of $0.04\, m$ and have been meshed via a *Volume Extruder* with the following settings:

- Number of layers: 40
- Stretching function: one-sided geometric progression
- First layer thickness: $0.6\,mm$

3.3.1 Solution verification

To perform the verification of the simulations, four meshes have been generated for each configuration with the settings reported in detail in the following. The numerical uncertainty has been estimated on the pressure drop for the single TPMS and the three channels configurations, and on the solid temperature for the single TPMS with unit cell size of $15\,mm$, as discussed more in detail in the next sections.

To estimate the uncertainty, the Grid Convergence Index (GCI) has been computed following the procedure suggested in [34].

First of all it is necessary to define the average mesh cell size h as in equation (3.4), where V_{meshed} is the total meshed volume and N is the number of cells.

$$h = \left(\frac{V_{meshed}}{N}\right)^{1/3} \tag{3.4}$$

$$GCI_{21} = \frac{F_s \cdot |\epsilon_{r,21}|}{(r_{21}^c - 1)} \tag{3.5}$$

Considering as meshes 1 and 4 respectively the finest and the coarsest one, GCI related to the variable ϕ can be obtained from equation (3.5), where F_s is the Factor of Safety and it is assumed equal to 1.25, $\epsilon_{r,21}$ is the relative error between the two finest meshes, r_{21} is the ratio between h_2 and h_1, while c is the observed convergence order. To compute this latter, the Least Squares Method has been applied. Starting from the one-term expansion of the discretization error (equation (3.6)), this method is based on the minimization of the S function in equation (3.7), where N_g is the number of grids, ϕ_i and ϕ_∞ are respectively the value related to mesh i and the extrapolated value of the studied variable and α is a coefficient. Through an iterative process it is possible to find the values that minimize S. Note that, as stated in [34], c should be limited to its theoretical value that for this type of problems is 2.

$$\phi_i - \phi_\infty \cong \alpha \cdot h_i^c \tag{3.6}$$

$$S(\phi_\infty, \alpha, p) = \sqrt{\sum_{i=1}^{N_g} [\phi_i - (\phi_\infty + \alpha \cdot h_i^c)]^2} \tag{3.7}$$

Finally, the relative numerical uncertainty can be estimated as in equation (3.8), where the expansion factor k is taken equal to 1.15.

$$u_{num} = \frac{GCI}{k} \tag{3.8}$$

Single TPMS structures

The numerical uncertainty has been estimated on the pressure drop (computed between the two sections in figure (4.1), as discussed in the results chapter (4)) for all the configurations and on the maximum and average external wall temperature increase, with respect to the inlet temperature, for the structures with mean TPMS unit cell size ($15\,mm$), all at the intermediate value of mass flow rate ($1\,kg/s$). In order to evaluate the first one, hydraulic only simulations have been performed, refining the fluid domain mesh. The values of the number of cells and average cell size are displayed in tables (3.2) and (3.3). For the GCI evaluation on the temperature increase, thermal-hydraulic processes have been simulated and the number of cells and the mean cell dimension h, in table (3.5) refer to the entire fluid and solid domain.

Table 3.2: *Number of cells of fluid domain for all the configurations*

TPMS type	Mesh	$s = 10\,mm$	$s = 15\,mm$	$s = 20\,mm$
Diamond	1	34.0M	22.3M	17.3M
	2	29.2M	19.1M	14.8M
	3	25.7M	16.8M	13.1M
	4	22.3M	14.5M	11.4M
Gyroid	1	24.7M	17.5M	13.9M
	2	24.5M	14.9M	11.8M
	3	18.9M	13.2M	10.5M
	4	16.5M	11.5M	9.10M
Lidinoid	1	131M	83.5M	51.7M
	2	98.3M	62.6M	44.9M
	3	72.4M	51.8M	38.7M
	4	51.3M	37.3M	28.5M
SplitP	1	93.3M	25.2M	37.7M
	2	75.2M	19.8M	33.2M
	3	59.7M	15.7M	28.9M
	4	43.9M	12.3M	23.3M

It can be noticed that the number of cells generated in the *Lidinoid* structures is significantly larger than the others, with the same settings. This is due to its higher level of geometrical complexity, that forces the tool to refine the mesh.

In table (3.4) the GCI values computed on the pressure drop are collected. The four configurations with unit cell size of $20\,mm$ show the highest GCI, meaning that the numerical uncertainty is larger in those cases.

Figures (3.3) and (3.4) show the variation of the pressure drop depending on the mesh average cell dimension for all the twelve configurations. For some of them the convergence is more evident than for others and this justifies also the difference in the computed GCI values.

Table 3.3: *Mean cell dimension $[mm]$ of the fluid domain for all the configurations*

TPMS type	Mesh	$s = 10\,mm$	$s = 15\,mm$	$s = 20\,mm$
Diamond	1	0.166	0.197	0.218
	2	0.175	0.208	0.230
	3	0.182	0.217	0.239
	4	0.191	0.228	0.250
Gyroid	1	0.188	0.216	0.236
	2	0.197	0.228	0.250
	3	0.205	0.237	0.260
	4	0.215	0.249	0.272
Lidinoid	1	0.103	0.124	0.148
	2	0.114	0.136	0.155
	3	0.126	0.145	0.163
	4	0.141	0.162	0.180
SplitP	1	0.117	0.187	0.167
	2	0.126	0.204	0.174
	3	0.136	0.220	0.183
	4	0.150	0.239	0.196

Table 3.4: *GCI computed on pressure drop for the four TPMS types*

Unit cell size $[mm]$	Diamond	Gyroid	Lidinoid	SplitP
10	0.81%	3.35%	2.02%	2.10%
15	5.46%	2.79%	2.29%	1.94%
20	14.9%	11.4%	13.4%	31.0%

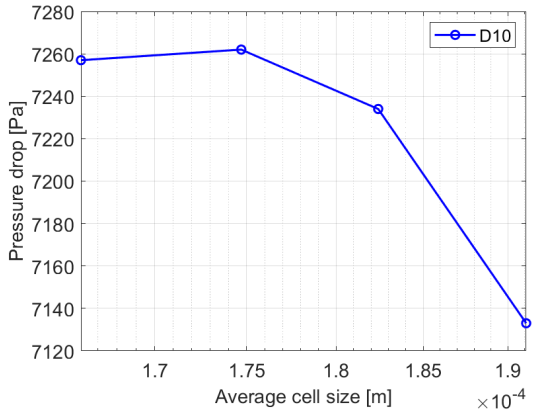

(a) *Diamond,* $s = 10\,mm$

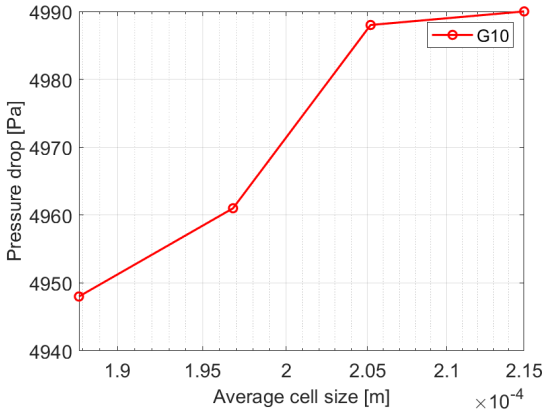

(b) *Gyroid,* $s = 10\,mm$

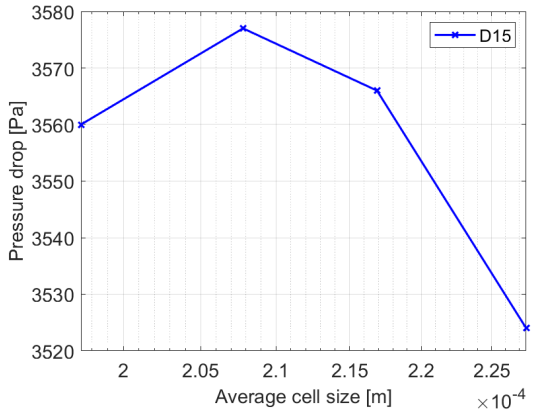

(c) *Diamond,* $s = 15\,mm$

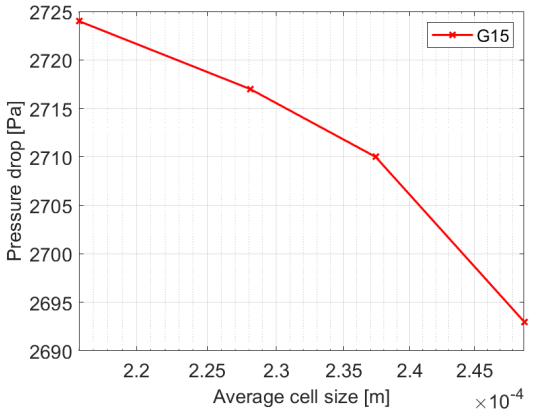

(d) *Gyroid,* $s = 15\,mm$

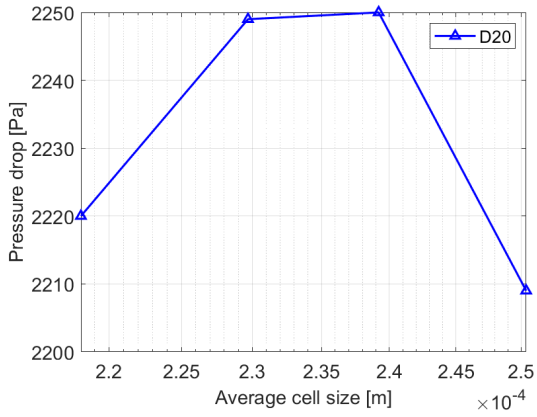

(e) *Diamond,* $s = 20\,mm$

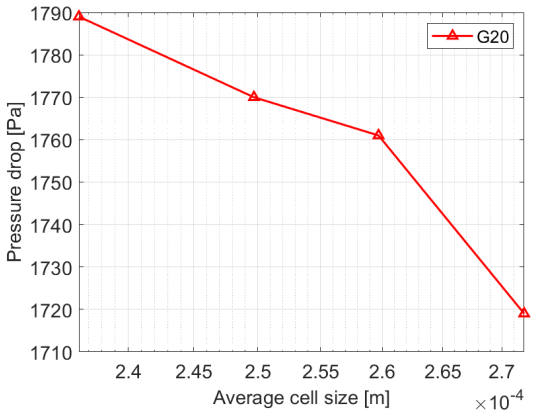

(f) *Gyroid,* $s = 20\,mm$

Figure 3.3: *Pressure drop at* $1\,kg/s$ *depending on the mesh cell dimension for Diamond ((a), (c), (e)) and Gyroid ((b), (d), (f))*

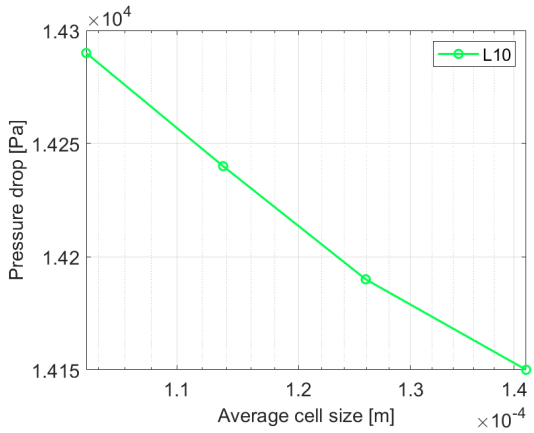

(a) *Lidinoid,* $s = 10\,mm$

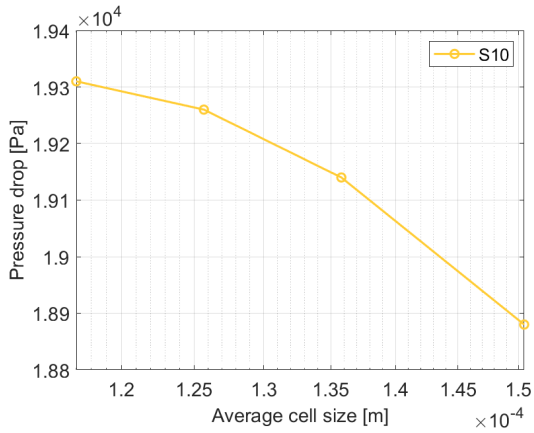

(b) *SplitP,* $s = 10\,mm$

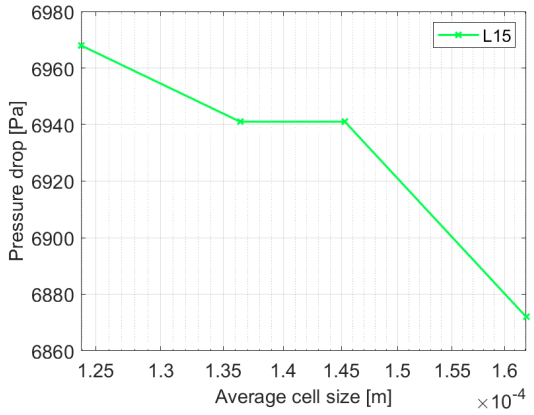

(c) *Lidinoid,* $s = 15\,mm$

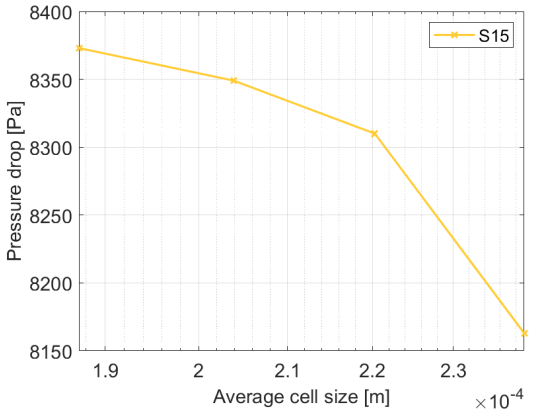

(d) *SplitP,* $s = 15\,mm$

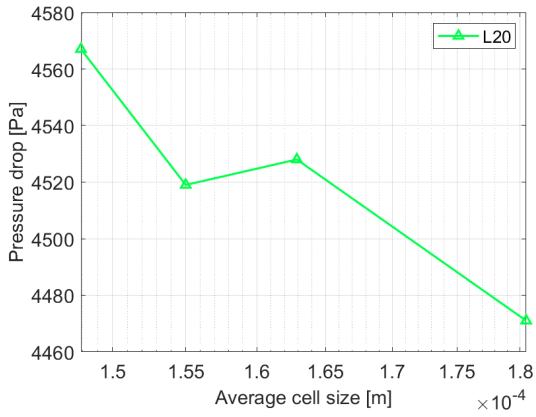

(e) *Lidinoid,* $s = 20\,mm$

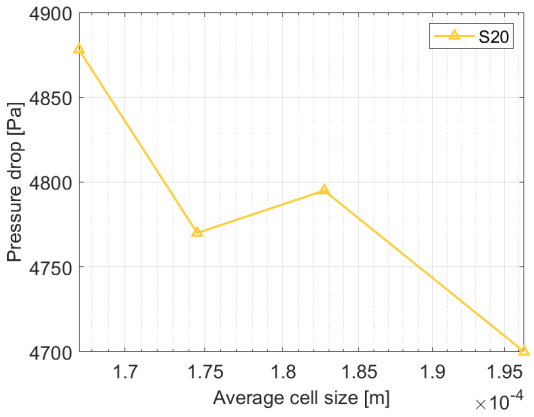

(f) *SplitP,* $s = 20\,mm$

Figure 3.4: *Pressure drop at* $1\,kg/s$ *depending on the mesh cell dimension for Lidinoid ((a), (c), (e)) and SplitP ((b), (d), (f))*

Table 3.5: *Number of cells and mean cell dimension of the whole domain for the four TPMS types with unit cell size* $15\,mm$

TPMS type	Mesh	N	$h\,[mm]$
Diamond	1	28.0M	0.193
	2	22.9M	0.207
	3	20.3M	0.215
	4	17.8M	0.225
Gyroid	1	22.1M	0.209
	2	18.0M	0.224
	3	16.0M	0.233
	4	14.1M	0.243
Lidinoid	1	96.1M	0.128
	2	73.6M	0.140
	3	61.3M	0.149
	4	44.7M	0.166
SplitP	1	33.6M	0.182
	2	27.0M	0.196
	3	22.3M	0.209
	4	18.1M	0.224

Table 3.6: *GCI computed on the external wall maximum and average temperature increase, with respect to the inlet one, for the four TPMS types with unit cell size 15 mm*

	Diamond	Gyroid	Lidinoid	SplitP
GCI on T_{max}	33.1%	14.7%	0.942%	2.87%
GCI on T_{avg}	26.3%	6.49%	3.89%	38.8%

Table (3.6) collects the GCI values computed on the external wall maximum and average temperature increases. The values are mostly higher than the ones computed on the pressure drop, a part from the *Lidinoid* ones, which instead shows a good convergence. This is also confirmed from the plots in figure (3.5). It has to be said that the maximum temperature increase may not be a significant parameter for the GCI estimation, since the hot spot does not necessarily occur in the same cell for all the simulations, thus, its variation may be not directly related to the mesh.

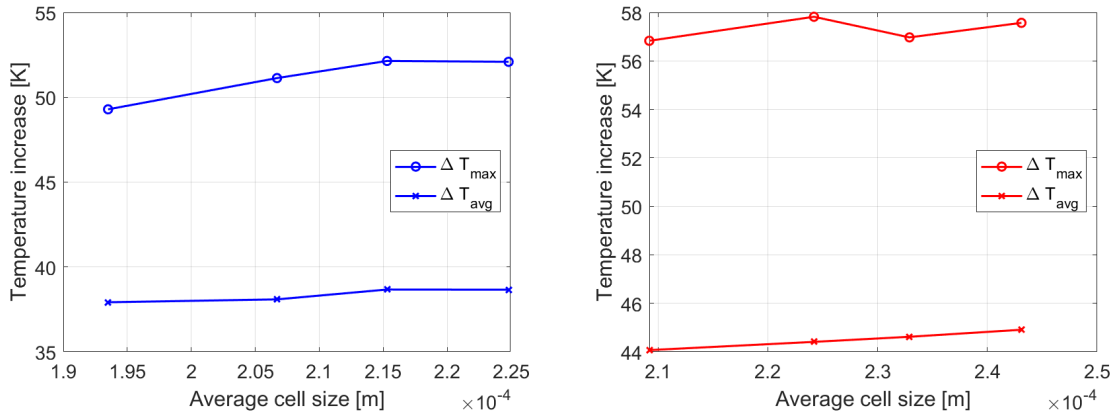

(a) *Diamond* **(b)** *Gyroid*

(c) *Lidinoid* **(d)** *SplitP*

Figure 3.5: *External wall maximum and average temperature increase at* $1\,kg/s$ *depending on the mesh mean cell dimension, for Diamond (a), Gyroid (b), Lidinoid (c) and SplitP (d) with unit cell size of* $15\,mm$

Comparison of three channel shapes

A GCI analysis has been performed also for the pressure drop obtained with the simulations on the three channels of different shapes equipped with *Gyroid*, both for *Lag-EB* $k-\epsilon$ and *SST* $k-\omega$ results. The number of cells and mean cell size for every configuration are shown in table (3.7). Even though the total number of cells differs from one channel to the other, the fact of having same hydraulic diameter and same mesh settings resulted in the same value of average cell dimension h for the three configurations.

The GCI values for the pressure drop resulted from the procedure exposed in section (3.3.1) are reported in table (3.8) both for *Lag-EB* $k-\epsilon$ and SST $k-\omega$ simulations.

Table 3.7: *Number of cells and mean cell dimension for the three channels equipped with Gyroid*

Unit cell size $s\,[mm]$	Mesh	Circular	Square	Rectangle	$h\,[mm]$
10	1	26.9M	34.6M	38.8M	0.182
	2	15.7M	20.3M	22.8M	0.217
	3	11.2M	14.6M	16.3M	0.243
	4	9.59M	12.5M	14.1M	0.256
15	1	19.3M	24.5M	27.5M	0.209
	2	10.4M	13.2M	14.7M	0.257
	3	4.90M	6.28M	6.92M	0.330
	4	3.50M	4.52M	4.98M	0.369
20	1	15.4M	19.5M	22.0M	0.228
	2	8.44M	10.6M	12.0M	0.279
	3	3.61M	4.57M	4.57M	0.370
	4	2.25M	2.87M	3.27M	0.433
25	1	12.8M	16.3M	18.2M	0.245
	2	7.00M	8.81M	9.80M	0.300
	3	2.93M	3.78M	4.10M	0.401
	4	1.76M	2.28M	2.48M	0.474
30	1	11.2M	14.3M	15.9M	0.257
	2	6.12M	7.89M	8.65M	0.314
	3	2.56M	3.33M	3.58M	0.420
	4	1.51M	1.98M	2.14M	0.501

Table 3.8: *GCI values for the three channels depending on the Gyroid unit cell size, computed on the simulations with Lag-EB* $k-\epsilon$

Turbulence model	Unit cell size $s\,[mm]$	Circular	Square	Rectangular
Lag-EB $k-\epsilon$	10	3.4%	1.5%	2.2%
	15	5.0%	0.28%	7.2%
	20	1.1%	9.7%	6.9%
	25	1.3%	1.4%	12%
	30	13%	19%	3.9%
SST $k-\omega$	10	1.4%	2.9%	1.3%
	15	6.2%	1.0%	12%
	20	44%	6.6%	3.4%
	25	9.2%	2.7%	1.3%
	30	66%	4.2%	15%

Chapter 4

Hydraulic results

The Reynolds number of the flow inside the TPMS can be computed as in equation (4.1), where P is the average wetted perimeter, that is substituted with the ratio between the total wetted area and the channel length (A_{wet}/L).

$$Re = \frac{4\dot{m}}{\mu P} = \frac{4\dot{m}L}{\mu A_{wet}} \tag{4.1}$$

The wetted area depends on the TPMS type and on its unit cell size, so to every configuration corresponds a different value of the Reynolds number. To clarify this, in figures (4.2), (4.3), (4.7), (4.11) and (4.15) the Reynolds numbers depending on the mass flow rate are reported, collected respectively by unit cell size and by TPMS type. The configurations are identified by the initial of the name of the TPMS type and the value of the unit cell size (for example L15 will be $Lidinoid$ with unit cell of $15\,mm$).

In the following, the different configurations are compared in terms of pressure drop (or pressure gradient) and friction factor. The domain used for these evaluations has been restricted to a central region of $7\,cm$ length, to excluded any inlet or outlet effects. The two surfaces where the pressure has been taken are indicated by the black lines in figure (4.1) for the case of *Diamond* with unit cell of $20\,mm$.

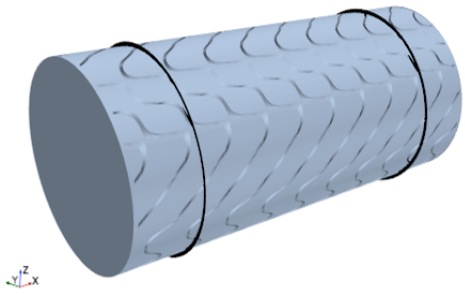

Figure 4.1: *Sections used to evaluate the pressure drop, for the case of Diamond with unit cell* $20\,mm$

The friction factor f can be computed knowing the pressure drop Δp since these two variables are related as in equation (4.2), where U is the fluid average velocity that is equal to $\dot{m}/(\rho A_s)$. Then, after substituting the cross section area A_s with V_{fluid}/L and inverting equation (4.2), it is possible to obtain the final formulation for f (4.3).

$$\Delta p = \frac{1}{2}\rho U^2 f \frac{L}{D_h} \tag{4.2}$$

$$f = \frac{2D_h}{\rho L U^2}\Delta p = 2\rho \frac{D_h}{L^3}\frac{V_{fluid}^2}{\dot{m}^2}\Delta p \tag{4.3}$$

4.1 Single TPMS structures

In this section the dimensional and dimensionless results of the four types of TPMS are exposed separately and finally they are compared to one another in section (4.1.5).

Figure (4.2) shows the Reynolds number depending on the mass flow rate for the different unit cell sizes: $10\,mm$ (4.2a), $15\,mm$ (4.2b) and $20\,mm$ (4.2c). For all the TPMS structures, the Reynolds number increases with increasing unit cell size, due to the reduction of the wetted surface area. *Gyroid* is the structure that produces the highest values of Reynolds number, followed by *Diamond*, then *SplitP* and *Lidinoid*. This order is coherent with the one obtained for the porosity, in figure (2.4a).

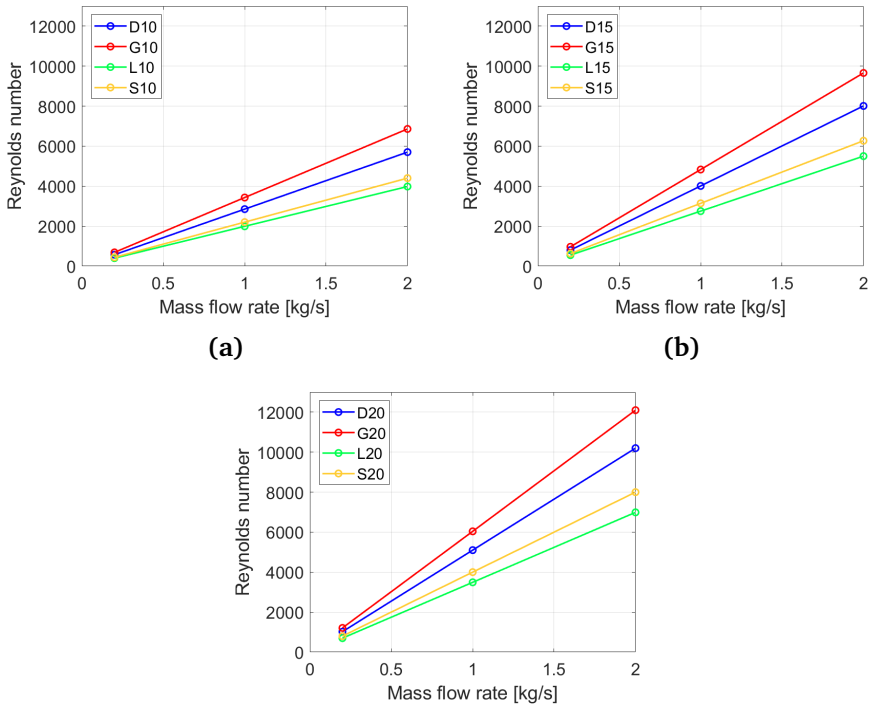

Figure 4.2: *Reynolds number depending on the mass flow rate for the three unit cell sizes,* $10\,mm$ *(a),* $15\,mm$ *(b) and* $20\,mm$ *(c)*

The Reynolds number values corresponding to the lowest mass flow rate are of the order of 10^2 and this would indicate laminar (or transitional) flow regime in a smooth tube. However the laminar-turbulent transition for TPMS has not been deeply studied yet and it is possible to expect the threshold to have a lower value.

The results proposed in the following have been obtained with the *Lag-EB* $k-\epsilon$ model.

4.1.1 Diamond

In figure (4.3) the Reynolds number for the *Diamond* is plotted against the mass flow rate for the three unit cell sizes. As predictable, unit cell size of $20\,mm$ produces the highest values of Re.

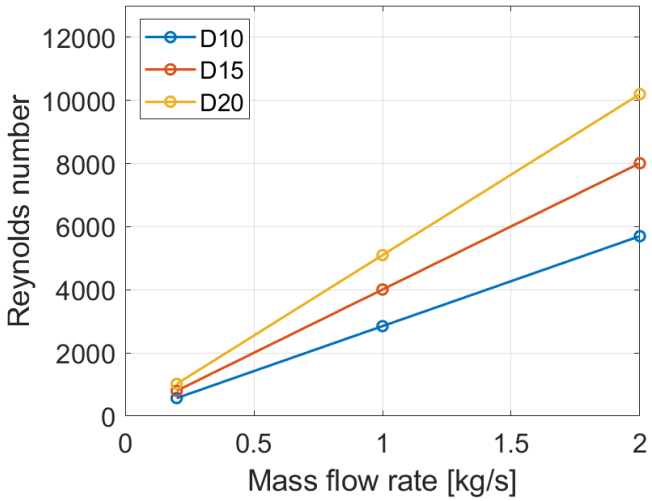

Figure 4.3: *Reynolds number depending on the mass flow rate for the three Diamond configurations*

The computed values of pressure drop are reported in table (4.1). They have been interpolated with a second order polynomial to produce the curves in figure (4.4a).

Table 4.1: *Diamond - Pressure drop $[kPa]$ depending on the mass flow rate $[kg/s]$*

	Unit cell size $[mm]$		
Mass flow rate $[kg/s]$	10	15	20
0.2	0.370 ± 0.003	0.184 ± 0.009	0.11 ± 0.01
1	7.26 ± 0.05	3.6 ± 0.2	2.2 ± 0.3
2	26.6 ± 0.2	13.1 ± 0.6	8 ± 1

The friction factor values are tabulated in table (4.2) for the three unit cell sizes depending on the associated Reynolds numbers. They are plotted together in figure (4.4b). The f values decrease with increasing Reynolds number and unit cell size.

Table 4.2: *Diamond - Friction factor depending on the Reynolds number*

Unit cell size $s\,[mm]$	Reynolds number	Friction factor
10	$0.570 \cdot 10^3$	4.94 ± 0.03
	$2.85 \cdot 10^3$	3.88 ± 0.03
	$5.70 \cdot 10^3$	3.55 ± 0.03
15	$0.801 \cdot 10^3$	4.6 ± 0.2
	$4.01 \cdot 10^3$	3.6 ± 0.2
	$8.01 \cdot 10^3$	3.3 ± 0.1
20	$1.02 \cdot 10^3$	4.0 ± 0.5
	$5.10 \cdot 10^3$	3.3 ± 0.4
	$10.2 \cdot 10^3$	2.9 ± 0.4

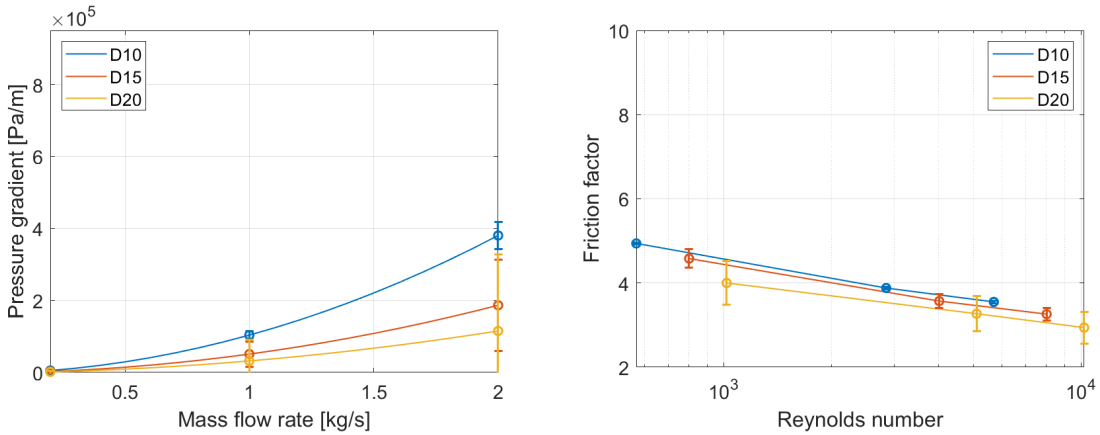

(a) **(b)**

Figure 4.4: *Pressure gradient curves (a) and friction factor (b) for the three Diamond structures*

Figure (4.5) shows the velocity field computed at mass flow rate of $1\,kg/s$ on a cross and a longitudinal sections for the three *Diamond* structures, also to highlight the internal shape of the lattices. The velocity magnitude depends on the section, but the structure with smaller unit cell size produces in general higher values of it. In figure (4.6) the streamlines are showed, again computed at $1\,kg/s$. Those have been produced starting from the center of the inlet cross section. The lattice with unit cell size of $20\,mm$ produces a noticeable lower dispersion of the streamlines with respect to the other two. They remain compact along the channel length, thus there is not a great mixing of the fluid.

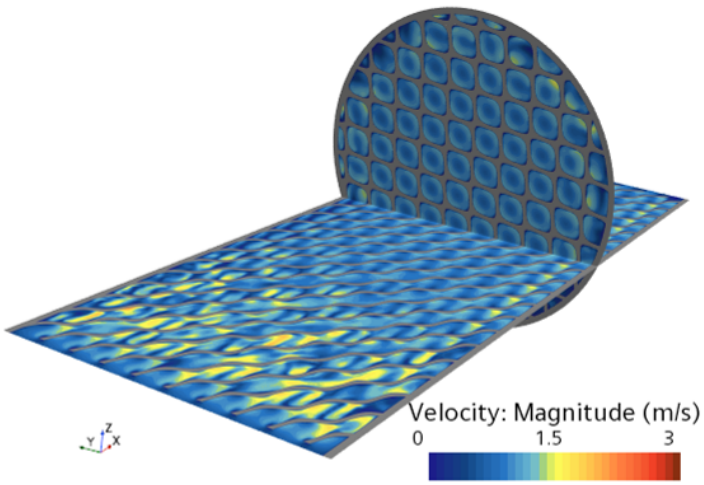

(a)

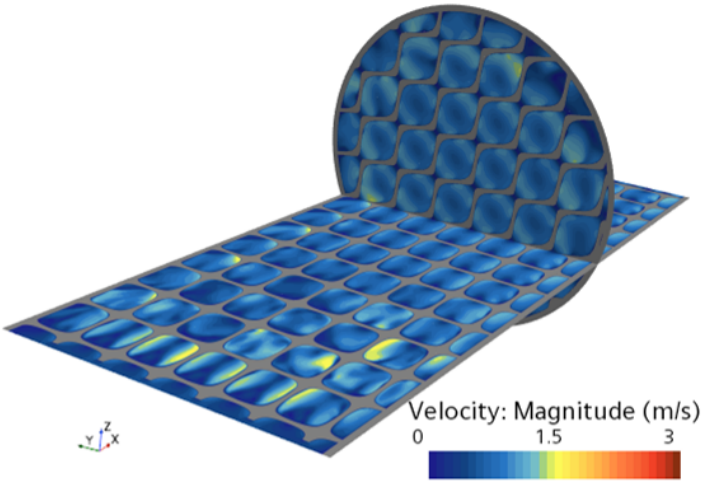

(b)

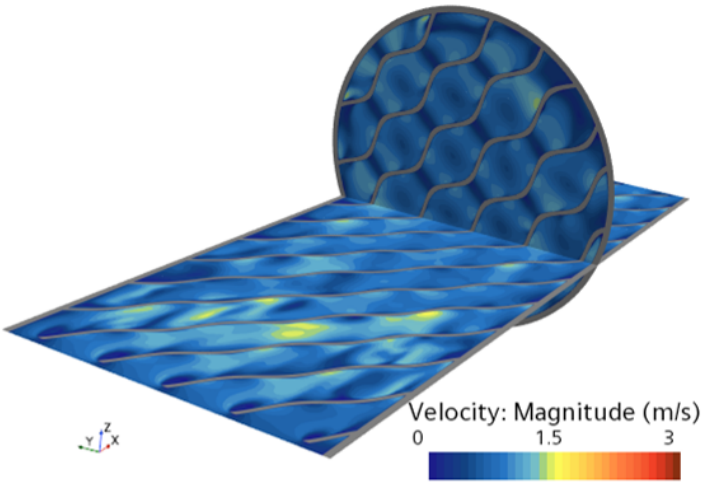

(c)

Figure 4.5: *Velocity field on cross and longitudinal sections of the three Diamond structures with unit cell size* $10\,mm$ *(a),* $15\,mm$ *(b) and* $20\,mm$ *(c)*

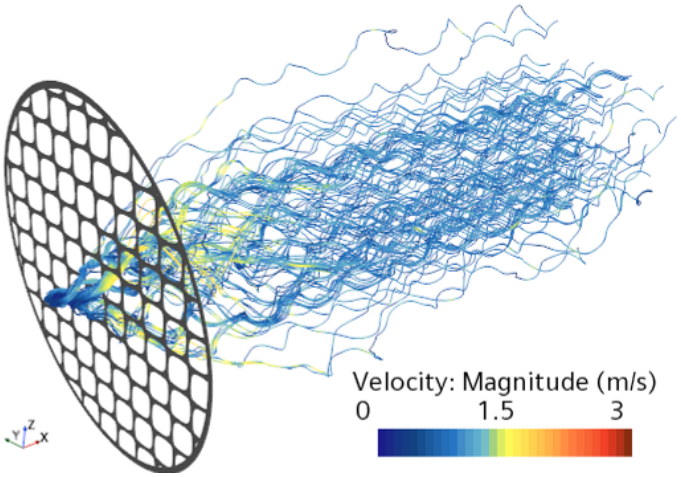

(a)

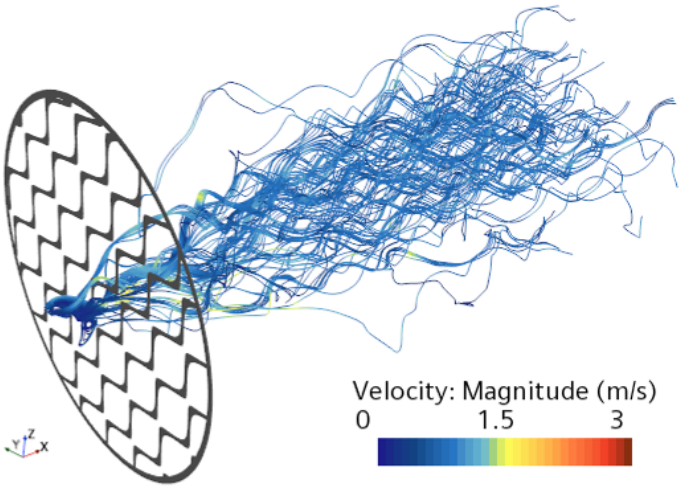

(b)

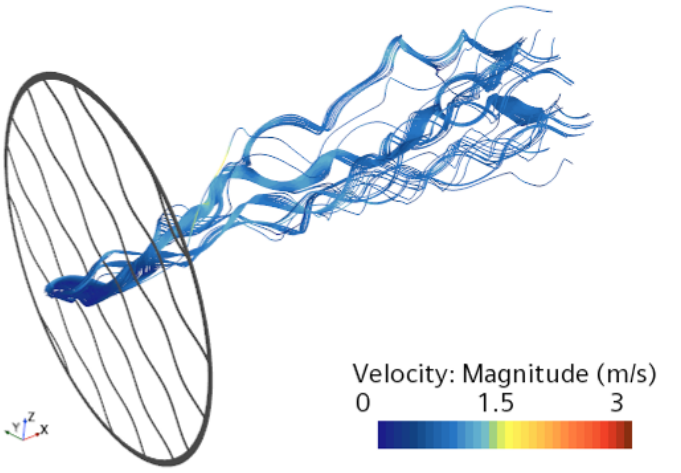

(c)

Figure 4.6: *Velocity field on the streamlines of the three Diamond structures with unit cell size* $10\,mm$ *(a),* $15\,mm$ *(b) and* $20\,mm$ *(c)*

4.1.2 Gyroid

The Reynolds number for the three *Gyroid* structures depending on the mass flow rate is plotted in figure (4.7).

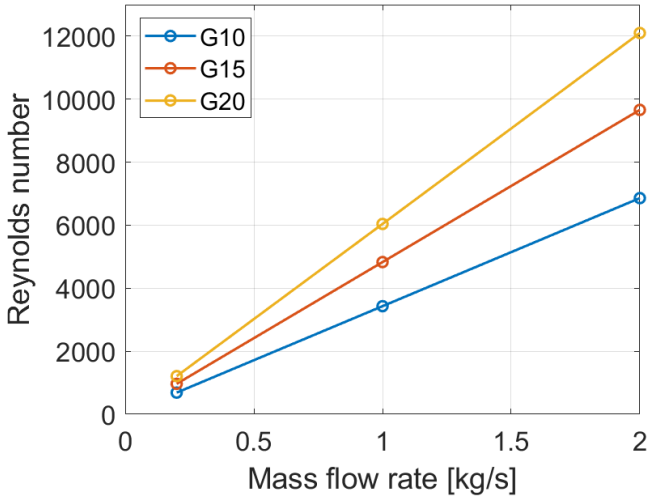

Figure 4.7: *Reynolds number depending on the mass flow rate for the three Gyroid configurations*

The computed pressure drop values are reported in table (4.3) and the curves of the pressure gradient, produced with an interpolation with a second order polynomial, are shown in figure (4.8a).

Table 4.3: *Gyroid - Pressure drop $[kPa]$ depending on the mass flow rate $[kg/s]$*

	Unit cell size $[mm]$		
Mass flow rate $[kg/s]$	10	15	20
0.2	0.283 ± 0.008	0.147 ± 0.004	0.092 ± 0.009
1	5.0 ± 0.1	2.72 ± 0.07	1.7 ± 0.2
2	18.3 ± 0.5	9.9 ± 0.2	6.3 ± 0.6

Table (4.4) reports the friction factor values depending on the Reynolds number for the three unit cell sizes. They are plotted in figure (4.8b). The f values produced by the *Gyroid* structures with unit cell size of $10\,mm$ and $15\,mm$ result to be comparable and slightly higher than the ones of the third structure.

Table 4.4: *Gyroid - Friction factor depending on the Reynolds number*

Unit cell size $s\,[mm]$	Reynolds number	Friction factor
10	$0.686 \cdot 10^3$	5.3 ± 0.2
	$3.43 \cdot 10^3$	3.7 ± 0.1
	$6.86 \cdot 10^3$	3.4 ± 0.1
15	$0.966 \cdot 10^3$	4.9 ± 0.1
	$4.83 \cdot 10^3$	3.59 ± 0.09
	$9.66 \cdot 10^3$	3.25 ± 0.08
20	$1.21 \cdot 10^3$	4.2 ± 0.4
	$6.04 \cdot 10^3$	3.2 ± 0.3
	$12.1 \cdot 10^3$	2.9 ± 0.3

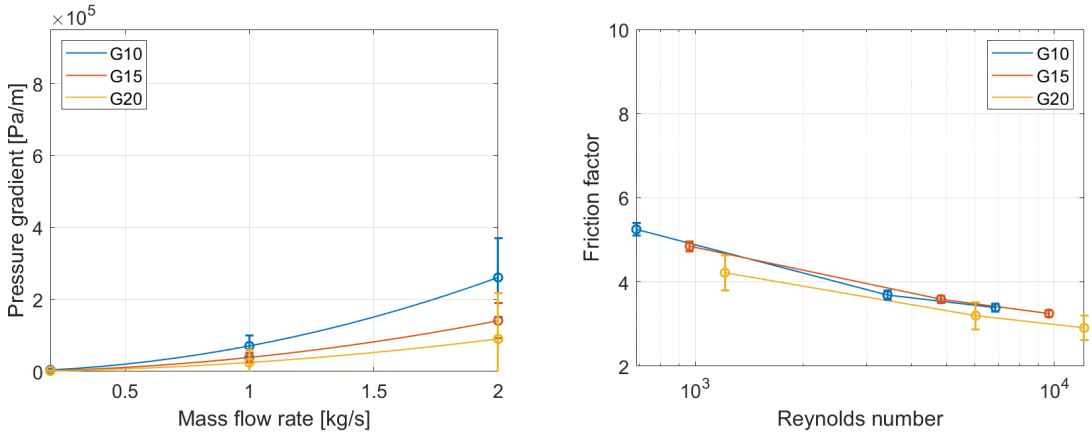

(a) **(b)**

Figure 4.8: *Pressure gradient curves (a) and friction factor (b) for the three Gyroid structures*

The velocity field at $1\,kg/s$ for the three *Gyroid* lattices on a cross and a longitudinal sections are presented in figure (4.9). The internal shape of the structure highlights the presence of some channels that go straight-forward from the inlet to the outlet, reducing the pressure drop, but also the mixing of the fluid.

Figure (4.10) shows the velocity plotted on some streamlines starting from the center of the inlet cross section. As for the *Diamond*, it is evident here the lower level of dispersion produced by the coarsest lattice with respect to the others.

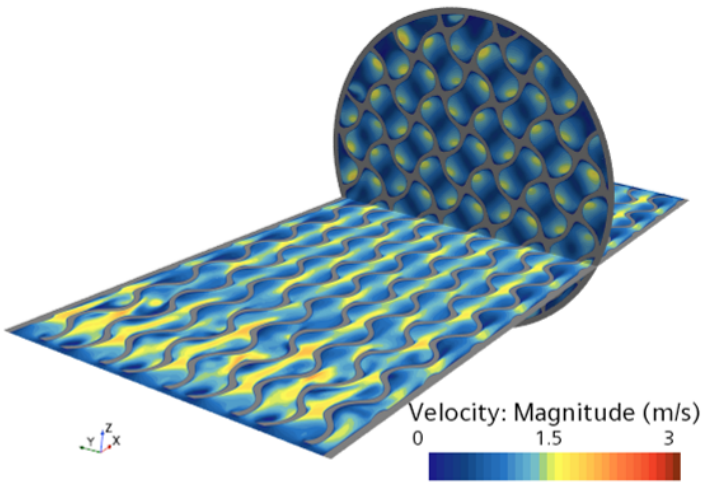

(a)

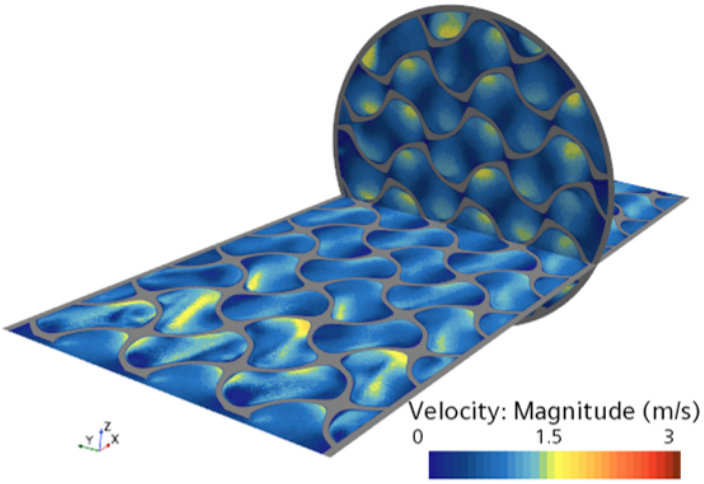

(b)

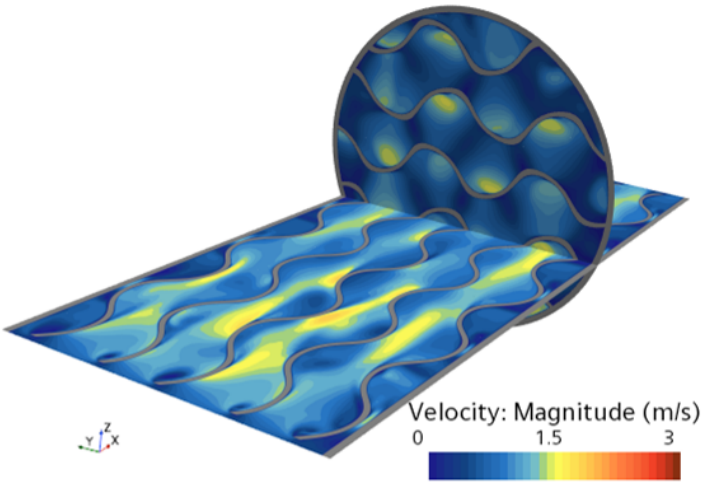

(c)

Figure 4.9: *Velocity field on cross and longitudinal sections of the three Gyroid structures with unit cell size* $10\,mm$ *(a),* $15\,mm$ *(b) and* $20\,mm$ *(c)*

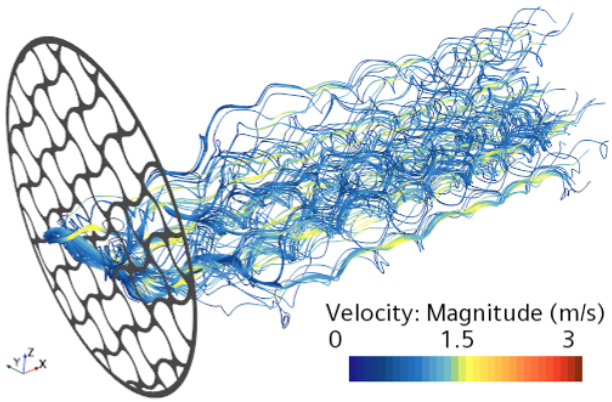

(a)

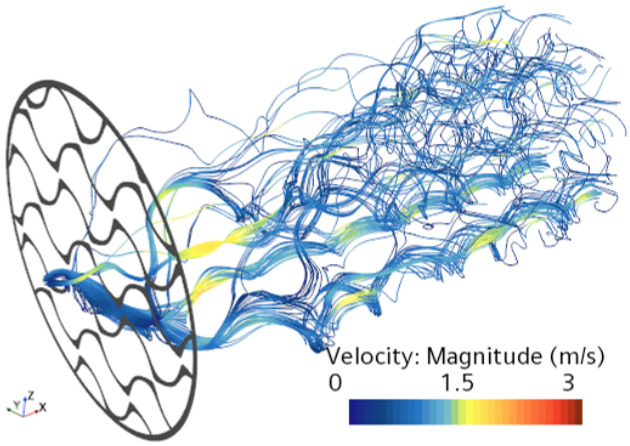

(b)

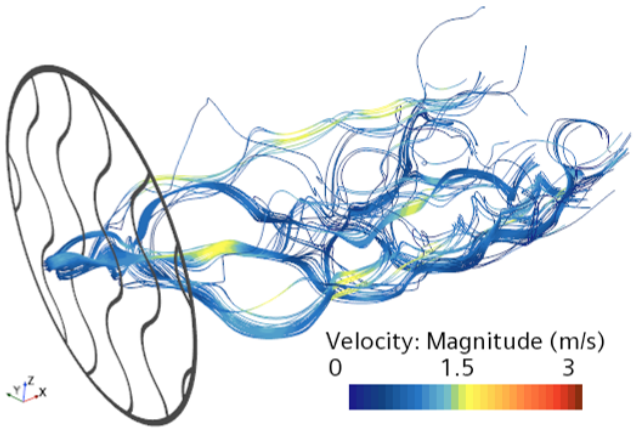

(c)

Figure 4.10: *Velocity field on the streamlines of the three Gyroid structures with unit cell size* $10\,mm$ *(a),* $15\,mm$ *(b) and* $20\,mm$ *(c)*

4.1.3 Lidinoid

Figure (4.11) presents the Reynolds number values for the three *Lidinoid* structures.

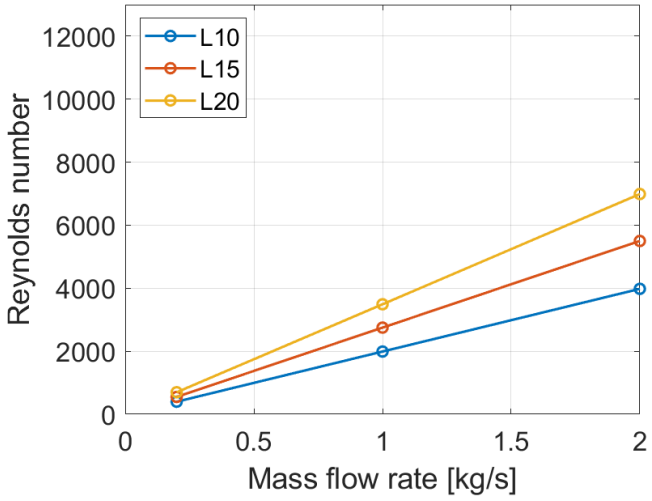

Figure 4.11: *Reynolds number depending on the mass flow rate for the three Lidinoid configurations*

In table (4.5) and figure (4.12a) are reported respectively the pressure drop values and pressure gradient curves. From those, the friction factor has been computed as in equation (4.3) and the values depending on the Reynolds number are collected in table (4.6) and in figure (4.12b).

Table 4.5: *Lidinoid - Pressure drop $[kPa]$ depending on the mass flow rate $[kg/s]$*

	Unit cell size $[mm]$		
Mass flow rate $[kg/s]$	10	15	20
0.2	0.77 ± 0.01	0.388 ± 0.007	0.25 ± 0.03
1	14.2 ± 0.3	7.0 ± 0.1	4.5 ± 0.5
2	51.1 ± 0.9	24.7 ± 0.5	16 ± 2

Table 4.6: *Lidinoid - Friction factor depending on the Reynolds number*

Unit cell size $s\,[mm]$	Reynolds number	Friction factor
10	$0.398 \cdot 10^3$	5.7 ± 0.1
	$1.99 \cdot 10^3$	4.25 ± 0.07
	$3.98 \cdot 10^3$	3.81 ± 0.07
15	$0.550 \cdot 10^3$	5.3 ± 0.1
	$2.75 \cdot 10^3$	3.83 ± 0.08
	$5.50 \cdot 10^3$	3.37 ± 0.07
20	$0.699 \cdot 10^3$	5.2 ± 0.6
	$3.49 \cdot 10^3$	3.7 ± 0.4
	$6.99 \cdot 10^3$	3.3 ± 0.4

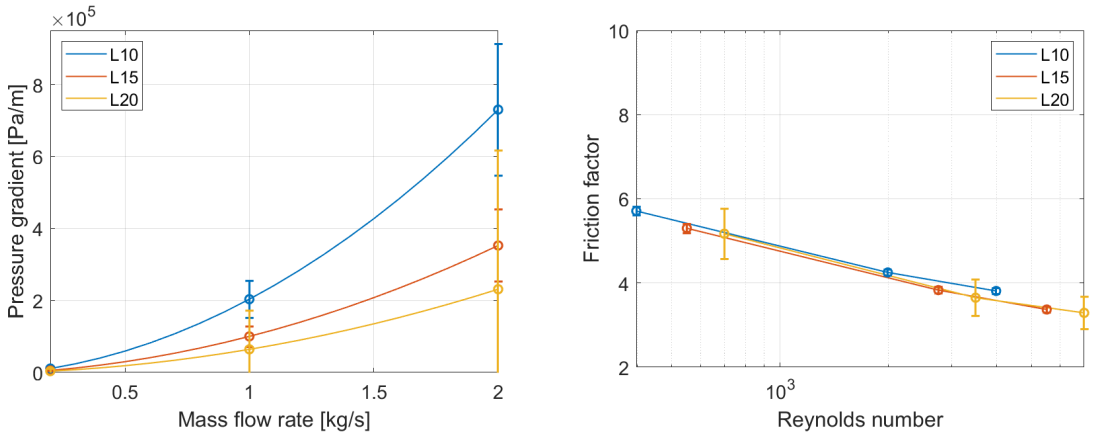

Figure 4.12: *Pressure gradient curves (a) and friction factor (b) for the three Lidinoid structures*

Figure (4.13) presents the velocity field computed at $1\,kg/s$ on two sections of the three *Lidinoid* structures. The velocity magnitude, that always depends on the cross section, is not substantially varying from one structure to the other. It is also clear from figure (4.13c) that, as occurs for the *Gyroid* structures, *Lidinoid* presents some inlet-outlet channels too.

The velocity plotted on the streamlines is shown in figure (4.14). On the contrary of what seen for the previous two TPMS structures, the dispersion level remains high even for the coarsest lattice, suggesting a good mixing.

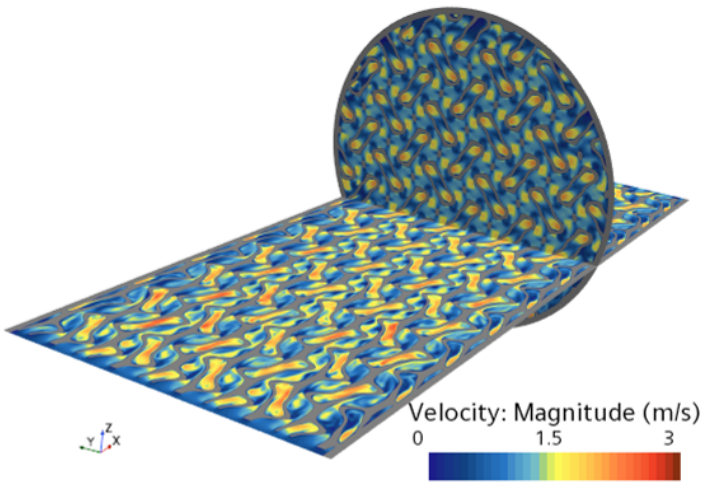

(a)

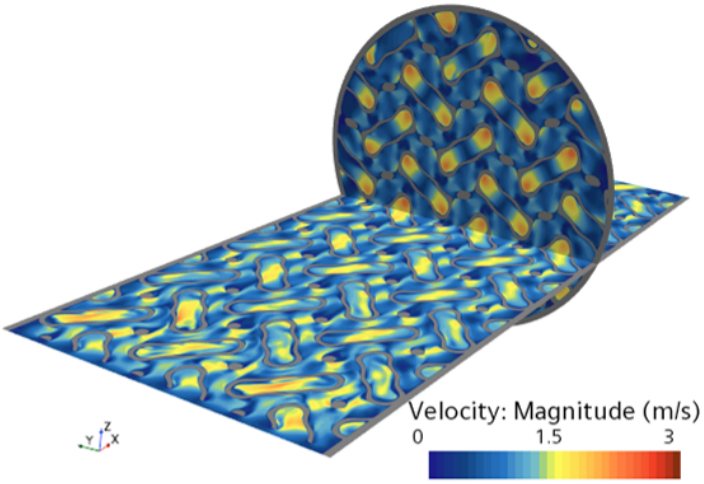

(b)

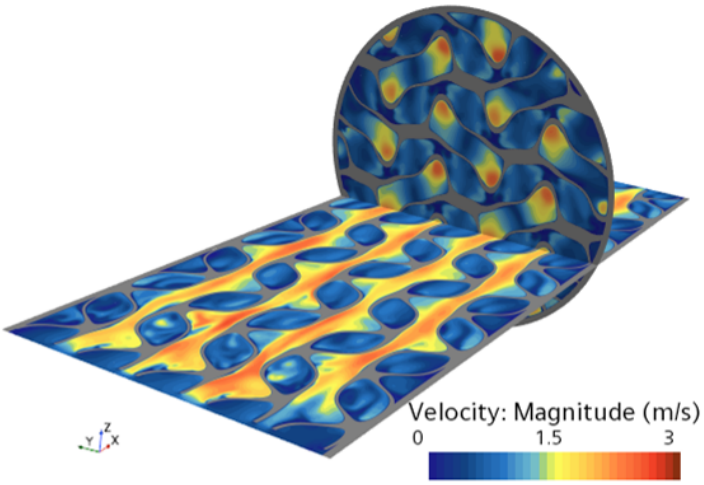

(c)

Figure 4.13: *Velocity field on cross and longitudinal sections of the three Lidinoid structures with unit cell size* $10\,mm$ *(a),* $15\,mm$ *(b) and* $20\,mm$ *(c)*

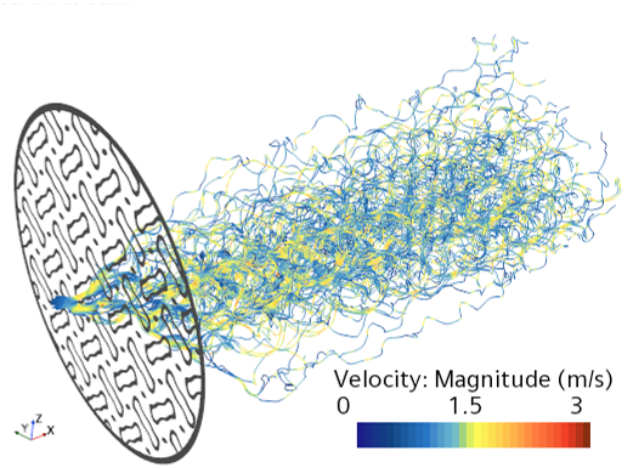

(a)

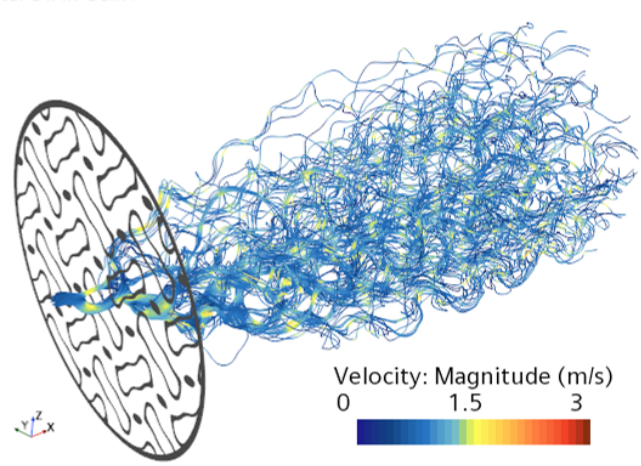

(b)

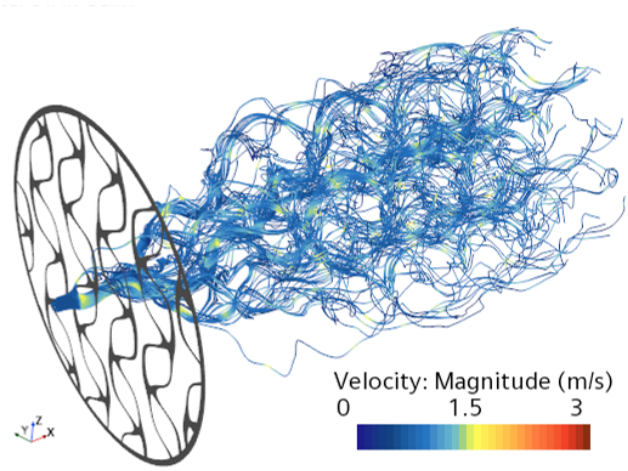

(c)

Figure 4.14: *Velocity field on the streamlines of the three Lidinoid structures with unit cell size* $10\,mm$ *(a),* $15\,mm$ *(b) and* $20\,mm$ *(c)*

4.1.4 SplitP

The Reynolds number values in the channels equipped with *SplitP* depending on the mass flow rate are shown in figure (4.15).

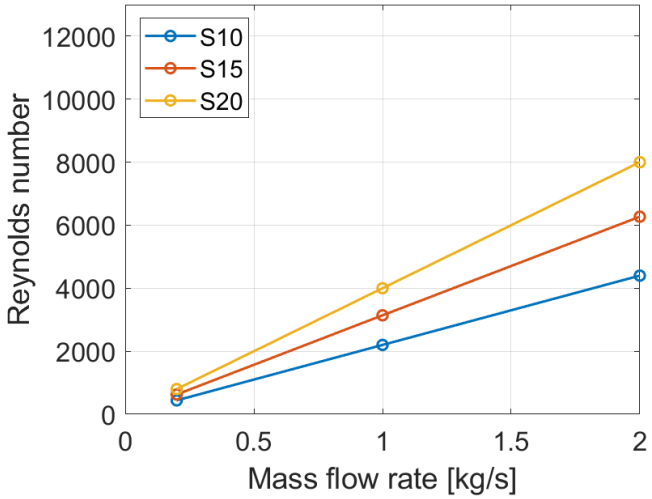

Figure 4.15: *Reynolds number depending on the mass flow rate for the three SplitP configurations*

The pressure drop values are presented in table (4.7) and interpolated with the curves shown in figure (4.16a).

Table 4.7: *SplitP - Pressure drop $[kPa]$ depending on the mass flow rate $[kg/s]$*

	Unit cell size $[mm]$		
Mass flow rate $[kg/s]$	10	15	20
0.2	1.06 ± 0.02	0.412 ± 0.007	0.37 ± 0.07
1	19.3 ± 0.4	8.36 ± 0.1	5 ± 1
2	65 ± 1	28.8 ± 0.5	16 ± 4

The computed friction factors are reported in table (4.8). They are shown all together in figure (4.16b), from which is visible that f decreases with increasing both Reynolds number and unit cell dimension.

Table 4.8: *SplitP - Friction factor depending on the Reynolds number*

Unit cell size $s\,[mm]$	Reynolds number	Friction factor
10	$0.440 \cdot 10^3$	9.7 ± 0.2
	$2.20 \cdot 10^3$	7.0 ± 0.1
	$4.40 \cdot 10^3$	5.9 ± 0.1
15	$0.627 \cdot 10^3$	7.5 ± 0.1
	$3.14 \cdot 10^3$	6.1 ± 0.1
	$6.27 \cdot 10^3$	5.28 ± 0.09
20	$0.800 \cdot 10^3$	7 ± 2
	$4.00 \cdot 10^3$	5 ± 1
	$8.00 \cdot 10^3$	4 ± 1

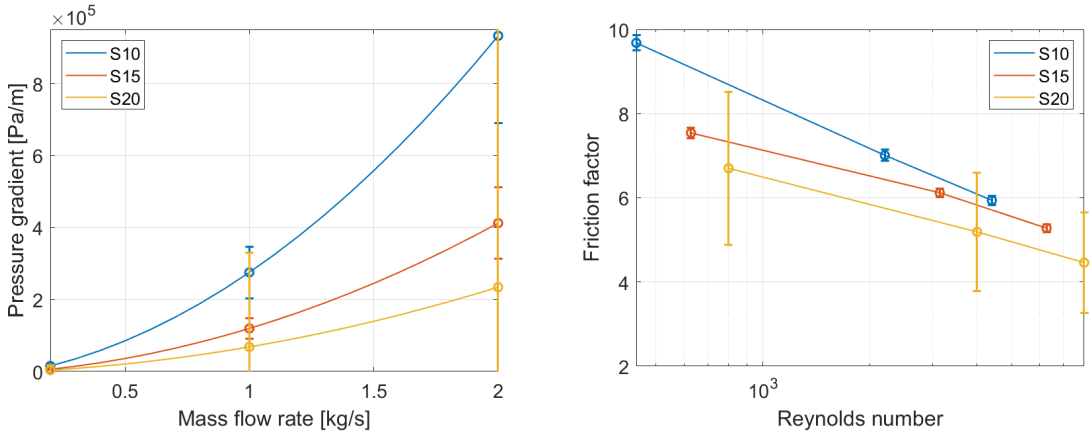

(a) **(b)**

Figure 4.16: *Pressure gradient curves (a) and friction factor (b) for the three SplitP structures*

In figure (4.17) the velocity field computed with a mass flow rate of $1\,kg/s$ is shown on a cross and a longitudinal sections for the three *SplitP* structures. The internal shape of the lattices is also evident. The velocity magnitude is higher for the structure with unit cell size of $10\,mm$, due to the reduction of the cross section area.

The streamlines deriving from the center of the inlet cross section are plotted in figure (4.18). The mixing of the flow is good, but the streamlines remain concentrated in the center of the channel and do not expand significantly in the radial direction.

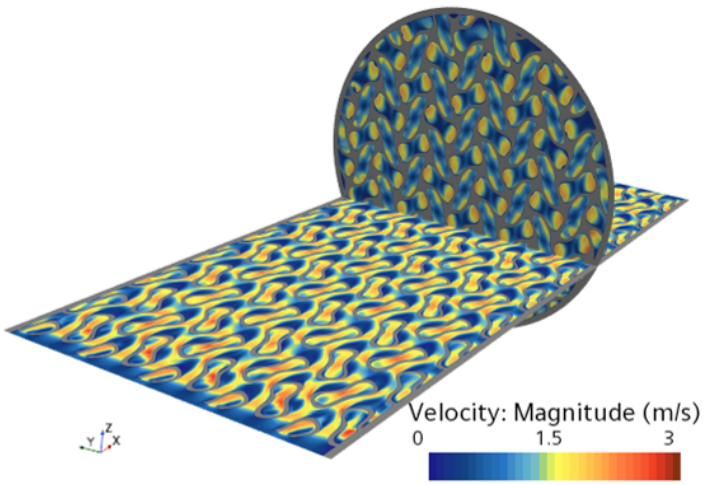

(a)

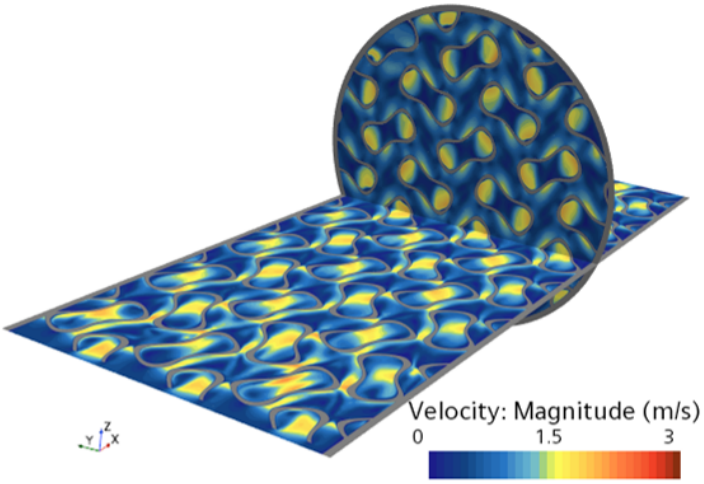

(b)

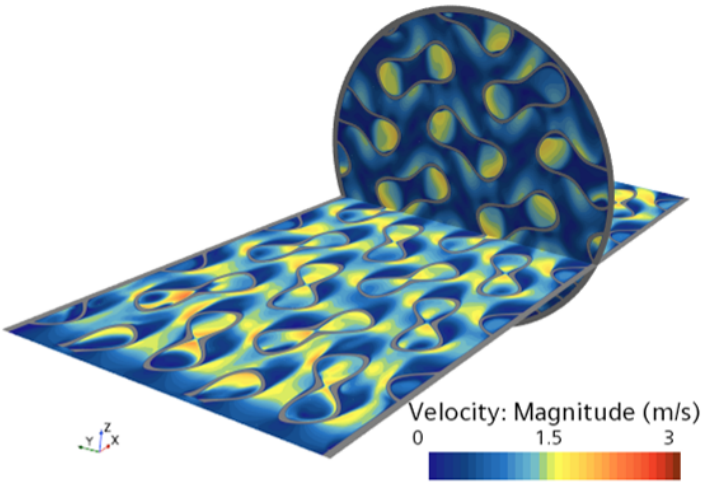

(c)

Figure 4.17: *Velocity field on cross and longitudinal sections of the three SplitP structures with unit cell size* $10\,mm$ *(a),* $15\,mm$ *(b) and* $20\,mm$ *(c)*

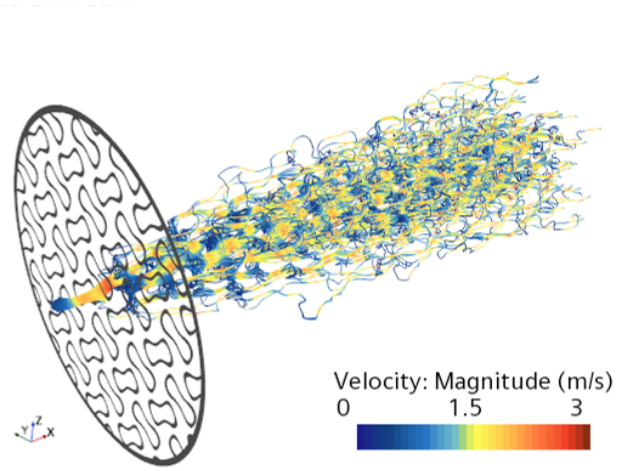

(a)

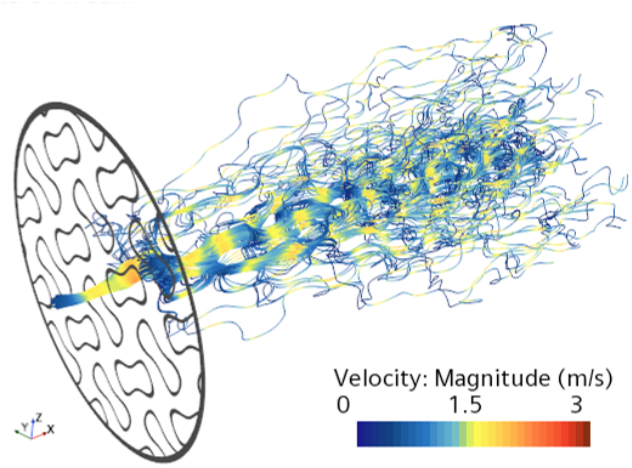

(b)

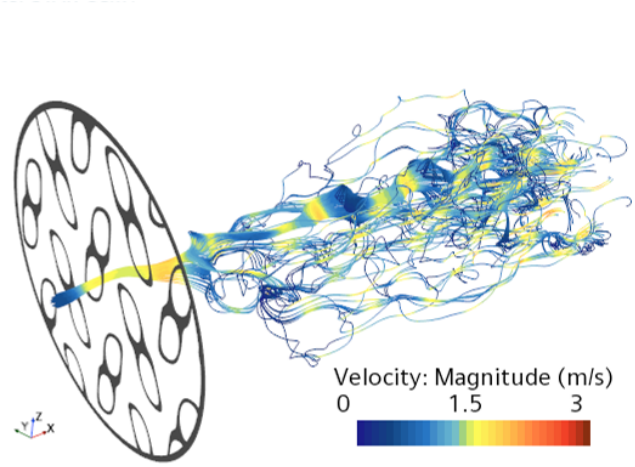

(c)

Figure 4.18: *Velocity field on the streamlines of the three SplitP structures with unit cell size* $10\,mm$ *(a),* $15\,mm$ *(b) and* $20\,mm$ *(c)*

4.1.5 Comparisons

This section is devoted to the comparison of the hydraulic performance of the four TPMS types. Figure (4.19) shows the pressure gradient curves of all the configurations collected by unit cell size.

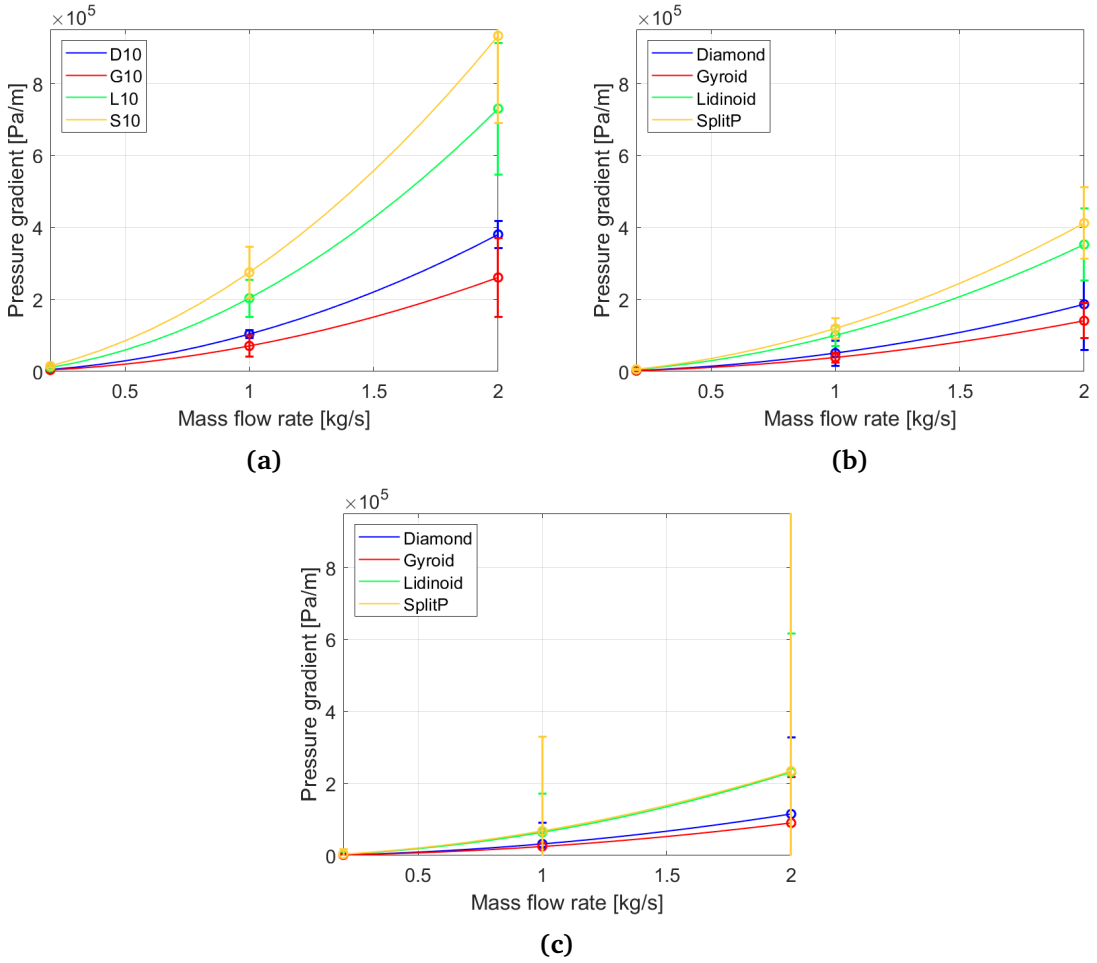

Figure 4.19: *Pressure gradient curves for all the TPMS types, with unit cell size* $10\,mm$ *(a),* $15\,mm$ *(b) and* $20\,mm$ *(c)*

The lowest curves are the one produced by the *Gyroid* structures, while the highest values correspond to the *SplitP* ones. *Diamond* curves behave similarly to the ones of *Gyroid* and *Lidinoid* to *SplitP*, coherently with the expectations discussed analyzing the geometrical characteristics of the four TPMS in section (2.1).

The friction factor values are plotted in figure (4.20) against the Reynolds number, that again is different for the four TPMS. *Diamond*, *Gyroid* and *Lidinoid* produce comparable values of f, even though the pressure gradient in the *Lidinoid* structure is significantly higher. This is due to the great impact of the geometrical characteristics of the structures (fluid volume and hydraulic diameter, discussed in section (2.1)) on the computation of the friction factor, from equation (4.3). *Diamond* and *Gyroid* structures have similar dimensions and produce comparable pressure drops, thus the friction factor values are also close. *Lidinoid* instead

produces a higher pressure drop, but the fluid volume and hydraulic diameter are reduced, that results in a relatively small friction factor. The opposite observation could be done for the *SplitP* lattice. As visible in figure (4.19), its pressure gradient curves are close to the ones of *Lidinoid*, but the resulting friction factor is clearly greater. In fact, the *SplitP* is characterized by higher values of fluid volume and hydraulic diameter with respect to the *Lidinoid*, that in principle means larger space for the fluid to flow, but the pressure drops in these two lattices are still comparable.

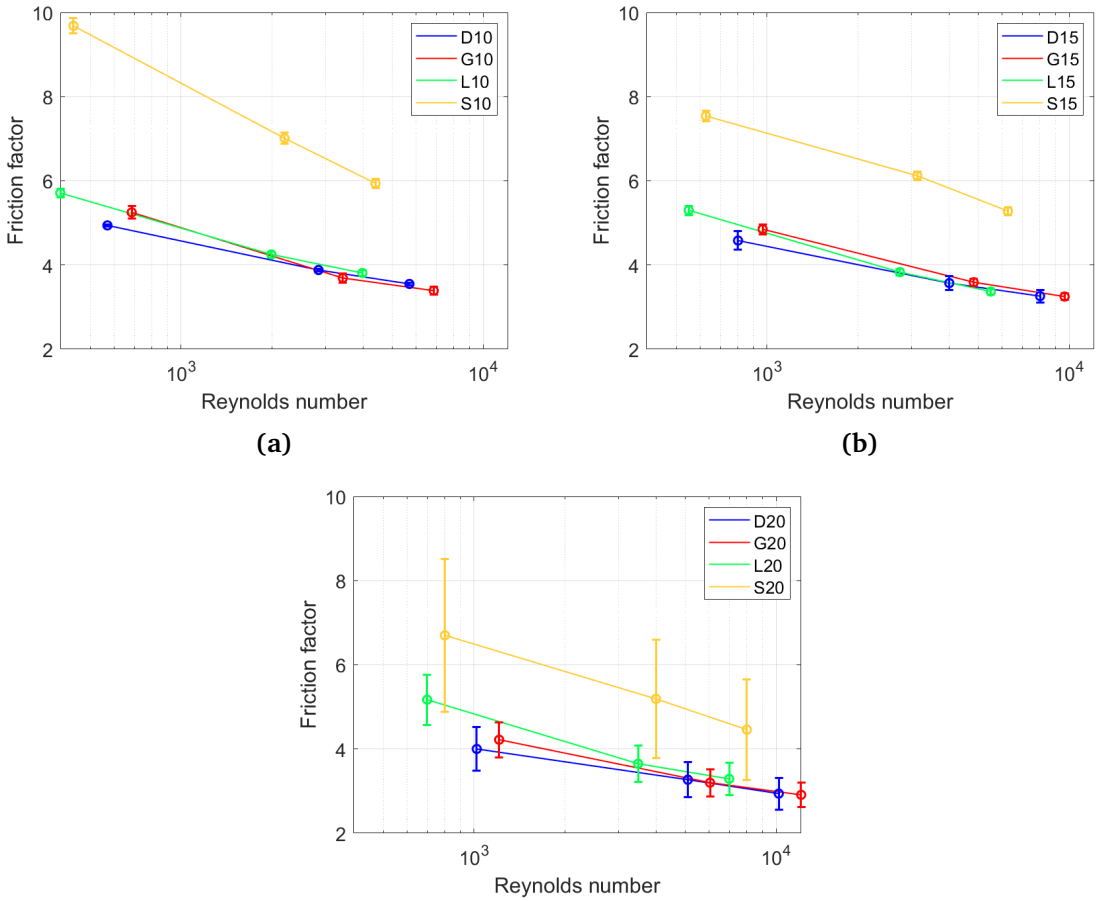

Figure 4.20: *Friction factor values for all the TPMS types, with unit cell size* $10\,mm$ *(a),* $15\,mm$ *(b) and* $20\,mm$ *(c)*

The error bars, estimated from the GCI study exposed in section (3.3.1), are much more visible for the case of unit cell size of $20\,mm$. In particular, The *SplitP* structure appears to be the one with the highest uncertainty, thus a more detailed mesh is probably needed for more accurate results.

4.2 TPMS combinations

The hydraulic performance of the channel equipped with TPMS combinations are here analyzed. In the following, each configuration is identified by the initials of the two structures that compose it, as already shown in table (2.3). The Reynolds number values are plotted against the mass flow rate in figure (4.21). This highlights that the Reynolds number depends much more on the TPMS type in the core region than on the one in the outer layer.

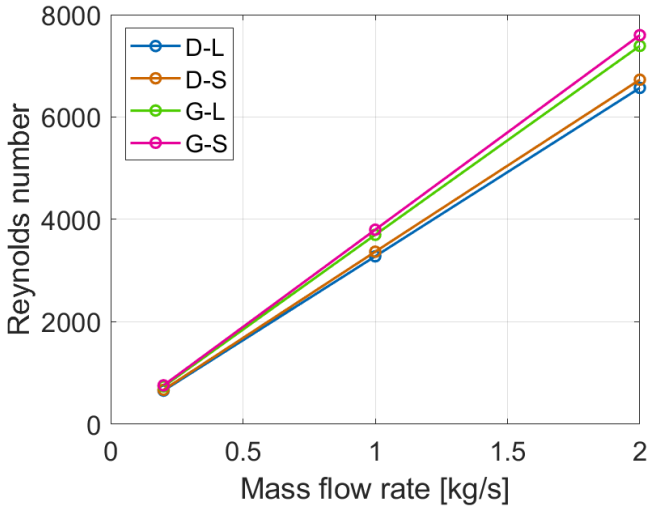

Figure 4.21: *Reynolds number depending on the mass flow rate for the TPMS combinations*

The pressure drop values are reported in table (4.9). The pressure gradient curves of the four combinations are shown in figure (4.23a).

Table 4.9: *TPMS combinations - Pressure drop $[kPa]$ depending on the mass flow rate $[kg/s]$*

	Combination name			
Mass flow rate $[kg/s]$	D-L	D-S	G-L	G-S
0.2	0.241	0.228	0.188	0.183
1	4.74	4.65	3.59	3.59
2	17.6	17.2	13.1	12.8

The four curves do not particularly differ one from the other. However, it is noticeable that they are coupled depending on the TPMS type inserted in their core. The two combinations containing *Diamond* produce pressure drops that are slightly larger with respect to the ones containing *Gyroid*, coherently with what previously obtained in section (4.1) for the single configurations. Thus, as expected, the pressure drop is driven by the core region TPMS.

In figure (4.22), the four combinations are compared to the single TPMS that compose them (for example, D-L is compared to *Diamond* and *Lidinoid*). It is visible that the pressure gradients of the combinations are closer to the ones produced by the core region structures (*Diamond* or *Gyroid*) than to the ones of the outer layer.

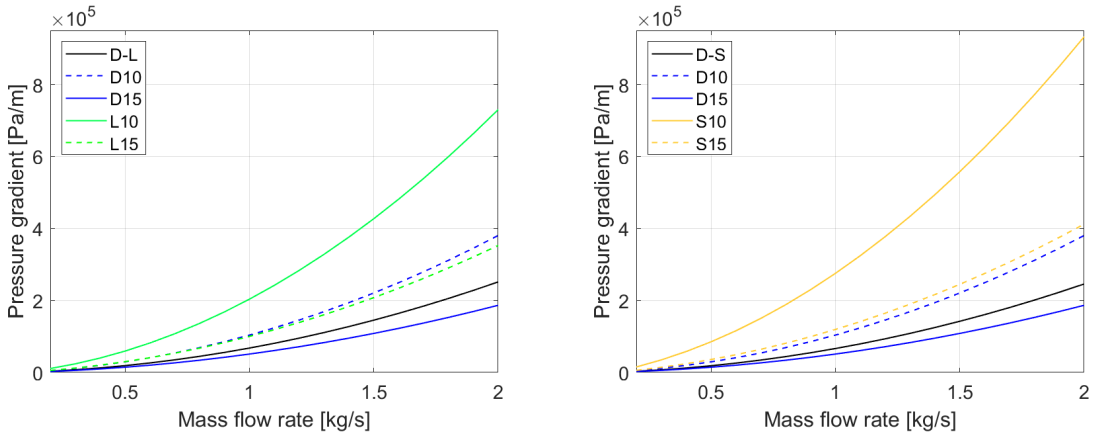

(a) *Diamond-Lidinoid*

(b) *Diamond-SplitP*

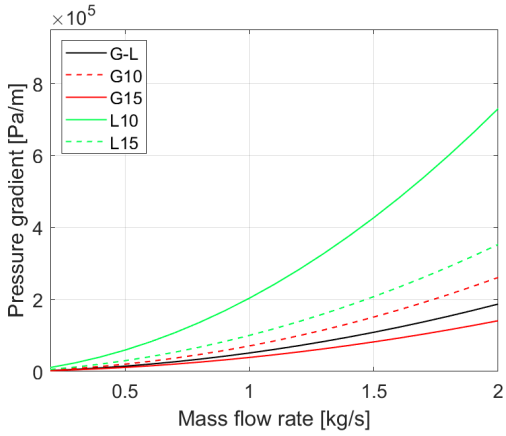

(c) *Gyroid-Lidinoid*

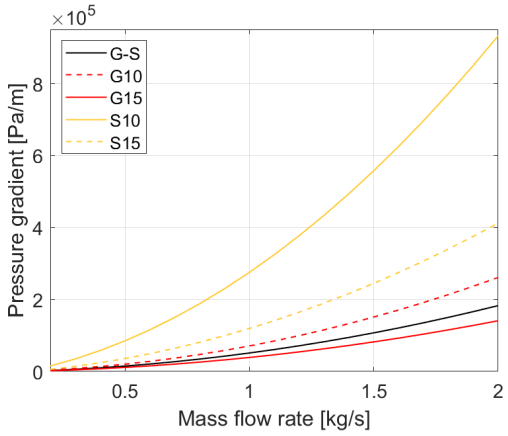

(d) *Gyroid-SplitP*

Figure 4.22: *Pressure gradient curves for the TPMS combinations, D-L (a), D-S (b), G-L (c) and G-S (d), compared to the ones of the single TPMS*

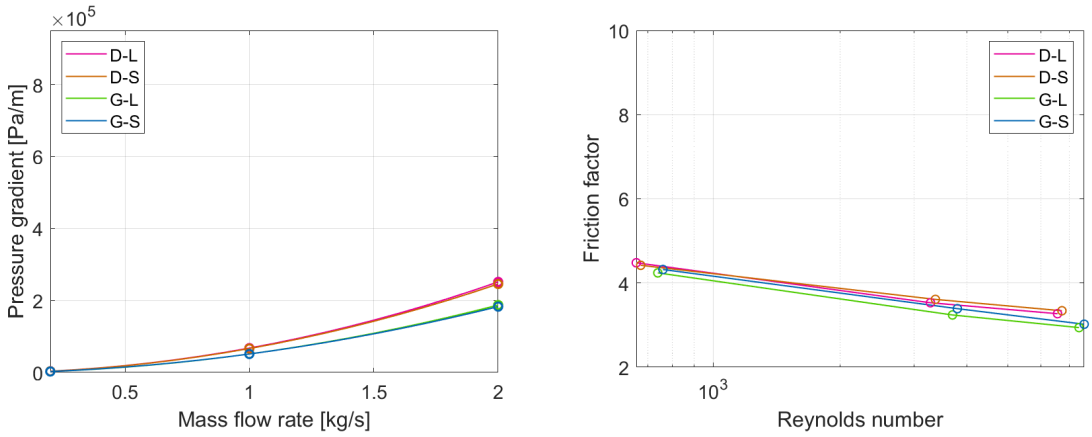

(a) **(b)**

Figure 4.23: *Pressure gradient curves (a) and friction factor (b) for the four TPMS combinations*

The friction factor values of each configuration, computed through equation (4.3) are reported in table (4.10) and plotted in figure (4.23b). The values are all comparable and the slight difference noticed in the pressure drop is visible also here, since the geometrical characteristics are similar. Thus, the combinations containing *Diamond* that produce larger pressure drop, also have higher friction factor.

Table 4.10: *Friction factor depending on the Reynolds number for the four TPMS combinations*

TPMS combination	Reynolds number	Friction factor
D-L	$0.657 \cdot 10^3$	4.48
	$3.28 \cdot 10^3$	3.53
	$6.57 \cdot 10^3$	3.27
D-S	$0.673 \cdot 10^3$	4.42
	$3.37 \cdot 10^3$	3.61
	$6.73 \cdot 10^3$	3.34
G-L	$0.739 \cdot 10^3$	4.24
	$3.70 \cdot 10^3$	3.24
	$7.39 \cdot 10^3$	2.94
G-S	$0.760 \cdot 10^3$	4.32
	$3.80 \cdot 10^3$	3.39
	$7.60 \cdot 10^3$	3.02

In figure (4.24), the friction factor resulting from the four combinations is compared to one of the single TPMS, as previously done for the dimensional variable (figure (4.22)). The friction factor of the TPMS combinations is always lower than the ones of the respective single TPMS. The motivation for that can be found in equation (4.3). The hydraulic diameter and the fluid volume have a relevant impact on f and these parameters are significantly reduced for the TPMS combinations with respect to their parent single lattices.

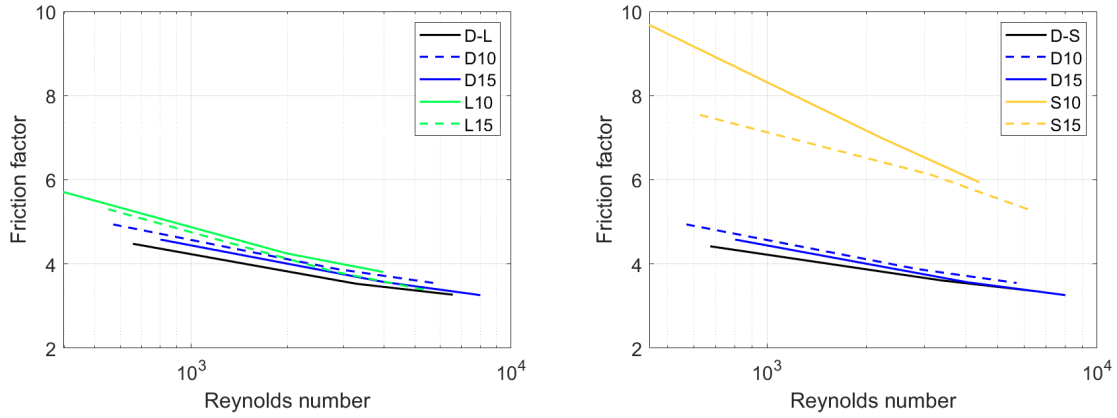

(a) *Diamond-Lidinoid* **(b)** *Diamond-SplitP*

(c) *Gyroid-Lidinoid* **(d)** *Gyroid-SplitP*

Figure 4.24: *Friction factor for the TPMS combinations, D-L (a), D-S (b), G-L (c) and G-S (d), compared to the ones of the single TPMS*

4.3 Comparison of three channel shapes

The dependence of the hydraulic variables on the channel shape has been investigated simulating three different pipes equipped with *Gyroid*.

The simulations have been performed again with the same three values of mass flow rate: $0.2\,kg/s$, $1\,kg/s$ and $2\,kg/s$. The corresponding values of Reynolds numbers, computed with equation (4.1), are shown in figures (4.25) and (4.26).

As visible in figure (4.26), the circular channel gives the highest values of Reynolds number, meaning that the wetted area is smaller in that configuration.

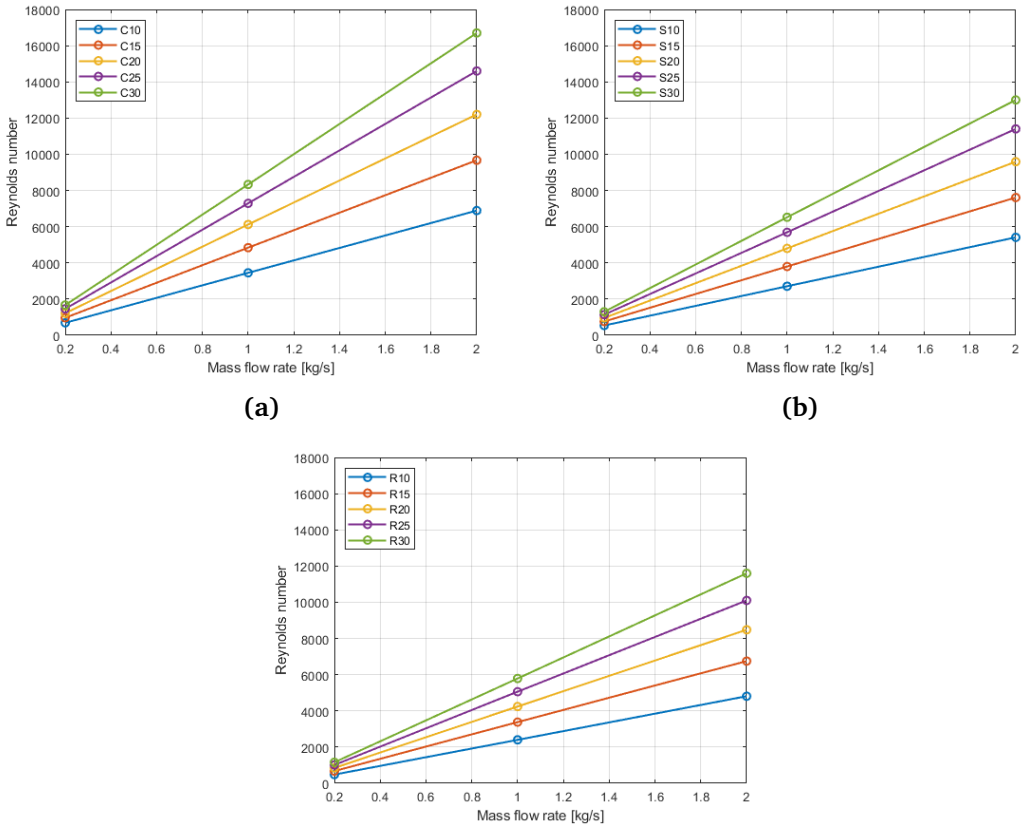

Figure 4.25: *Reynolds number depending on the mass flow rate for the circular (a), square (b) and rectangular (c) channels*

Figure (4.27) presents the curves of the pressure gradient for the three channels. For the largest and smallest unit cell size, the results of $Lag - EB\ k - \epsilon$ are compared to the ones of *SST* $k - \omega$ (dashed line), that has produced higher values.

Of the three channels, the circular one has the largest pressure gradient for the same mass flow rate, coherently with its higher values of Reynolds number.

Figure (4.28) collects the friction factor values of all the simulations, organized according to the *Gyroid* unit cell size. The circular markers refer to T1 while the triangular ones to T2.

The second turbulence model tends to produce higher values of friction factor with respect to the other one. Moreover, it is interesting to note that, in general, the square channel (red

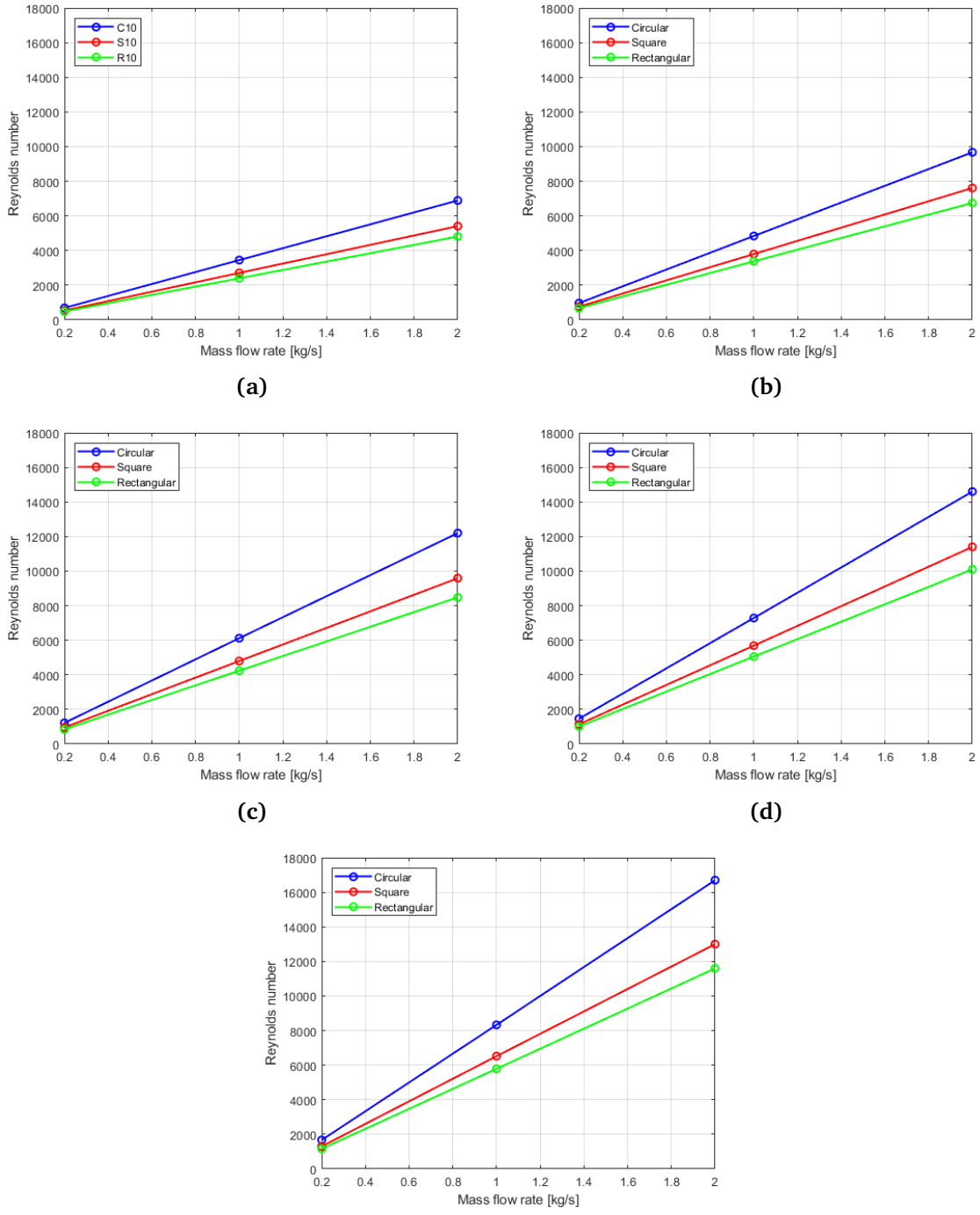

Figure 4.26: *Reynolds number depending on the mass flow rate for the five unit cell values,* $10\,mm$ *(a),* $15\,mm$ *(b),* $20\,mm$ *(c),* $25\,mm$ *(d), and* $30\,mm$ *(e)*

markers in the figures) shows higher values with respect to the other two. The uncertainties related to the channels equipped with the Gyroid with bigger unit cells are very large and most of the results fall in the same interval. In particular, the error bars of the results produced

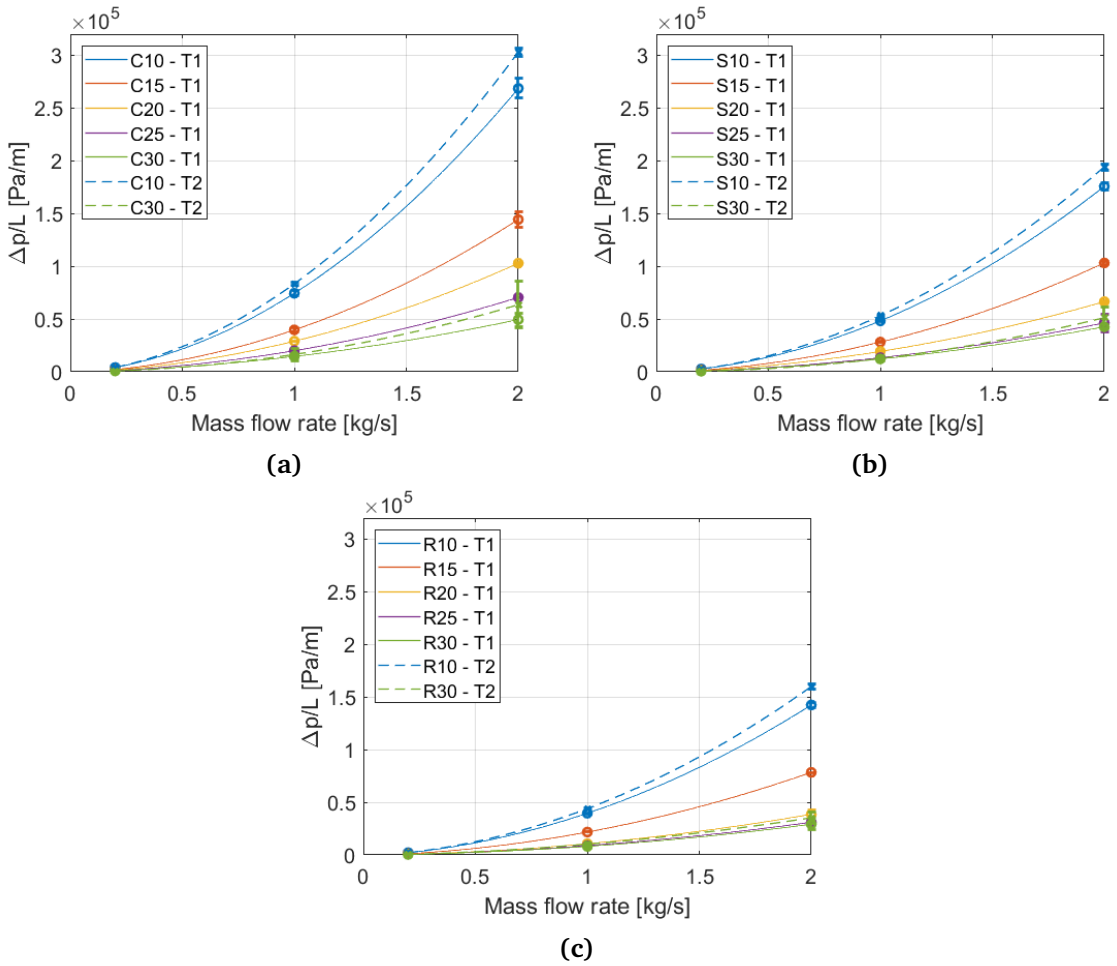

Figure 4.27: *Pressure gradient depending on the mass flow rate for the circular (a), square (b) and rectangular (c) channels*

with *SST* $k-\omega$ are more relevant than the ones related to *Lag-EB* $k-\epsilon$. However, in many cases, the difference between the two turbulence models is still evident.

Looking at the plots from the last one (4.28e) to the first (4.28a), it can be noticed that the results of the three channels get closer as the unit cell size decreases, independently on the turbulence model. Thus, as the TPMS gets denser, the shape of the channel becomes less relevant and the hydraulic performance is less sensitive to the way in which the channels volumes "cut" the TPMS. In other words, with unit cell sizes sufficiently low with respect to the hydraulic diameter, below a unit-cell-dimension-to-hydraulic-diameter ratio of around $1/3$ (unit cell size $15\,mm$), the effect of the shape of the cross section is nullified by the TPMS presence.

Larger unit cell sizes result in macroscopic structures, as the maximum one ($30\,mm$), since in 7 cm of length only two cells and a half are contained. On the contrary, a smaller unit cell dimension results in a greater number of unit cells and a more uniform porous structure.

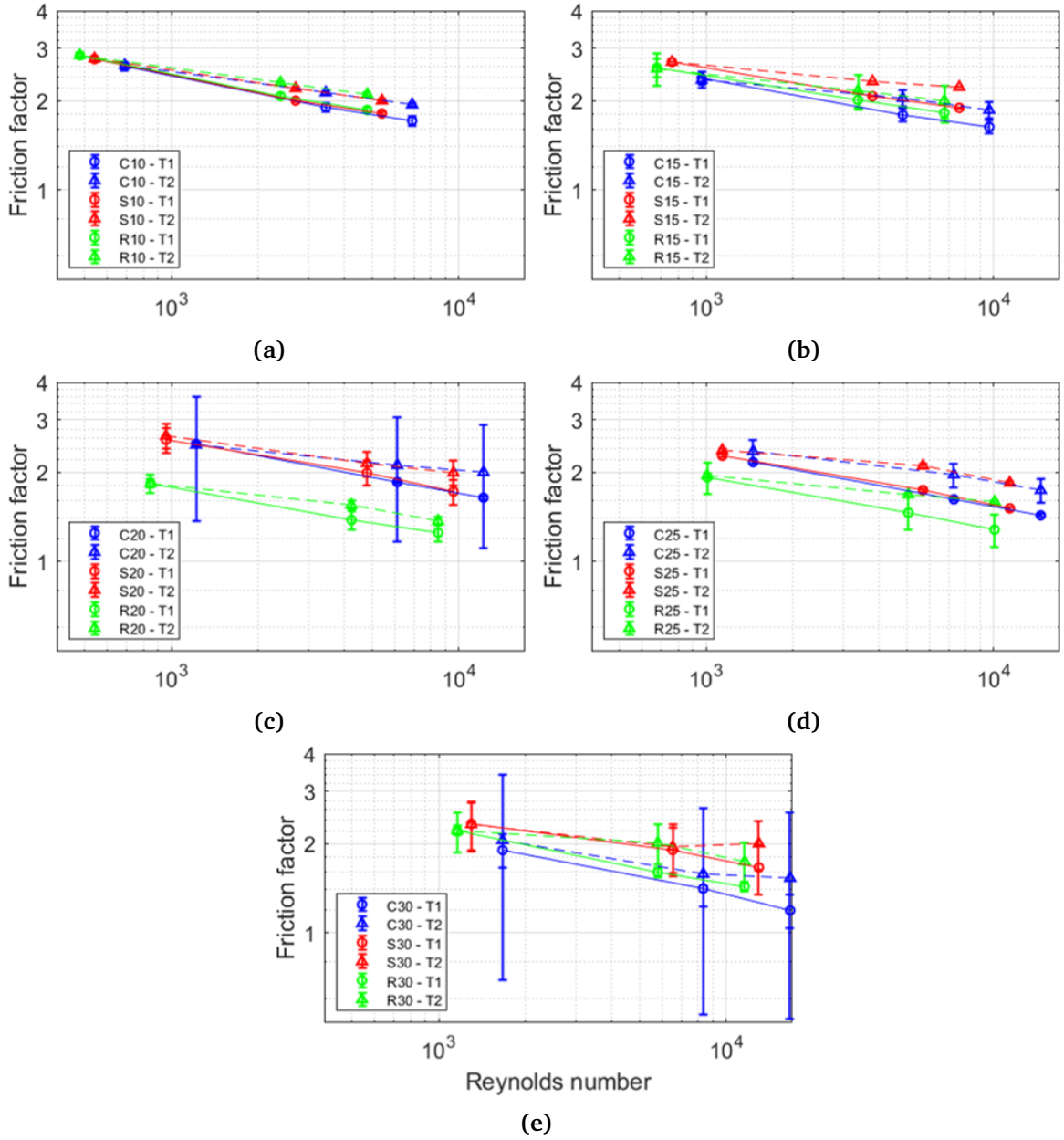

Figure 4.28: *Friction factor for the five unit cell sizes,* $10\,mm$ *(a),* $15\,mm$ *(b),* $20\,mm$ *(c),* $25\,mm$ *(d), and* $30\,mm$ *(e)*

Chapter 5

Thermal results

Energy simulations have been performed applying a uniform heat flux of $1\,MW/m^2$ on the external wall, excluding $1\,mm$ at the inlet and at the outlet.

The water inlet temperature has been set to $300\,K$ and the external wall maximum and average temperature increases with respect to it have been estimated for each configuration.

The average value of the dimensionless parameter Nu (Nusselt number) has also been estimated as in equation (5.1), where HTC is the average heat transfer coefficient, D_h is the hydraulic diameter and k_f is the fluid thermal conductivity.

$$\overline{Nu} = \frac{HTC \cdot D_h}{k_f} \tag{5.1}$$

The heat transfer coefficient is computed as in equation (5.2), where Q_{tot} is the total power deposited on the channel surface, A_{wall} is the interface area between solid and fluid, T_{wall} and T_{bulk} are the average temperatures respectively of the wall and of the water. The bulk temperature of the water has been obtained as the mean value of the mass flow averaged inlet and outlet temperatures.

$$HTC = \frac{Q_{tot}}{A_{wall} \cdot (T_{wall} - T_{bulk})} \tag{5.2}$$

5.1 Single TPMS structures

The thermal variables computed with the simulations on the single TPMS are exposed in this section. The four TPMS types are compared to each other in section (5.1.5). The results are presented with an error bar on the temperature, assuming that all the configurations would produce an uncertainty similar to the one estimated for the cases of $s = 15\,mm$ in section (3.3.1). Since the GCI study is not complete, the error has not been propagated to the other thermal variables (such as HTC and Nusselt number).

5.1.1 Diamond

The maximum and average temperature increase with respect to the water inlet temperature ($300\,K$) on the channel external wall are reported respectively in table (5.1) for the *Diamond* cases. They are graphically shown also in figure (5.1). It is interesting to notice that the difference between the maximum and average temperature decreases with decreasing unit cell dimension, indicating that the temperature distribution is getting more uniform.

Table 5.1: *Diamond - External wall maximum and average temperature increases and fluid maximum temperature increase with respect to inlet temperature* $[K]$ *depending on the mass flow rate* $[kg/s]$

$s\,[mm]$	$\dot{m}\,[kg/s]$	$\Delta T_{solid,MAX}\,[K]$	$\Delta T_{solid,AVG}\,[K]$	$\Delta T_{fluid,MAX}\,[K]$
10	0.2	95.3	70.0	93.8
	1	37.6	32.2	35.9
	2	27.9	22.7	26.5
15	0.2	120	96.9	119
	1	55.6	41.5	54.1
	2	42.4	28.8	40.8
20	0.2	147	122	146
	1	69.5	51.1	67.9
	2	53.6	34.9	52.1

The values of the maximum temperature increase in the water are also shown in table (5.1). Being the water saturation temperature around $407\,K$ at $3\,bar$ (imposed as outlet pressure), the maximum allowable temperature increase should be of approximately $110\,K$ to assure that the flow is single-phase. This threshold is not respected in the cases of unit cell sizes of $15\,mm$ and $20\,mm$ and the lowest mass flow rate. Thus, it would be necessary to work at higher pressure values for those configurations.

The heat transfer coefficient and Nusselt number for each configuration are exposed in table (5.2). The heat transfer coefficient is higher for smaller TPMS unit cells, while the Nusselt number behaves oppositely. This is due to the great influence of the geometrical characteristics (hydraulic diameter) on this dimensionless parameter.

Figure (5.2) shows the temperature field on the external wall of the channel computed at $1\,kg/s$. This highlights the beneficial effect of the TPMS with lower unit cell dimension.

Table 5.2: *Diamond - Heat transfer coefficient and Nusselt number depending on the Reynolds number*

$s\,[mm]$	Reynolds number	HTC $[W/(m^2K)]$	Nusselt number
10	$0.570 \cdot 10^3$	$6.51 \cdot 10^3$	41.1
	$2.85 \cdot 10^3$	$17.8 \cdot 10^3$	113
	$5.70 \cdot 10^3$	$29.1 \cdot 10^3$	184
15	$0.801 \cdot 10^3$	$5.02 \cdot 10^3$	49.1
	$4.01 \cdot 10^3$	$14.8 \cdot 10^3$	145
	$8.01 \cdot 10^3$	$24.0 \cdot 10^3$	235
20	$1.02 \cdot 10^3$	$4.38 \cdot 10^3$	57.0
	$5.10 \cdot 10^3$	$13.1 \cdot 10^3$	170
	$10.2 \cdot 10^3$	$21.3 \cdot 10^3$	277

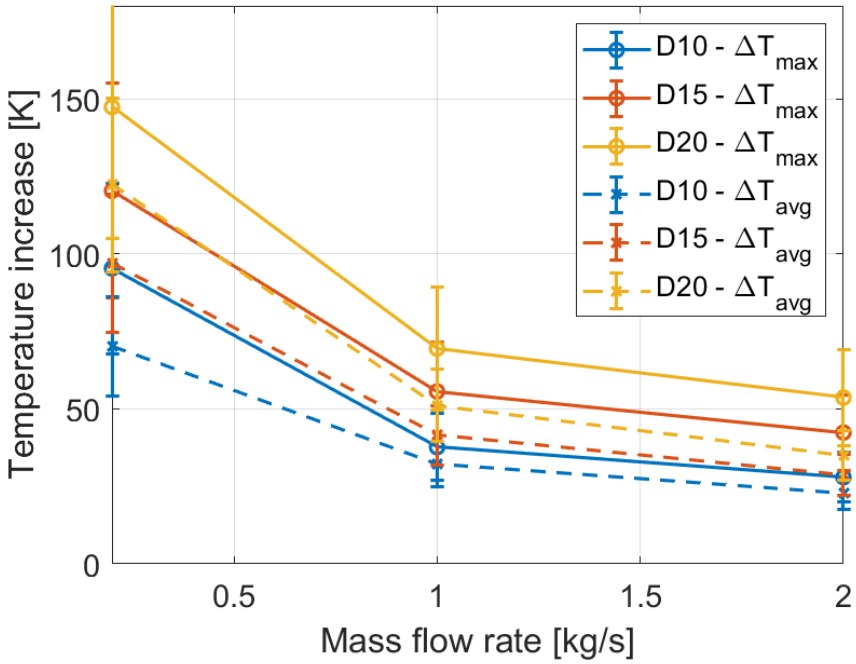

Figure 5.1: *Maximum and average temperature increase on the channel external wall for the Diamond structures depending on the mass flow rate*

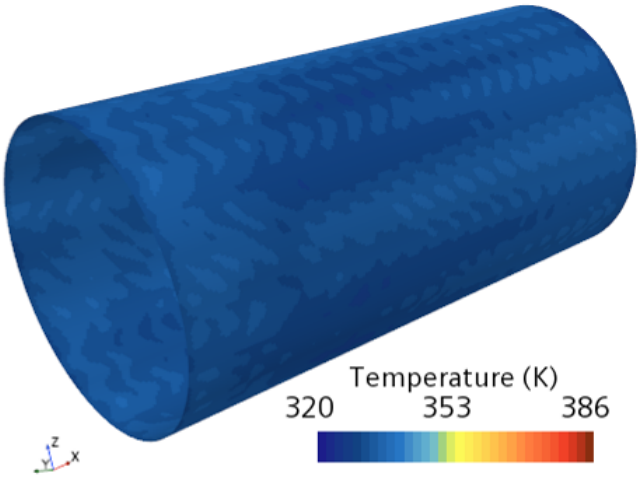

(a)

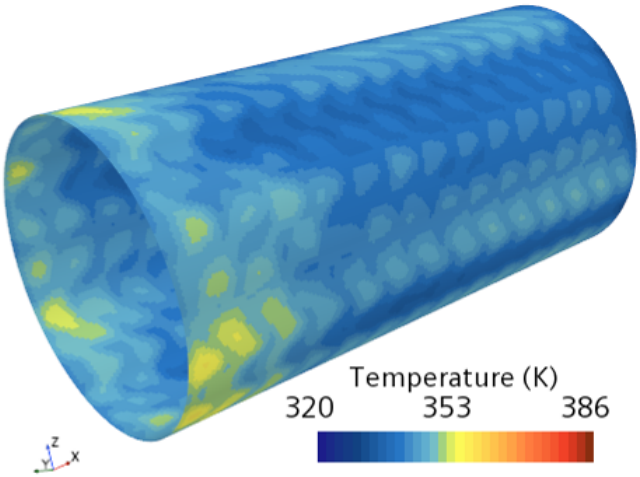

(b)

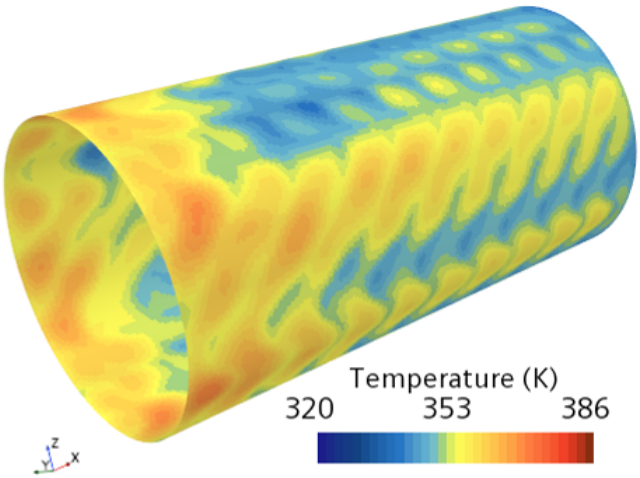

(c)

Figure 5.2: *Temperature field on the external wall for the three Diamond structures with unit cell size of* $10\,mm$ *(a),* $15\,mm$ *(b) and* $20\,mm$ *(c)*

5.1.2 Gyroid

The maximum and average temperature increase with respect to the water inlet temperature on the external wall of the channel equipped with *Gyroid* structures are collected in table (5.3) and plotted in figure (5.3). The difference between the values produced by the three lattices is relevant. Moreover, the gap between the maximum and the average temperature diminishes as the unit cell dimension reduces.

Table 5.3: *Gyroid - External wall maximum and average temperature increases and fluid maximum temperature increase with respect to inlet temperature* $[K]$ *depending on the mass flow rate* $[kg/s]$

$s\,[mm]$	$\dot{m}\,[kg/s]$	$\Delta T_{solid,MAX}\,[K]$	$\Delta T_{solid,AVG}\,[K]$	$\Delta T_{fluid,MAX}\,[K]$
10	0.2	99.6	83.5	98.1
	1	44.9	38.1	43.4
	2	33.9	26.7	32.4
15	0.2	151	132	150
	1	62.2	49.0	60.4
	2	48.8	34.1	46.2
20	0.2	173	142	172
	1	85.3	59.7	83.7
	2	66.0	40.0	64.3

The fluid maximum temperature increase with respect to the inlet one is exposed in table (5.3) too. Also in the *Gyroid* case, the saturation temperature (around $407\,K$) is overcome by the two configurations with unit cell sizes of $15\,mm$ and $20\,mm$ at the lowest mass flow rate, indicating that the flow is not completely single-phase. This is however limited to small portions of the fluid domain next to the wall.

The heat transfer coefficient and Nusselt number depending on the Reynolds number are collected in tables (5.4). The first decreases with increasing the unit cell dimension, while the second, computed as in equation (5.1) has the opposite trend, due to the influence of the hydraulic diameter.

Table 5.4: *Gyroid - Heat transfer coefficient and Nusselt number depending on the Reynolds number*

$s\,[mm]$	Reynolds number	HTC $[W/(m^2K)]$	Nusselt number
10	$0.686 \cdot 10^3$	$5.61 \cdot 10^3$	44.7
	$3.43 \cdot 10^3$	$15.8 \cdot 10^3$	126
	$6.86 \cdot 10^3$	$25.4 \cdot 10^3$	203
15	$0.966 \cdot 10^3$	$4.85 \cdot 10^3$	39.3
	$4.83 \cdot 10^3$	$13.7 \cdot 10^3$	111
	$9.66 \cdot 10^3$	$21.1 \cdot 10^3$	171
20	$1.21 \cdot 10^3$	$4.03 \cdot 10^3$	63.4
	$6.04 \cdot 10^3$	$11.9 \cdot 10^3$	188
	$12.1 \cdot 10^3$	$19.4 \cdot 10^3$	306

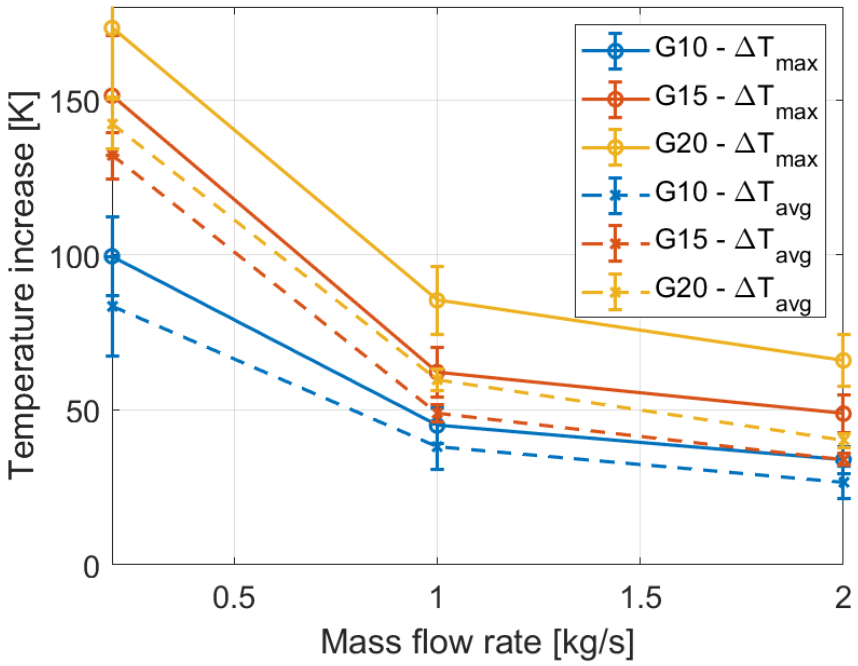

Figure 5.3: *Maximum and average temperature increase on the channel external wall for the Gyroid structures depending on the mass flow rate*

Figure (5.4) shows the temperature distribution on the channel external wall, when cooling with a mass flow rate of $1\,kg/s$. It is evident how a denser lattice produces lower values of the temperature and a more uniform distribution.

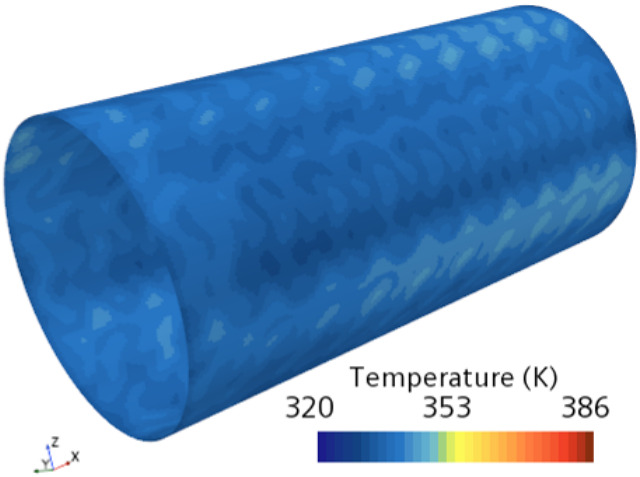

(a)

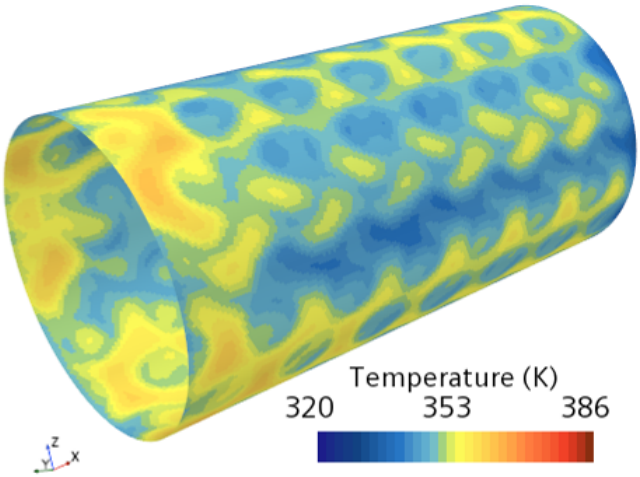

(b)

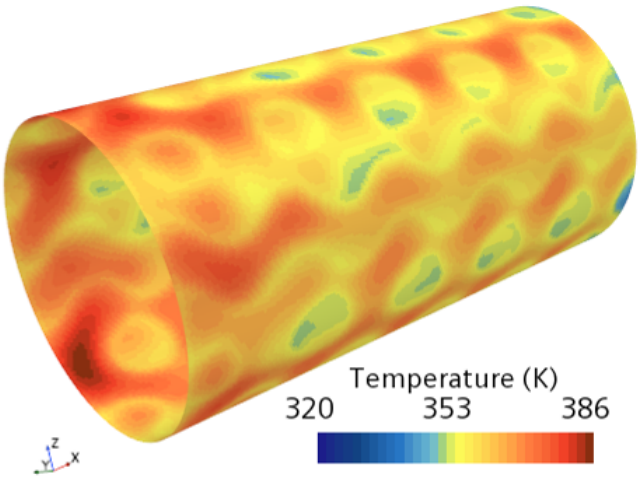

(c)

Figure 5.4: *Temperature field on the external wall for the three Gyroid structures with unit cell size of* $10\,mm$ *(a),* $15\,mm$ *(b) and* $20\,mm$ *(c)*

5.1.3 Lidinoid

For the *Lidinoid* structures, the maximum and average temperature increase with respect to the water inlet temperature ($300\,K$) on the channel external wall are reported respectively in tables (5.5). They are plotted also in figure (5.5). The lowering of the temperature is not linear with the unit cell size of structure. Moreover, the gap between the maximum and average temperature increase diminishes as the lattice gets denser.

Table 5.5: *Lidinoid - External wall maximum and average temperature increases and fluid maximum temperature increase with respect to inlet temperature* $[K]$ *depending on the mass flow rate* $[kg/s]$

$s\,[mm]$	$\dot{m}\,[kg/s]$	$\Delta T_{solid,MAX}\,[K]$	$\Delta T_{solid,AVG}\,[K]$	$\Delta T_{fluid,MAX}\,[K]$
10	0.2	71.8	57.7	70.1
	1	32.3	27.7	30.6
	2	23.6	18.1	21.0
15	0.2	80.0	64.5	78.5
	1	40.7	33.0	39.1
	2	33.9	24.3	32.0
20	0.2	118	91.2	117
	1	57.8	42.9	56.1
	2	46.1	30.0	44.4

The fluid maximum temperature increase is tabulated depending on the mass flow rate in table (5.5). The threshold of $110\,K$ is in this case mostly respected, so it is possible to assume that the flow is single-phase in the entire domain even with the lowest mass flow rate.

The heat transfer coefficient and the Nusselt number, computed from equations (5.2) and (5.1), are reported in tables (5.6). The heat transfer coefficient and the Nusselt number do not have a monotonic trend with the unit cell dimension.

Figure (5.5) presents the temperature field on the external wall of the channel for the three cases of *Lidinoid* structures, at $1\,kg/s$ of mass flow rate. On the chosen scale, the difference from one structure to the other is less evident than for the previous cases (*Diamond* and *Gyroid*). However, it is possible to appreciate an improvement of the uniformity in the case of unit cell size of $10\,mm$.

Table 5.6: *Lidinoid - Heat transfer coefficient and Nusselt number depending on the Reynolds number*

$s\,[mm]$	Reynolds number	HTC $[W/(m^2K)]$	Nusselt number
10	$0.398 \cdot 10^3$	$7.79 \cdot 10^3$	31.9
	$1.99 \cdot 10^3$	$19.4 \cdot 10^3$	79.6
	$3.98 \cdot 10^3$	$23.2 \cdot 10^3$	94.8
15	$0.550 \cdot 10^3$	$8.46 \cdot 10^3$	120
	$2.75 \cdot 10^3$	$17.7 \cdot 10^3$	251
	$5.50 \cdot 10^3$	$19.6 \cdot 10^3$	279
20	$0.699 \cdot 10^3$	$5.23 \cdot 10^3$	43.5
	$3.49 \cdot 10^3$	$14.1 \cdot 10^3$	117
	$6.99 \cdot 10^3$	$22.7 \cdot 10^3$	189

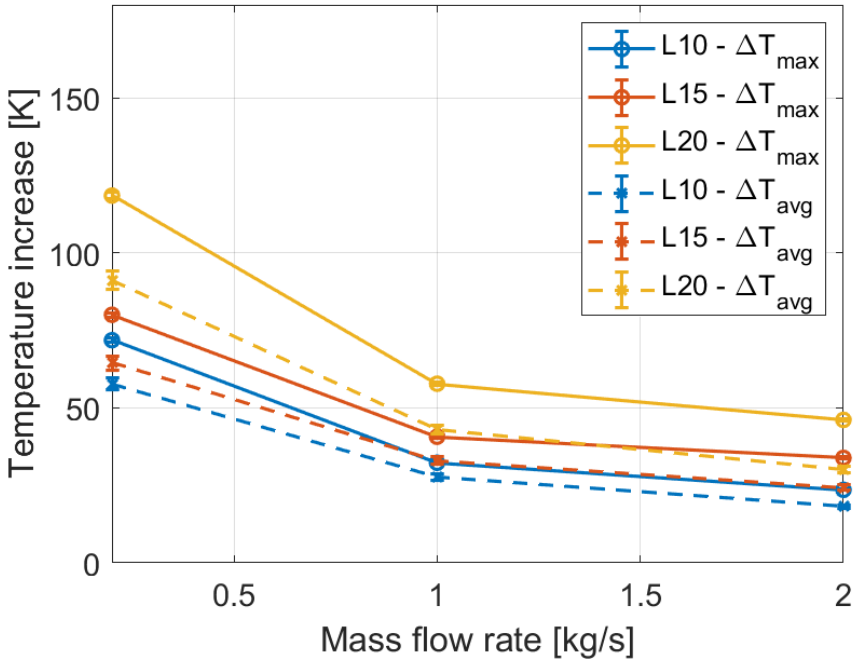

Figure 5.5: *Maximum and average temperature increase on the channel external wall for the Lidinoid structures depending on the mass flow rate*

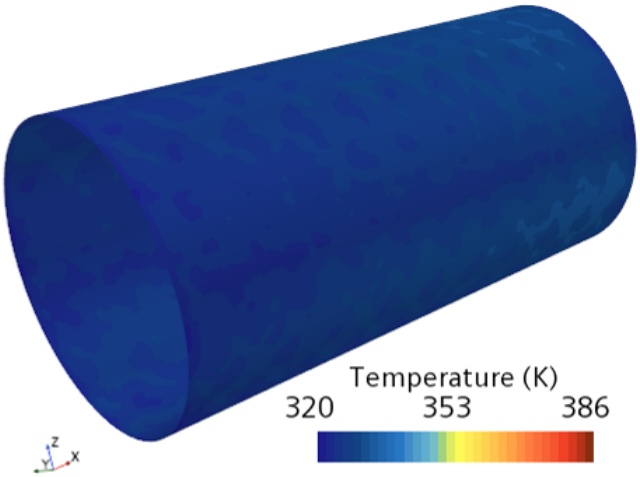

(a)

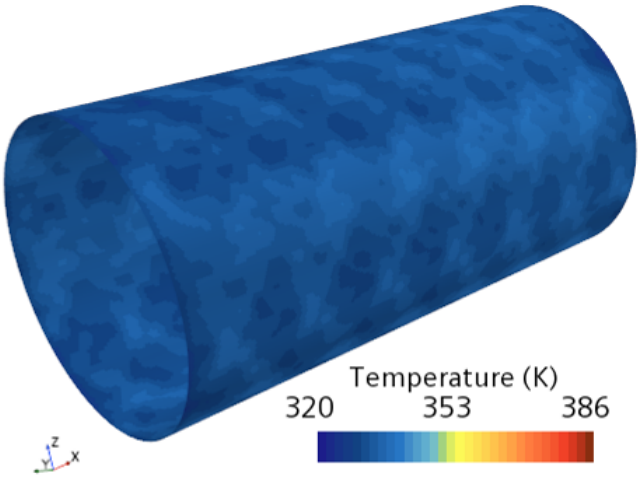

(b)

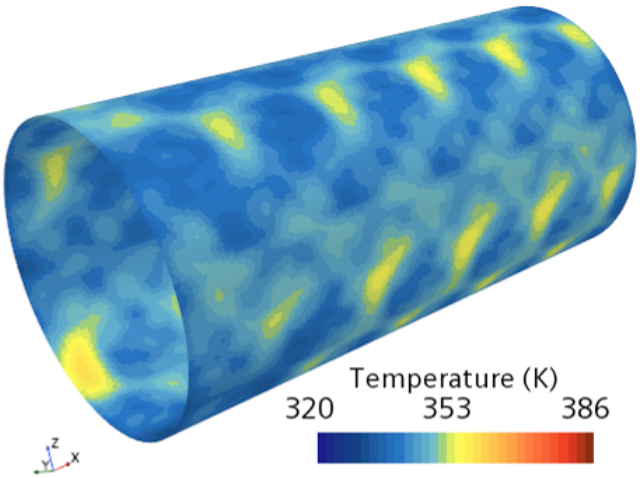

(c)

Figure 5.6: *Temperature field on the external wall for the three Lidinoid structures with unit cell size of* $10\,mm$ *(a),* $15\,mm$ *(b) and* $20\,mm$ *(c)*

5.1.4 SplitP

The maximum and average temperature increases obtained with the *SplitP* structures on the external wall of the channel are reported respectively in table (5.7). The same values are also plotted against the mass flow rate in figure (5.7). As occurs for all the other configurations, also here the difference between the maximum and average temperature increase on the heated wall decreases with lower unit cell dimension, suggesting a more uniform temperature distribution.

Table 5.7: *SplitP - External wall maximum and average temperature increases and fluid maximum temperature increase with respect to inlet temperature* $[K]$ *depending on the mass flow rate* $[kg/s]$

$s\,[mm]$	$\dot{m}\,[kg/s]$	$\Delta T_{solid,MAX}\,[K]$	$\Delta T_{solid,AVG}\,[K]$	$\Delta T_{fluid,MAX}\,[K]$
10	0.2	73.4	60.2	72.0
	1	32.4	27.4	30.8
	2	24.1	18.2	22.9
15	0.2	82.0	66.2	79.4
	1	44.4	36.9	42.7
	2	33.5	26.0	31.8
20	0.2	121	99.2	119
	1	59.2	43.5	57.8
	2	44.7	30.2	43.2

Table (5.7) collects also the computed values of the maximum temperature increase in the fluid. Remembering that the water saturation temperature at the outlet pressure ($3\,bar$) is approximately $407\,K$, the maximum acceptable temperature increase, that assures single-phase flow, is around $110\,K$. This upper limit is slightly exceeded by one of the configurations at the lowest mass flow rate. However, saturated conditions are restricted to small regions of the fluid domain next to the wall.

The heat transfer coefficient and Nusselt number of each configuration are reported in tables (5.8) depending on the Reynolds number. The configuration with unit cell size of $15\,mm$ appears in general to be the one with the highest heat transfer coefficient and Nusselt number.

The temperature field on the external wall of the channel is presented in figure (5.8) for the three *SplitP* structures, obtained at the intermediate value of mass flow rate ($1\,kg/s$). As commented for the *Lidinoid* case, the three fields look similar with this temperature scale, even though it is still possible to spot the different uniformity of the distribution.

Table 5.8: *SplitP - Heat transfer coefficient and Nusselt number depending on the Reynolds number*

$s\,[mm]$	Reynolds number	HTC $[W/(m^2K)]$	Nusselt number
10	$0.440 \cdot 10^3$	$7.19 \cdot 10^3$	33.6
	$2.20 \cdot 10^3$	$21.6 \cdot 10^3$	101
	$4.40 \cdot 10^3$	$26.8 \cdot 10^3$	125
15	$0.627 \cdot 10^3$	$9.17 \cdot 10^3$	114
	$3.14 \cdot 10^3$	$16.8 \cdot 10^3$	209
	$6.27 \cdot 10^3$	$26.9 \cdot 10^3$	336
20	$0.800 \cdot 10^3$	$5.23 \cdot 10^3$	53.0
	$4.00 \cdot 10^3$	$15.2 \cdot 10^3$	153
	$8.00 \cdot 10^3$	$24.3 \cdot 10^3$	244

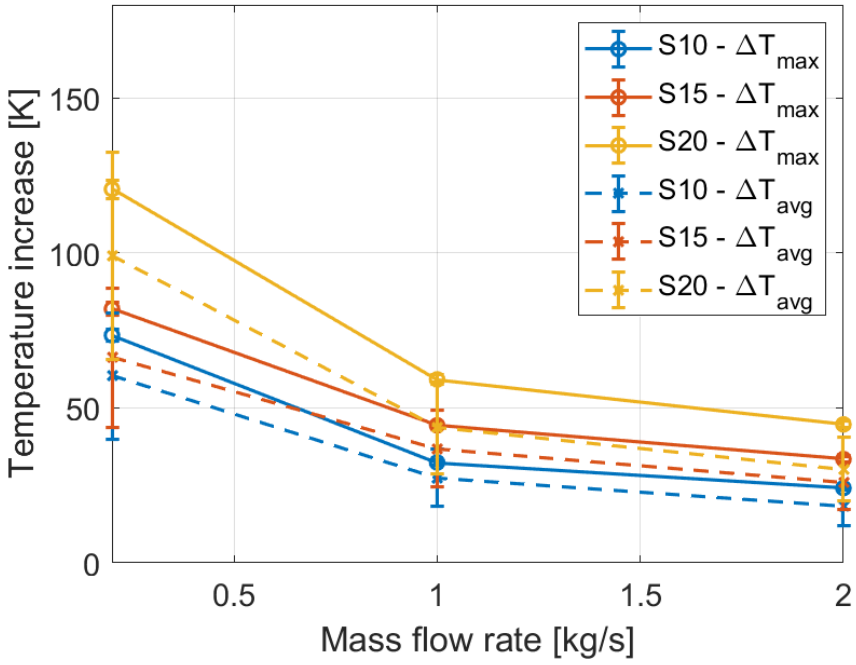

Figure 5.7: *Maximum and average temperature increase on the channel external wall for the SplitP structures depending on the mass flow rate*

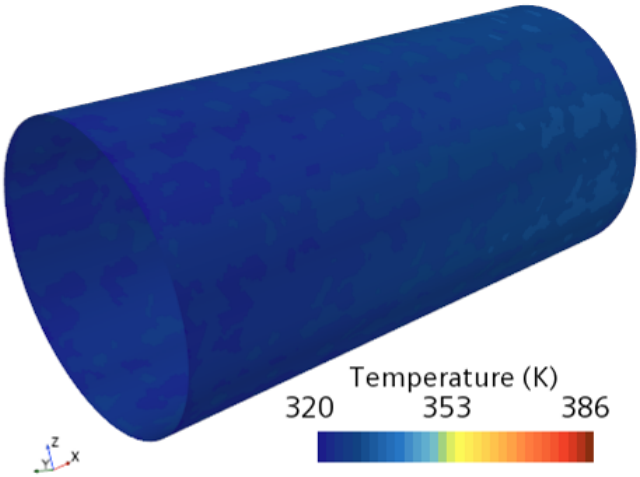

(a)

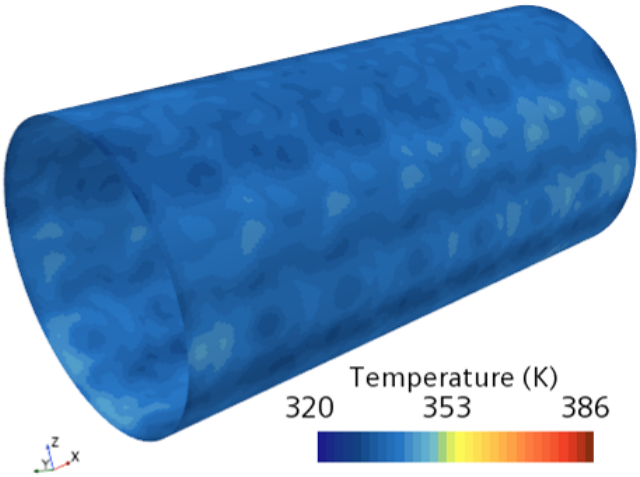

(b)

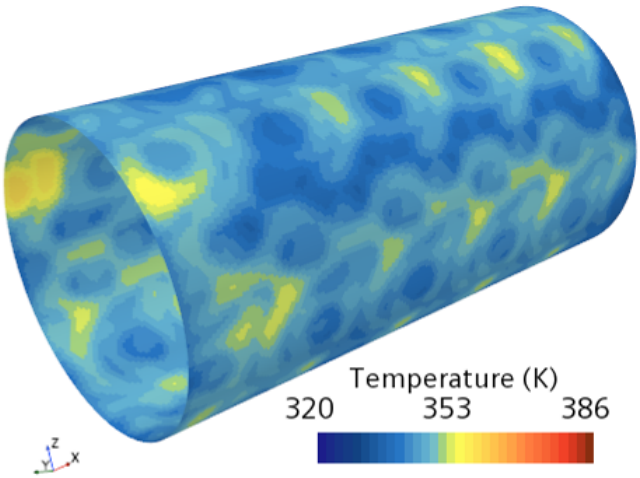

(c)

Figure 5.8: *Temperature field on the external wall for the three SplitP structures with unit cell size of* $10\,mm$ *(a),* $15\,mm$ *(b) and* $20\,mm$ *(c)*

5.1.5 Comparisons

To compare the thermal performance of the different configurations, the maximum and average temperature increase on the external wall of the channel are proposed in figure (5.9), collected by unit cell dimension. This parameter has been chosen because it appears to be the most significant one, since the target of this problem is to keep the temperature of the channel sufficiently low, to avoid oxidation, melting and structural issues in general.

Gyroid lattices are the ones that produce the highest values of temperature increase on the wall. *Lidinoid* and *SplitP* instead allow to get lower temperatures and the values resulting from these two are mostly superposed.

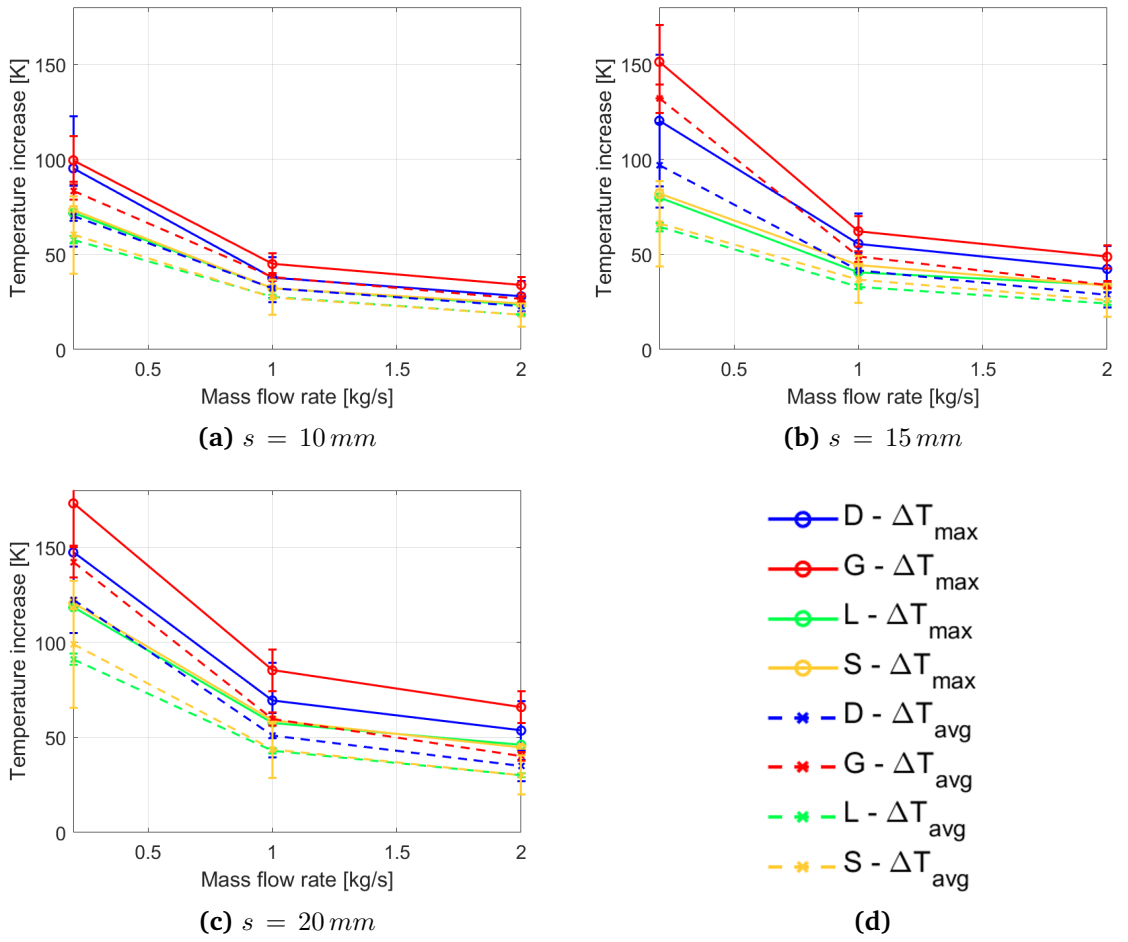

(a) $s = 10\,mm$ **(b)** $s = 15\,mm$ **(c)** $s = 20\,mm$ **(d)**

Figure 5.9: *Maximum and average temperature increase on the channel external wall for all the TPMS types with unit cell size* $10\,mm$ *(a),* $15\,mm$ *(b) and* $20\,mm$ *(c) and the legend (d)*

Also, considering the fluid maximum temperature increases exposed in the previous sections, it is worth noticing that, with the lowest mass flow rate ($0.2\,kg/s$), *Diamond* and *Gyroid* lattices with unit cell size of $15\,mm$ and $20\,mm$ do not allow to keep the fluid under the saturation condition, at least in some portions of the domain. For the other two structures the threshold of the temperature of $407\,K$ (saturation point at $3\,bar$) is also overcome, but of a smaller percentage, thus it is more probable to have a completely single-phase flow.

5.2 TPMS combinations

Thermal-hydraulic simulations have been performed on the channel equipped with the four designed combinations of TPMS.

The resulting maximum and average temperature increase on the channel external wall are reported in table (5.9) and in figure (5.10). The values of the four combinations are very similar and it is possible to see the influence of the core TPMS, that, occupying the majority of the pipe volume, has a prominent role in the cooling. However, a small gap between the structures with *Lidinoid* and *SplitP* can still be noticed.

Table 5.9: *TPMS combinations - External wall maximum and average temperature increases and fluid maximum temperature increase with respect to inlet temperature* $[K]$ *depending on the mass flow rate* $[kg/s]$

TPMS combination	$\dot{m}\,[kg/s]$	$\Delta T_{solid,MAX}\,[K]$	$\Delta T_{solid,AVG}\,[K]$	$\Delta T_{fluid,MAX}\,[K]$
D-L	0.2	105	78.8	103
	1	40.7	35.2	39.2
	2	29.8	25.5	28.2
D-S	0.2	105	79.1	104
	1	42.3	35.7	40.8
	2	30.5	25.7	28.9
G-L	0.2	102	84.5	101
	1	45.2	37.8	43.7
	2	33.1	27.2	33.7
G-S	0.2	103	85.1	101
	1	46.7	38.8	45.5
	2	34.3	27.8	32.8

In table (5.9) the maximum temperature increases obtained in the fluid are collected too. In all the cases, the flow results to be single-phase, since the temperature always falls below the limit of $407\,K$ that corresponds to the saturation temperature of the water at the outlet pressure. Thus, even though *Diamond* and *Gyroid* with unit cell size of $15\,mm$ do not completely satisfy this request, the insertion of a thin layer of a denser TPMS next to the wall enhances the heat transfer and avoids the water to reach saturation.

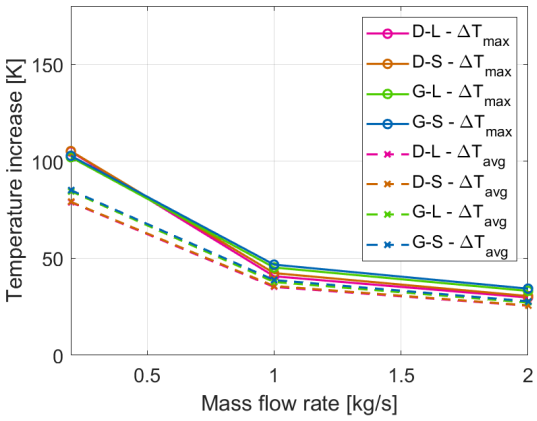

Figure 5.10: *Maximum and average temperature increase on the channel external wall for the four TPMS combinations*

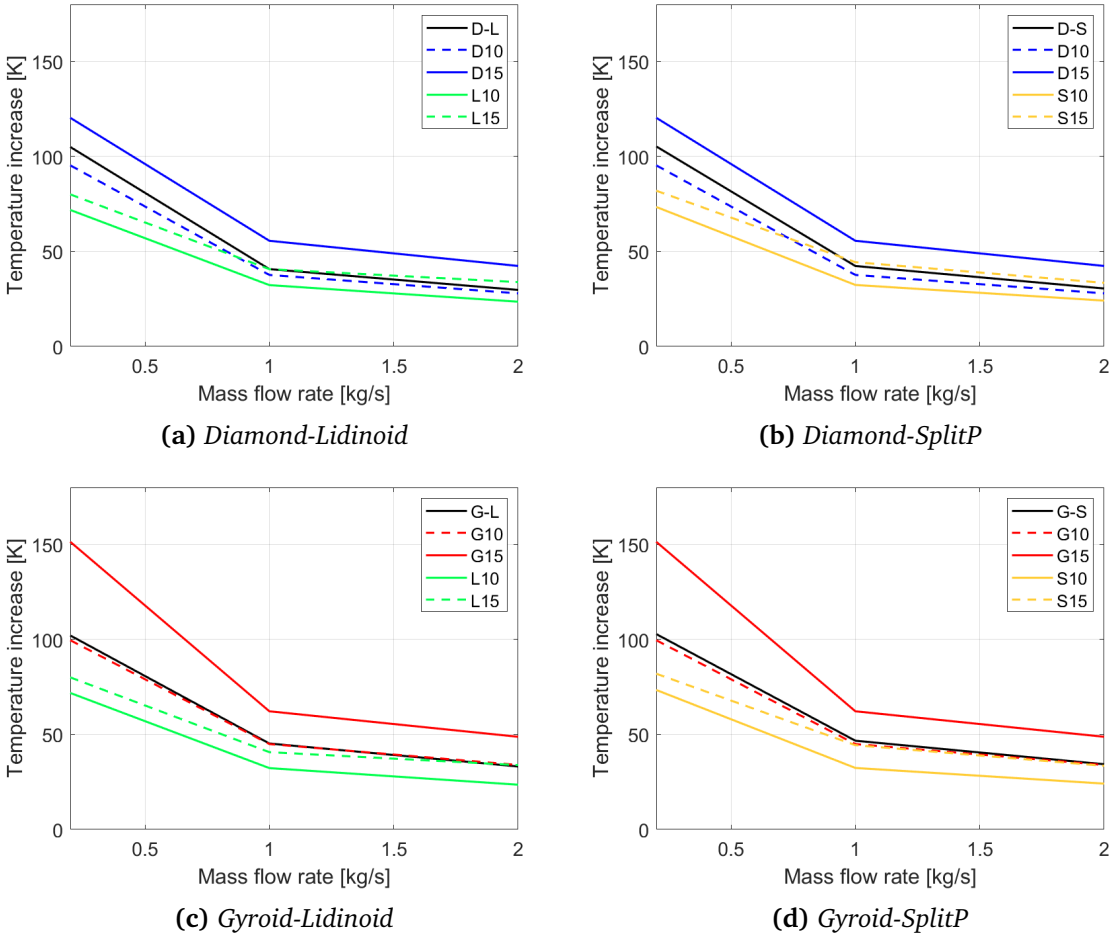

(a) *Diamond-Lidinoid*

(b) *Diamond-SplitP*

(c) *Gyroid-Lidinoid*

(d) *Gyroid-SplitP*

Figure 5.11: *Maximum temperature increase on the channel external wall for the four combinations, D-L (a), D-S (b), G-L (c) and G-S (d), compared to ones of the single TPMS*

In figure (5.11), the four combinations are compared to the single TPMS that compose them, as it has been already done for the hydraulic results. Only the maximum temperature increase on the wall is shown. It is interesting to notice that the values resulting from the simulations on the four combinations are very close or almost superposed to the ones corresponding to the core TPMS with unit cell $10\,mm$ and outer TPMS with unit cell $15\,mm$. However, both these configurations produce higher values of pressure drop, as shown previously in figure (4.22). So, it is possible to infer that, at least from a qualitative point of view, the TPMS combinations have better performance than the single TPMS structures.

In table (5.10), the heat transfer coefficient and the Nusselt number are reported depending on the Reynolds number. It can be noticed that the HTC values are coupled depending on the core TPMS (thus, D-L values are similar to those of D-S and G-L values to G-S), but for the Nusselt number the opposite occurs. That means that this dimensionless parameter is more influenced by the outer layer TPMS.

Table 5.10: *TPMS combinations - Heat transfer coefficient and Nusselt number depending on the Reynolds number*

TPMS combination	Reynolds number	HTC $[W/(m^2K)]$	Nusselt number
D-L	$0.657 \cdot 10^3$	$4.96 \cdot 10^3$	38.5
	$3.28 \cdot 10^3$	$13.1 \cdot 10^3$	102
	$6.57 \cdot 10^3$	$20.6 \cdot 10^3$	160
D-S	$0.673 \cdot 10^3$	$5.10 \cdot 10^3$	40.8
	$3.37 \cdot 10^3$	$13.7 \cdot 10^3$	110
	$6.73 \cdot 10^3$	$21.8 \cdot 10^3$	174
G-L	$0.739 \cdot 10^3$	$4.50 \cdot 10^3$	40.2
	$3.70 \cdot 10^3$	$11.8 \cdot 10^3$	106
	$7.39 \cdot 10^3$	$18.6 \cdot 10^3$	166
G-S	$0.760 \cdot 10^3$	$4.56 \cdot 10^3$	42.2
	$3.80 \cdot 10^3$	$12.2 \cdot 10^3$	113
	$7.60 \cdot 10^3$	$18.9 \cdot 10^3$	175

Chapter 6

Discussion

From the results presented in the previous chapters, it is evident that the TPMS type strongly influences the performance of the cooling channel. For all the TPMS types, smaller unit cell dimensions resulted in higher pressure drop and lower maximum temperature on the external wall.

Diamond and *Gyroid* showed lower values of pressure drop and friction factor with respect to *Lidinoid* and *SplitP*, at the cost of poorer thermal performances in terms of maximum and average temperature increase. However, the dimensionless analysis has highlighted that the Nusselt number has greater values for *Gyroid* and *Diamond* structures. The results obtained from the simulations on the TPMS combinations confirmed the expectations. The pressure drop remains limited, while the heat exchange next to the wall is enhanced by the presence of a denser TPMS in the outer layer.

To have a global vision of all the configurations and be able to effectively compare them, in the next section (6.1) the thermal efficiency index is defined and computed for them all.

6.1 Thermal efficiency index

A widely used parameter to compare different configurations is the thermal efficiency index (η), that evaluates the enhancement of the heat exchange with respect to the pressure loss. It is usually defined as in equation (6.1), exploiting the dimensionless variables, where the subscript 0 refers to the smooth tube.

$$\eta = \frac{\overline{Nu}/\overline{Nu}_0}{(f/f_0)^{1/3}} \tag{6.1}$$

For a clearer comparison, dimensional variables (heat transfer coefficient HTC and pressure drop Δp) have been used in this work to compute η, as in equation (6.2). This is suggested in [35], to eliminate the effect of having different hydraulic diameters.

$$\eta = \frac{HTC/HTC_0}{(\Delta p/\Delta p_0)^{1/3}} \tag{6.2}$$

The values of Δp_0 and HTC_0 have been obtained respectively from f_0 and $\overline{Nu}_0$ computed with Blasius and Dittus-Boelter correlations (equations (6.3) and (6.4)) [36].

$$f = 0.316 \cdot Re^{-0.25} \tag{6.3}$$

$$\overline{Nu} = 0.023 \cdot Re^{0.8} \cdot Pr^{0.4} \tag{6.4}$$

Table (6.1) presents the values of η for the TPMS structures with unit cell size $10\,mm$, $15\,mm$ and $20\,mm$. The values computed for the TPMS combinations are instead tabulated in (6.2).

Most of the values are smaller than 1, while a good turbulence promoter should produce η greater than 1. This indicates that the increase of the pressure drop with respect to the smooth tube affects the performance more than the heat transfer enhancement. However, the threshold may be lower than 1 for porous media, but there is not available literature on this topic yet.

Table 6.1: *Thermal efficiency index η for the four TPMS*

$s\,[mm]$	$\dot{m}\,[kg/s]$	Diamond	Gyroid	Lidinoid	SplitP
10	0.2	1.02	0.96	0.96	0.79
	1	0.73	0.74	0.64	0.64
	2	0.67	0.66	0.43	0.46
15	0.2	1.00	1.04	1.31	1.39
	1	0.77	0.78	0.73	0.66
	2	0.70	0.67	0.46	0.60
20	0.2	1.03	1.01	0.093	0.95
	1	0.80	0.79	0.68	0.72
	2	0.73	0.72	0.62	0.66

Table 6.2: *Thermal efficiency index η for the four TPMS combinations*

Mass flow rate $[kg/s]$	D-L	D-S	G-L	G-S
0.2	0.90	0.94	0.89	0.90
1	0.62	0.65	0.61	0.63
2	0.54	0.58	0.54	0.55

From the tables and from figures (6.1) and (6.2), it could be noticed that η increases with decreasing mass flow rate, reaching values close to or higher than 1. This suggests that at low Reynolds numbers the presence of the TPMS promotes the turbulence enhancing the heat transfer processes, while at high Reynolds numbers the flow impedance produced by the structures becomes more relevant. Thus, the use of TPMS-based structures for low-Re applications may be beneficial and should be further investigated.

The values corresponding to *Diamond* and *Gyroid* at the lowest mass flow rate and unit cell sizes of $15\,mm$ and $20\,mm$ have been included in the table and figures, even though those simulations might be affected by the fact that the fluid is not completely single-phase, as noted in chapter (5).

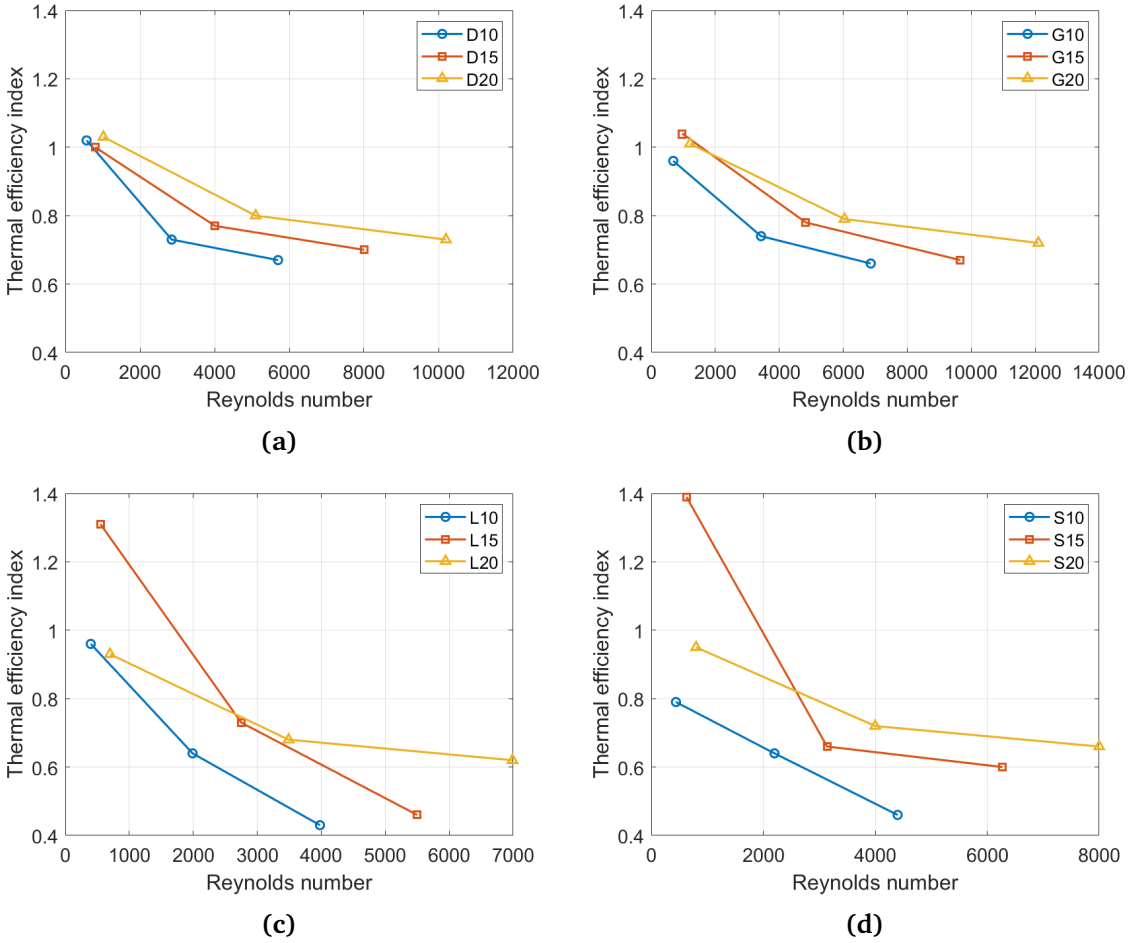

Figure 6.1: *Thermal efficiency index for the four TPMS, Diamond (a), Gyroid (b), Lidinoid (c) and SplitP (d)*

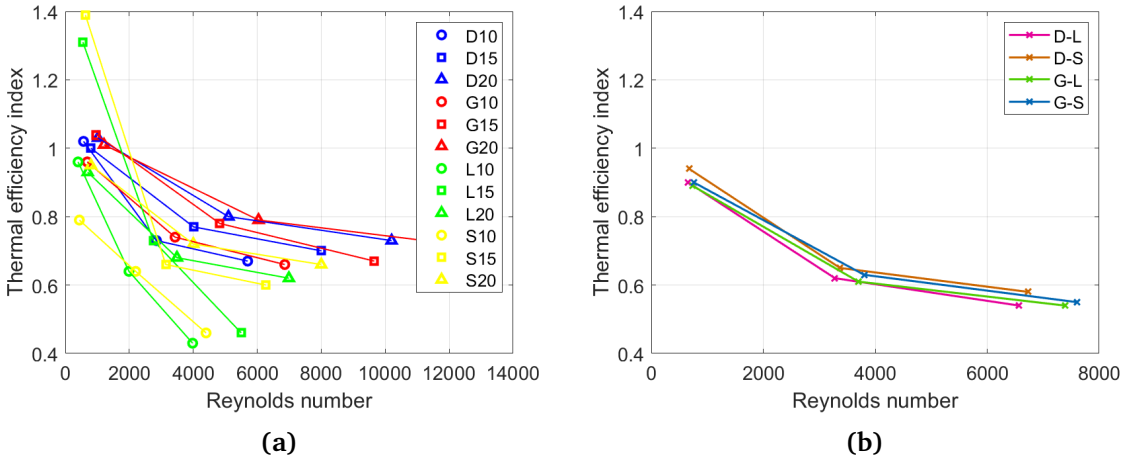

Figure 6.2: *Thermal efficiency index for all the TPMS configurations, single TPMS (a) and combinations (b)*

6.2 Conclusion and perspectives

In the present work, different structures obtained from four Triply Periodic Minimal Surfaces have been used to equip a circular channel. Their thermal-hydraulic performance has been analyzed computationally. It has been shown that the type of TPMS strongly influences both the hydraulic and the thermal parameters. In particular *Diamond* and *Gyroid* cause in general a moderate pressure drop in the fluid, while with *Lidinoid* and *SplitP* it is possible to keep the external wall temperature at a lower level, at the expenses of higher losses in the fluid pressure. The temperature values obtained for the channel wall are always far below the melting point of the material (Copper), that is around $1300\,K$, however, the mechanical properties could change significantly also below that point and a better cooling is beneficial. Moreover, the most uniform distribution of the temperature on the pipe wall is obtained with dense TPMS structures, that means setting a small unit cell size of the lattices.

The results obtained on the TPMS combinations are promising. Several settings, such as the topology type of the structures, the thickness of the outer layer or the unit cell size, could be modified to optimize these configurations and improve their performance.

The thermal efficiency index has been computed and has resulted to be strongly affected by the pressure drop increase with respect to the smooth tube. This seems to be less evident at lower mass flow rates, suggesting that further investigation in the laminar regime should be performed.

As a complementary study, a parametric analysis on the channel shape has been performed, using *Gyroid* only as TPMS structure. This has allowed to estimate the minimum ratio between the hydraulic diameter and the TPMS unit cell size needed to nullify the effect of the channel shape on the hydraulic performance.

The generation of TPMS-based structures, as discussed in section (1.1), offers multiple options to adapt them to the specific shape and dimensions of each application domain. In the present work, only a small portion of this wide range of possibilities has been analyzed. For sure, further investigations are needed to correlate the heat removal capability of the TPMS to their design parameters. Moreover, the study have focused on *sheet-TPMS* structures, while *solid-TPMS* could be interesting as well and a comparative analysis has been performed only in few research works so far.

6.3 Acknowledgments

The thesis has been performed in the framework of a joint research project with the Marine Engineering Technology Department of Texas A&M University of Galveston.

Computational resources were provided by HPC@POLITO, a project of Academic Computing within the Department of Control and Computer Engineering at the Politecnico di Torino (http://www.hpc.polito.it).

Appendix A

Applications of TPMS

The study performed in this thesis is focused on the application of TPMS-based structures for thermal management of high heat flux components. However, there are several fields where TPMS are currently under investigation. A non-complete review of them is proposed here to provide a clearer vision of the potentiality of these lattices.

A.1 Thermal management

Many recent studies have investigated the possibilities of using TPMS for thermal-hydraulic applications. As discussed in section (1.1), depending on the type of the structure, *solid* or *sheet*, TPMS can be suitable as heat sinks or heat exchangers.

This work focused on the analysis of TPMS as heat sinks and the ending point would be to apply them to nuclear fusion components. As an example, the current cooling strategy of fusion Gyrotron cavity (pink in figure (A.1a)) consists of packed matrices of Raschig Rings, hollow cylinders of millimetric size, showed in figure (A.1b).

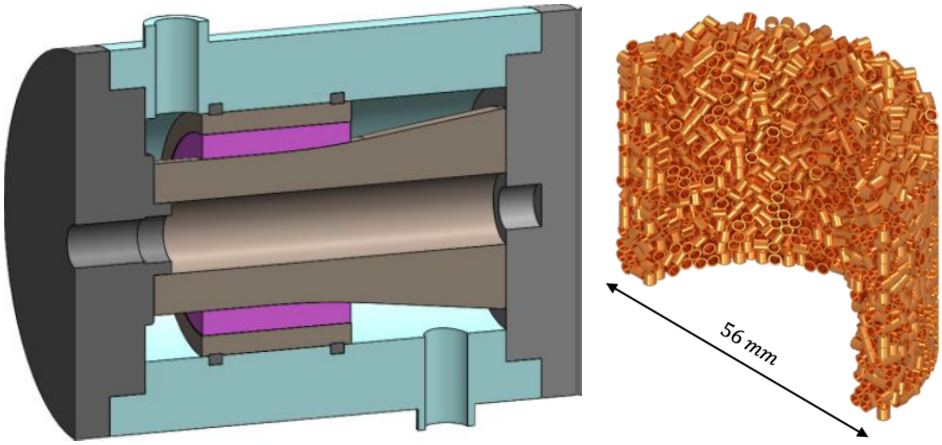

Figure A.1: *Gyrotron cavity (a) with the insertion of a Raschig Rings matrix (b) [37]*

Even though their performance has already been proved to be satisfying, the design and simulation of such structures are limited due to their random nature. As an alternative cooling

configuration, mini-channels have been investigated, since their reduced diameter dimension significantly enhances the heat transfer. However, the probability for a channel of getting plugged is not negligible. The application of TPMS-based structures could substitute them and be beneficial to solve those issues.

As another example, also the cooling strategy of divertor tiles is under development and TPMS-based structures are among the considered possibilities. Figure (A.2) shows an example of design.

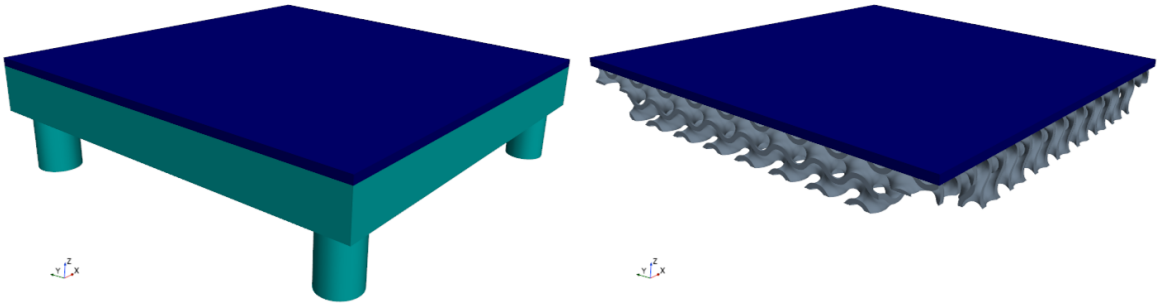

(a) **(b)**

Figure A.2: *Design of a divertor tile (a) equipped with an internal Gyroid structure (b)*

Some studies are also devoted to the application of TPMS-based structures in solar thermal receivers, since their geometrical characteristics are particularly suitable as they provide high interfacial heat transfer coefficient, low pressure drop and uniform solar absorption, required for a good solar thermal conversion [38].

A great number of research works have focused on the implementation of innovative heat exchangers by using *sheet-TPMS* structures. In this case, the interest is mainly due to the high surface-to-volume ratio that makes TPMS very compact. Several configurations have been analyzed so far, such as the one reported in figure (A.3) from the already cited paper by Kim et al. [23].

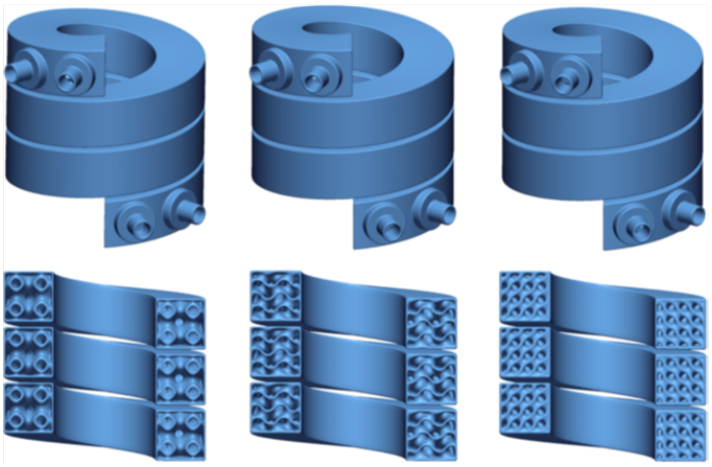

Figure A.3: *Highly curved compact heat exchangers with Primitive, Gyroid and Diamond structures [23]*

A.2 Carbon capture

Green House Gases (GHG) emission plays an important role in the climate change issues that the world is facing. Thus, CO_2 capture has become an interesting research field to mitigate the release of GHG in the atmosphere. The most widely developed technology is post-combustion CO_2 capture, that uses reactive absorption with aqueous solutions containing organic compounds (alkanolamine) to extract the Carbon dioxide from a gas [39]. This process takes place in packed columns where the fluids flow in counter-current. The gas mixture travels up while the water solution flows downward progressively removing the CO_2 from the gas.

TPMS may provide a good solution for the internal structure of the packed columns and the *Diamond* lattice has been analyzed for this purpose by Singh et al. [40], as shown in figure (A.4).

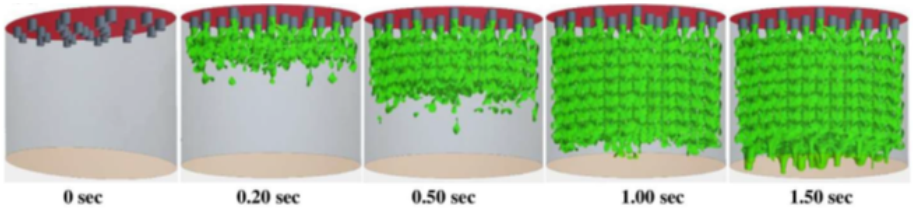

Figure A.4: *Gas-liquid interface at different time instants in Diamond packed column [40]*

A.3 Energy storage

The energy storage field is continuously evolving and is gaining interest in particular for electric vehicles applications. To comply with safety and performance requirements, the design of the battery thermal management system (BTMS) is crucial. As an alternative to an active cooling, phase change materials (PCM) offer the possibility to store the battery heat without energy consumption (passive method). Moreover, the process is based on the absorption of latent heat thus there is no evident temperature change.

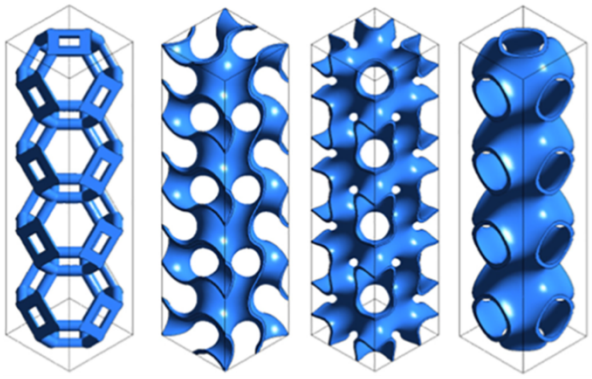

Figure A.5: *Metal skeletons of Kelvin, Gyroid, IWP and Primitive structures [41]*

TPMS-based structures could be used as skeletons impregnated of PCM to enhance the thermal conductivity. This solution has been proposed by Qureshi et al. in 2021 [41] and

their work proved that TPMS performed better than traditional structures (as the Kelvin-based one, showed in figure (A.5), compared to three TPMS). More recently, Fan et al. [42] have elaborated more on this concept and have come out with a proposal of combination of TPMS to increase the thermal conductivity farther from the battery. Thus, the *Primitive* structure is inserted next to the battery, while the *IWP* with a smaller unit cell dimension occupies the volume farther from it as shown in figure (A.6). This again confirms the wide range of possibilities offered by the TPMS generation parameters.

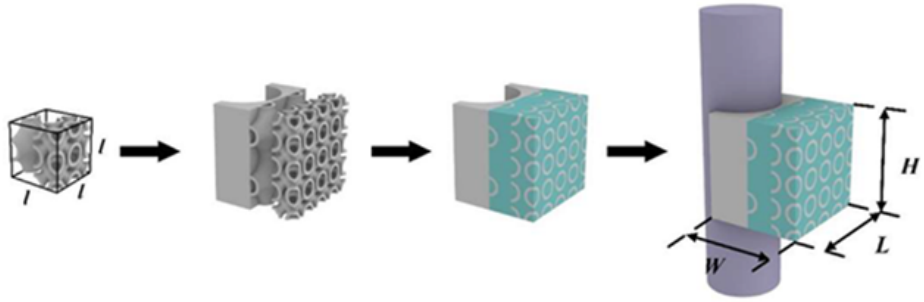

Figure A.6: *Model of the BTMS based on PCM filled with Primitive-IWP combination [42]*

A.4 Biomedical applications

TPMS are also analyzed in tissue engineering, in particular as bone scaffolds. In fact the porosity of TPMS matrices enables to effectively mimic the bones structure and to repair critical defects of fractures. The objective is to select an optimal lattice type and porosity to assure a fast recover and TPMS are particularly suitable due to their high surface-to-volume ratio that allows more cell attachment compared to other geometries [20]. Moreover, the mathematical generation of TPMS is a key point in the precision of the porosity that can be tailored depending on the measured one of the patient bones, as in figure (A.7).

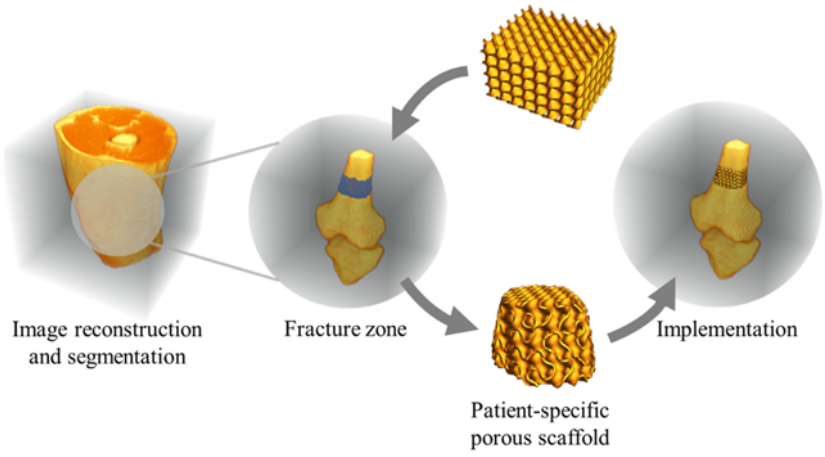

Figure A.7: *Patient-specific surgical framework for bone regeneration [19]*

A.5 Structural components

TPMS result to be suitable for structural purposes too and this possibility has been inspired by nature. In fact there is evidence of some TPMS natural systems such as sea urchins, biological cubic membranes, butterfly wing scales (shown in figure (A.8) and exoskeletons of some insects.

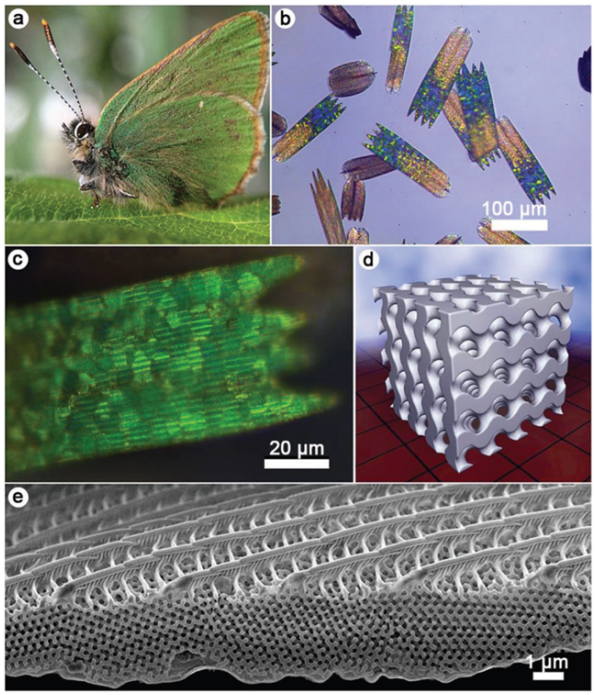

Figure A.8: *Photograph of a C. rubi butterfly, with the optical and scanning electron microscope images of the wing scale compared to a Gyroid [43]*

Studying these natural structures, understanding their functions and properties is essential in order to be able to reproduce them [43]. Due to their high porosity, TPMS-based structures result to be very light and a moderate quantity of material is needed to manufacture them. Therefore, their mechanical properties have been investigated, among all by Novak et al. [44] and by Khaleghi et al. [45], to asses their suitability for structural purposes.

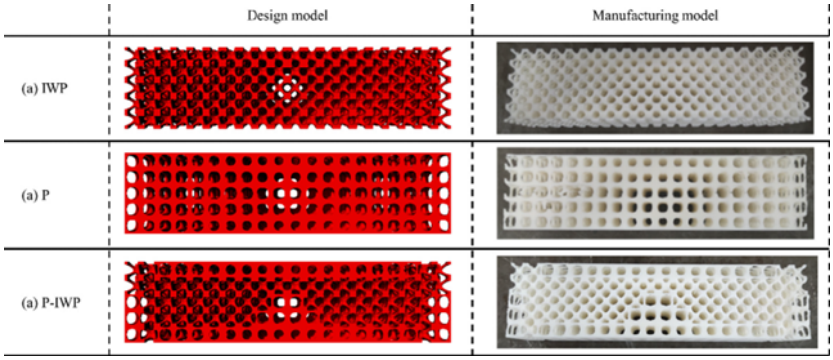

Figure A.9: *Three types of three-point bending beams, IWP, Primitive and the combination of them [46]*

The application of TPMS-based structures is also under investigation in the field of architected cellular materials, that aim at the design of lightweight structural components with high stiffness and strength. These would be strongly beneficial for example in the automotive industry, providing advantages in terms of fuel consumption and performance. Feng et al. [46] performed a stiffness optimization study on architected cellular structural materials combining different sizes of TPMS lattices, shown in figure (A.5).

The possibility to design the internal lattice of the materials starting from simulations results allows to reduce stress concentration in weak areas of the structure and minimize the failure probability.

Bibliography

[1] IPCC, *Global Warming of 1.5 °C, Special Report on the Impacts of Global Warming of 1.5°C above Pre-Industrial Levels and Related Global Greenhouse Gas Emission Pathways, in the Context of Strengthening the Global Response To the Threat of Climate Change*, Intergovernamental Panel on Climate Change, 2022, https://www.ipcc.ch/sr15/

[2] IEA, *World Energy Outlook 2022*, 2022, Paris, https://www.iea.org/reports/world-energy-outlook-2022

[3] Efstathios E. Michaelides, *Alternative Energy Sources*, Green Energy and Technology, Springer, 2012

[4] H. Ritchie, M. Roser, P. Rosado, *Energy*, 2022, published online at OurWorldInData.org, https://ourworldindata.org/energy

[5] UNECE, *Carbon Neutrality in the UNECE Region: Integrated Life-cycle Assessment of Electricity Sources*, United Nations Economic Commission for Europe, 2022, Geneva

[6] EUROfusion, *European Research Roadmap to the Realisation LONG VERSION of Fusion Energy*, 2018

[7] L. Savoldi, A. Allio, A. Leggieri, *Optimization of the flow distribution in a gyrotron cavity using evolutionary CFD simulations driven by a genetic algorithm*, International Journal of Heat and Fluid Flow, Volume 96, 2022, 108987, ISSN 0142-727X, https://doi.org/10.1016/j.ijheatfluidflow.2022.108987

[8] Siemens Digital Industries Software Simcenter STAR-CCM+ User Guide v2021.1, Siemens, 2021

[9] https://ntopology.com/

[10] *Minimal surface*, Wikipedia
https://en.wikipedia.org/wiki/Minimal-surface

[11] J.L. Lagrange, *Oeuvres*, Gauthier-Villars, Paris, 1867

[12] J.B. Meusnier, *Mémoire sur la courbure des surfaces*, 1881

[13] H. Karcher, K. Polthier, *Construction of Triply Periodic Minimal Surfaces*, 1996

[14] H. A. Schwarz, *Gesammelte Mathematische Abhandlungen*, Springer, Berlin, 1933

[15] E. R. Neovius, *Bestimmung zweier spezieller periodischer Minimalflächen*, Akad. Abhandlungen, Helsingfors, 1883

[16] A. Schoen, *Geometry Garret*
https://schoengeometry.com/e-tpms.html

[17] A. Schoen, *Infinite Periodic Minimal Surfaces without Self-Intersections*, Electronics Research Center, Cambridge, 1970

[18] T. Pereira, J.V. Kennedy, J. Potgieter, *A comparison of traditional manufacturing vs additive manufacturing, the best method for the job*, 14th Global Congress on Manufacturing and Management (GCMM), 2018

[19] A. Karakoc, *RegionTPMS—Region based triply periodic minimal surfaces (TPMS) for 3-D printed multiphase bone scaffolds with exact porosity values*, SoftwareX, 2021

[20] E.F. Lehder, I.A. Ashcroft, R.D. Wildman, L.A. Ruiz-Cantu, I. Maskery, *A multiscale optimisation method for bone growth scaffolds based on triply periodic minimal surfaces*, Biomechanics and Modeling in Mechanobiology, 2021

[21] H. Peng, F. Gao, W. Hu, *Design, modeling and characterization of Triply Periodic Minimal Surface heat exchangers with additive manufacturing*, Solid Freeform Fabrication Conference, August 2019

[22] T. Dixit, E. Al-Hairi, M.C. Paul, P. Nithiarasu, S. Kumar, *High performance, microarchitected, compact heat exchanger enabled by 3D printing*, Applied Thermal Engineering, Volume 210, 2022, 118339, ISSN 1359-4311, https://doi.org/10.1016/j.applthermaleng.2022.118339

[23] J. Kim et al., *3D printed compact heat exchangers with mathematically defined core structures*, Journal of Computational Design and Engineering, 2020, 7(4), 527–550

[24] M. Alteneiji, M.I. Hassan Ali, K.A. Khan, R.K. Abu Al-Rub, *Heat transfer effectiveness characteristics maps for additively manufactured TPMS compact heat exchangers*, Energy Storage and Saving, 2022

[25] O. Al-Ketan, M. Ali, M. Khalil, R. Rowshan, K.A. Khan, R.K.A. Al-Rub, *Forced convection computational fluid dynamics analysis of architected and three-dimensional printable heat sinks based on Triply Periodic Minimal Surfaces*, Journal of Thermal Science and Engineering Applications, Volume 13, Issue 2, April 2021

[26] T. Femmer, A.J.C. Kuehne, M. Wessling, *Estimation of the structure dependent performance of 3-D rapid prototyped membranes*, Chemical Engineering Journal, 2015

[27] N. Baobaid, M.I. Ali, K.A. Khan, R.K.A. Al-Rub, *Fluid flow and heat transfer of porous TPMS architected heat sinks in free convection environment*, Case Studies in Thermal Engineering, Volume 33, 2022, 101944, ISSN 2214-157X, https://doi.org/10.1016/j.csite.2022.101944

[28] C. Fee, *3D-printed porous bed structures*, Current Opinion in Chemical Engineering, Vol. 18, 2017

[29] K. Yeranee, Y. Rao, *A Review of Recent Investigations on Flow and Heat Transfer Enhancement in Cooling Channels Embedded with Triply Periodic Minimal Surfaces (TPMS)*, Energies, 2022

[30] O. Al-Ketan, R.K.A. Abu Al-Rub, *MSLattice: A free software for generating uniform and graded lattices based on triply periodic minimal surfaces*, Mat Design Process Comm. 2021, https://doi.org/10.1002/mdp2.205

[31] H.K. Versteeg, W. Malalasekera, *An Introduction to Computational Fluid Dynamics*, Second Edition, 2007

[32] S. Lardeau, F. Billard, *Development of an elliptic-blending lag model for industrial applications*, 54th AIAA Aerospace Sciences Meeting, 2016

[33] R. Difonzo, E. Gajetti, L. Savoldi, N. Fathi, *Assessment of different RANS turbulence models in mini-channels for the cooling of MW-class gyrotron resonators*, International Journal of Heat and Mass Transfer 193, 122922, 2022

[34] American Society of Mechanical Engineers, *Standard for Verification and Validation in Computational Fluid Dynamics and Heat Transfer*, ASME V&V 20, 2019

[35] L. Liu, Z. Cao, T. Shen, L. Zhang, L. Zhang, *Experimental and numerical investigation on flow and heat transfer characteristics of a multi-waves internally spiral finned tube*, International Journal of Heat and Mass Transfer, Volume 172, 2021, 121104, ISSN 0017-9310, https://doi.org/10.1016/j.ijheatmasstransfer.2021.121104

[36] F.P. Incropera, D.P. Dewitt, T.L Bergman, A.S. Lavine *Fundamentals of heat and mass transfer*, Sixth Edition, New York: Wiley, 1996

[37] A. Allio, R. Difonzo, A. Leggieri, F. Legrand, R. Marchesin, L. Savoldi, *Test and Modeling of the Hydraulic Performance of High-Efficiency Cooling Configurations for Gyrotron Resonance Cavities*, Energies 2020, 13, 1163, doi:10.3390/en13051163

[38] D. Xu, M. Lin, *Design controllable TPMS structures for solar thermal applications: A pore-scale vs. volume-averaged modeling approach*, International Journal of Heat and Mass Transfer, Volume 201, Part 2, 2023, 123625, ISSN 0017-9310, https://doi.org/10.1016/j.ijheatmasstransfer.2022.123625

[39] F.M. Khan, V. Krishnamoorthi, T. Mahmud, *Modelling reactive absorption of CO2 in packed columns for post-combustion carbon capture applications*, Chemical Engineering Research and Design, Volume 89, Issue 9, 2011, Pages 1600-1608, ISSN 0263-8762, https://doi.org/10.1016/j.cherd.2010.09.020

[40] R.K. Singh, Y. Fu, Chao Zeng, D.T. Nguyen, P. Roy, J. Bao, Z. Xu, G. Panagakos, *Hydrodynamics of countercurrent flow in an additive-manufactured column with triply periodic minimal surfaces for carbon dioxide capture*, Chemical Engineering Journal, Volume 450, Part 2, 2022, 138124, ISSN 1385-8947, https://doi.org/10.1016/j.cej.2022.138124

[41] Z.A. Qureshi, S.A.B. Al-Omari, E. Elnajjar, O. Al-Ketan, R.A. Al-Rub, *Using triply periodic minimal surfaces (TPMS)-based metal foams structures as skeleton for metal-foam-PCM composites for thermal energy storage and energy management applications*, International

Communications in Heat and Mass Transfer, Volume 124, 2021, 105265, ISSN 0735-1933, https://doi.org/10.1016/j.icheatmasstransfer.2021.105265

[42] Z. Fan, Y. Fu, R. Gao, S. Liu, *Investigation on heat transfer enhancement of phase change material for battery thermal energy storage system based on composite triply periodic minimal surface*, Journal of Energy Storage, Volume 57, 2023, 106222, ISSN 2352-152X, https://doi.org/10.1016/j.est.2022.106222

[43] L. Han, S. Che, *An Overview of Materials with Triply Periodic Minimal Surfaces and Related Geometry: From Biological Structures to Self-Assembled Systems*, Advanced Materials, 2018, 30, 1705708. https://doi.org/10.1002/adma.201705708

[44] N. Novak, O. Al-Ketan, L. Krstulović-Opara, R. Rowshan, R.K.A. Al-Rub, M. Vesenjak, Z. Ren, *Quasi-static and dynamic compressive behaviour of sheet TPMS cellular structures*, Composite Structures, Volume 266, 2021, 113801, ISSN 0263-8223, https://doi.org/10.1016/j.compstruct.2021.113801

[45] S. Khaleghi, F.N. Dehnavi, M. Baghani, M. Safdari, K. Wang, M. Baniassadi, *On the directional elastic modulus of the TPMS structures and a novel hybridization method to control anisotropy*, Materials & Design, Volume 210, 2021, 110074, ISSN 0264-1275, https://doi.org/10.1016/j.matdes.2021.110074

[46] Y. Feng, T. Huang, Y. Gong, P.Jia, *Stiffness optimization design for TPMS architected cellular materials*, Materials & Design, Volume 222, 2022, 111078, ISSN 0264-1275, https://doi.org/10.1016/j.matdes.2022.111078

Ringraziamenti

A conclusione di questo mio percorso universitario, ci terrei a ringraziare le persone che, da vicino o da lontano, mi hanno accompagnata e permesso di arrivare fino a qui.

Un sentito grazie alla professoressa Laura Savoldi per la dedizione con cui mi ha seguita in questo lavoro di tesi e per avermi sempre incoraggiata e spronata a fare del mio meglio e a superare le mie paure e insicurezze.

Grazie al professor Nima Fathi, con cui ho avuto il piacere di lavorare nei quattro mesi trascorsi in Texas, per la sua disponibilità e per la gentilissima accoglienza.

Un grazie di cuore ai miei genitori e alla mia sorellina Letizia che mi hanno sempre supportata, ma soprattutto sopportata, tra gli alti e bassi di questi anni. Non bastano le parole per dirvi quanto vi sono grata.

Un grazie anche ai miei nonni, in particolare a mio nonno Enrico, che con il suo interesse e la sua passione per la scienza mi ha dato un grande sostegno e mi ha sempre stimolata ad andare a fondo nello studio.

Infine un grazie va alle ragazze nucleari con cui ho condiviso gioie e dolori di questa magistrale. Grazie a Eleonora, che stata un'insostituibile compagna di TPMS (e non solo) e spero continuerà a esserlo. Grazie anche a Diana, Betta ed Eleonora A. che hanno spesso dovuto ascoltare i miei racconti e le mie preoccupazioni e mi sono sempre state accanto con il sorriso. Questo traguardo è anche merito vostro.